This is to certify that the
dissertation entitled

QUASARS, CLUSTERS AND COSMOLOGY

presented by

NEELAM DHANDA

has been accepted towards fulfillment
of the requirements for the

Ph.D. degree in Physics and Astronomy

Major Professor's Signature

Aug 11, 2010

Date

MSU is an Affirmative Action/Equal Opportunity Employer

QUASARS, CLUSTERS AND COSMOLOGY

By

Neelam Dhanda

A DISSERTATION

Submitted to
Michigan State University
in partial fulfillment of the requirements
for the degree of

DOCTOR OF PHILOSOPHY

Physics and Astronomy

2010

ABSTRACT

QUASARS, CLUSTERS AND COSMOLOGY

By

Neelam Dhanda

PART A: Acceleration of the Universe and Modified Gravity:

We study the power of next-generation galaxy cluster surveys (such as eROSITA and WFXT) in constraining the cosmological parameters and especially the growth history of the Universe, using the information from galaxy cluster redshift and mass-function evolution and from cluster power spectrum. We use the Fisher Matrix formalism to evaluate the potential for the galaxy cluster surveys to make predictions about cosmological parameters like the gravitational growth index γ. The primary purpose of this study has been to check whether we can rule out one or the other of the underlying gravity theories in light of the present uncertainty of mass-observable relations and their scatter evolution.

We found that these surveys will provide better constraints on various cosmological parameters even after we admit a lack of complete knowledge about the galaxy cluster structure, and when we combine the information from the cluster number count redshift and mass evolution with that from the cluster power spectrum. Based on this, we studied the ability of different surveys to constrain the growth history of the Universe. It was found that whereas eROSITA surveys will need strong priors on cluster structure evolution to conclusively rule out one or the other of the two gravity models, General Relativity and DGP Braneworld Gravity; WFXT surveys do hold the special promise of differentiating growth and telling us whether it is GR or not, with its wide-field survey having the ability to say so even with 99% confidence.

PART B: Chemical Evolution in Quasars:

We studied chemical evolution in the broad emission line region (BELR) of nitrogen rich quasars drawn from the SDSS Quasar Catalogue IV. Using tools of emission-line spectroscopy, we made detailed abundance measurements of ~ 40 quasars and estimated their metallicities using the line-intensity ratio method. It was found that quasars with strong nitrogen lines are indicators of high metallicities. Some of these quasars have reached metallicities as high as $Z \sim 20Z_{\odot}$. Our detailed analysis showed that except in three QSOs, most of the different line-intensity ratios implied the similar metallicities. This verifies that this abundance analysis technique does produce meaningful results. The exceptions are the line-intensity ratio NIV]/CIV, which gives systematically low metallicities and the line-intensity ratio NV/He II, which gives systematically high metallicities.

We compared our findings with the predictions of the galactic chemical evolution models. From this study it was concluded that such high metallicities are reached either by requiring a top-heavy Initial Mass Function (IMF) for the quasar host galaxy as suggested by theoretical models, or by physically catastrophic events such as mergers that trigger star formation in already evolved systems which then leads to extreme metallicities in such quasars.

To The Universe

ACKNOWLEDGMENTS

As this moment my thanks are due to many people.

I would like to thank my advisor Prof. Mark Voit and also Prof. Jack Baldwin for letting me do this thesis on two separate projects, guiding me all along. And thanks to all my other committee members, Prof. R. Sekhar Chivukula, Prof. S. D. Mahanti and Prof. Steve Zepf for supporting me in this endeavour.

My sincere thanks to many wonderful teachers I have had all my life. At this moment my heartfelt thanks go out to Sir Jose Cherian, my Physics teacher in high school who, I would say, is the person behind my passion for physics. Not forgetting my science teacher, Mrs. Gurmeet Kaur for teaching us in a loving way, all the wonderful things about science, I will always be indebted to you, Ma'am. And many thanks to Prof. Ajoy Ghatak for making learning quantum mechanics and fiber optics such a wonderful experience during my M.Sc days. Prof. Voit, you as a teacher were amazing too! It was an honour to learn radiation astrophysics from you.

I would also like to thank my colleagues, Eric Pellegrini, David Ventigmilia and Young Sun Lee for introducing me to the tricks of the trade, and answering my numerous questions related to IRAF, IDL and LaTeX. Thank you for your immense help all along these years.

Thanks to all those persons whom I met as strangers but kept as lifelong friends, including Shweta, Sonal, Sheenu, Trupti and Saurabh. Finally, I would like to thank my family for having faith in me all along, and for showing immense patience while waiting for me and bearing me all this time as I near the completion of my Ph.D. Thanks to Christopher Waters for the LaTeX class used to format this thesis.

I, hereby, express my gratitude towards the Department of Physics and Astronomy, Michigan State University for providing me with this opportunity to do research in

this wonderful subject.

Finally, as Carl Sagan says, “What else can the exploration of Universe be, other than a journey in self-discovery!” Indeed it has been!

PREFACE

Astrophysics, or the study of heavens is a very vast area of research. We want to understand how the Universe behaves overall and what do its various constituents tell us. With a subject as intriguing as astrophysics, where each subfield is equally engrossing, one wants to *understand it all.* However it is not quite possible to cover very many topics in the few years of graduate research. Nevertheless, I pursued two widely different topics of research for my dissertation. As a result, this thesis consists of not one single complete work but is based on two different projects I have worked on in the last few years of my initiation into research in Astrophysics, and it represents my small effort towards understanding this amazing Universe *via* the two different studies I undertook: *one*, to comprehend the overall dynamics of the Universe as reflected by the 1st project; and *two*, to understand the nature of one of it most exotic beings as reflected by the 2nd project. These are as follows:

Project 1: *Acceleration of the Universe and Modified Gravity*: Covered in Chapters 1-5, this project aims to understand the reason behind the recent acceleration of the Universe using the tools of Galaxy Cluster Cosmology.

Project 2: *Chemical Evolution in Quasars*: Covered in Chapters 6-10, this project studies the metallicity in Quasars with strong Nitrogen lines and compares the findings from this study to the results of Chemical Evolution Models of Quasars.

TABLE OF CONTENTS

Appendices

LIST OF TABLES

LIST OF FIGURES

Images in this dissertation are presented in color.

Chapter 1: Cosmology: Understanding The Universe

Cosmology, the scientific study of origin and evolution of the Universe, has been around since times immemorial. However the last 25 years have marked the start of a new epoch in the history of this ancient science. During these years, cosmology essentially got reinvented from a pure theory based discipline to a largely observational and data driven science. With the bombardment in precision data taken from ground and space based telescopes, and many large-scale surveys taking place now and coming up in the near future, we are increasingly living in an era which offers the possibility of testing the foundational theories of cosmology with unprecedented accuracy.

1.1 The Accelerating Universe

About a decade ago when two research teams, *High Z Supernovae* [Reiss et. al., 1998] and *Supernovae Cosmology Project* [Perlmutter et. al., 1999], published the analysis of their observations and measurements of Type IA Supernovae, their result came as a shock not only to these scientists but it resonated almost as a supernova explosion with the entire scientific community. The data from these surveys provided strong evidence that the Universe has recently entered a phase of accelerated expansion and this has been confirmed further by numerous supernovae (SNe) observations since then. Of late, the Cosmic Microwave Background (CMB) observations have also provided a strong support to this [Larson et. al., 2010], indirectly, by verifying the flatness of the Universe which when combined with the measurements of the mean matter density (Ω_m) of the Universe, imply the existence of Dark Energy which is theorised to result in the acceleration of the Universe. No doubt the accelerated expansion of the Universe, as is indicated by numerous observations, has been among the most important breakthoughs of the last century which has forced us to reanalyse the way we think about the composition and dynamics of the Universe.

1.1.1 Problem With The Standard Model Of The Universe

The standard cosmological model is based on Einstein's General Relativity (GR) applied to an expanding Universe which is homogeneous and isotropic on large scales. These two (*Einstein's GR* and *the assumption of homogeneity and isotropy*) are the foundational ideas of this widely accepted model of Nature. The standard cosmological model very well explains much of the observed behaviour of the Universe and has seen many successes, e.g., the Big Bang Nucleosynthesis.

The Einstein's Field Equations (EFEs) are given as,

$$G_{\mu\nu} = 8\pi T_{\mu\nu} \tag{1.1}$$

(in the units of $c = 1$) and where, ($G_{\mu\nu} = R_{\mu\nu} - g_{\mu\nu}R/2$), is defined as the *Einstein Tensor.*

Here, the expression on the left represents the curvature of spacetime as determined by the metric and the one on the right represents the matter energy content of the Universe.

It has gradually become clear in recent years that either one or both of these foundational ideas of standard cosmological model, with ordinary particles, is not suffcient to describe what we observe. For example, this model does not explain the observed rotation curves of galaxies, as well as the recently discovered late time cosmic acceleration. In order to explain these observations, it is necessary to assume either a new gravitational dynamics or new components of the cosmic energy budget or, perhaps, both. In the next few paragraphs we touch upon both these explanations briefly.

1.1.2 The Repulsive Gravity Term

Ever since Sir Isaac Newton was hit by an apple in the 1600s till the end of last century, the defining feature of Gravity has been its "attractive" nature. However, when Einstein formulated GR he allowed for gravity to push as well as to pull, by including a "repulsive" term proportional to the metric tensor, $g_{\mu\nu}$, in order to make the Universe static, neither expanding nor contracting as was believed at that time,

$$G_{\mu\nu} = 8\pi T_{\mu\nu} - g_{\mu\nu}\Lambda \tag{1.2}$$

It does not matter where we put this additional term, either to the RHS (as above) or LHS like the following,

$$G_{\mu\nu} + g_{\mu\nu}\Lambda = 8\pi T_{\mu\nu} \tag{1.3}$$

However, the "static" Universe so formed was practically unstable and robbed the EFEs of their "formal beauty". More importantly, the observations of the expanding Universe proved that the cosmological constant was not necessary. This led Einstein to discard the "repulsive" part altogether and so did most scientists until the SNe Ia results were published in the late 1990s.

Today the EFEs sans the cosmological constant term do not explain the accelerating expansion of the Universe, and an additional term is needed for the observations and theory to match. The term featuring *repulsive gravity* or *Einstein's cosmological* *constant* Λ, when put back into the EFEs, does explain the accelerated expansion phenomenon. But what is the physical explanation of Λ?

Explanation 1: Λ As Dark Energy

Gravity is still an attractive force for all the known forms of matter and energy. In simplest terms, an additional term involving Λ on the RHS of EFEs represents the presence of hitherto undetected energy which will account for $\sim$ 75% of the mass-energy content of the Universe. This mysterious form of energy with strange properties that give rise to repulsive gravity has been broadly termed as "Dark Energy".

It can be represented by writing the EFEs as,

$$G_{\mu\nu} = 8\pi T_{\mu\nu} + 8\pi T^{dark}_{\mu\nu} \tag{1.4}$$

where, now the EFEs are modified by adding the second term on the RHS which represents Dark Energy.

Explanation 2: No Mysterious Dark Energy but GR needs a "space-time" modification on large scales

In a sense, the argument presented above also represents a "modification" of the EFEs wherein the "energy content" of the Universe is modified to make way for repulsive dark energy. Instead modification of the LHS side of EFEs by adding an additional term can also explain the accelerating Universe and this leads us to the broad topic of "modified gravity" (MG). The motivation behind this approach is that the geometry of the Universe has not yet been tested on cosmological scales even though it is known to work to a high degree of accuracy on the solar system [Shapiro, 1964; Will, 2001] and the stellar [Hulse and Taylor, 1975] scales in its present form. EFEs with modified gravity can, in general, be represented as,

$$G_{\mu\nu} + G_{\mu\nu}^{dark} = 8\pi T_{\mu\nu} \tag{1.5}$$

where the modified part is represented by the second term on the LHS, lumping together all kinds of modified gravity theories in this term.

There exist countless flavours of MG. Examples of the MG theories include Braneworld Gravity theories e.g., DGP theory [Dvali, Gabadadze and Porrati, 2000] which seek the solution to cosmic acceleration by introducing extra space-time dimensions; and Scalar-Tensor gravity theories [Caldwell and Linder, 2005] which introduce new scalar degrees of freedom to induce acceleration.This new topic has seen some frenzied activity in recent years however we will not delve into the details of these MG models here, except for a very brief introduction of the DGP gravity model which will be used for structure growth comparison with the GR model in later Chapters.

DGP Gravity Model

DGP gravity model [Dvali, Gabadadze and Porrati, 2000] is the modified version of the GR gravity model with 5 dimensional (5D) Minkowski space. The usual 4D space-time, which we are used to, is embedded in these five dimensions. The 4D Newtonian gravity emerges on a 3-brane in this 5D space-time model of the Universe. The extra dimension is infinite in size. As a result the Einstein-Hilbert action term in this model has two parts: a 4D GR term and a 5D extra dimensional term. The usual 4D term is dominant at short distances whereas the 5D term becomes important as we go to large scales of the order of current size of the Universe.

The main motivation behind introducing this model (and many such MG models) was to explain the acceleration of the Universe without the need for dark energy. The acceleration of the Universe implies weakening of gravity. Since the acceleration has started only recently, it might imply that the gravity weakens only at large scales in the Universe. According to the Gauss' Law of Gravity, the force of gravity for normal 3+1 D Universe $\propto 1/r^2$. However as we increase the number of spatial dimensions, each extra dimension would increase the exponent in Newton's gravitational law weakening the gravity. For a 4+1 D Universe, the force of gravity thus becomes $\propto 1/r^3$.

In a Universe where DGP is the underlying gravity model, this alteration in the gravitational force results in different (slower) growth rate of structure formation. This alteration in the history of structure formation by virtue of its slower growth rate as compared to GR gravity model can be tested by counting the galaxy clusters as we will be see in later Chapters.

Explanation 3: Backreaction

Yet another direction of work on this problem taken by some physicsts involves relaxing the second foundational idea of cosmology: the assumption of homogeneity and isotropy of the Universe [e.g., Futamase, 1996; Brandenberger, 2002]. It is argued that since homogeneity is an approximate assumption, a note must be taken of how the inhomogeneities on smaller scales affect the evolution of the metric variables as per Newton's third law. This has been termed as gravitational backreaction of small scale inhomogeneities, whereby gravitational waves propagating in background spacetime affects its dynamics and hence its evolution. We will not go any further into the details of this approach for the purpose of this project.

1.1.3 This Project

This first part of the thesis is a study that attempts to see whether we can determine, using galaxy cluster survey data, which of the two main competing theories (Dark Energy or Modified Gravity) is responsible for the acceleration of the Universe. Our tool of choice for this work would be the upcoming galaxy cluster surveys that will search for galaxy clusters over more than 10% of the sky. If we are to detect the difference between the two, it would provide us with a better understanding of how the Universe works. The path appears rather simple but as we will see, many roadblocks are encountered on the way, mainly because the astrophysics of clusters is not sufficiently well known. Much of this thesis deals with how to take into account those astrophysical caveats while on our journey to discover whether Nature still swears by GR with missing "Dark Energy" or needs "space-time" modification or whether the picture will still be hazy a few years from now and new methods need to be devised to solve this problem. Before proceeding further in this direction, let us step back and recapitulate our knowledge of the building blocks of Modern Cosmology.

1.2 A Short History Of The Universe

According to the most accepted hypothesis, the Universe began with "Big Bang", a violent explosion that occured about 15 billion years ago. Ever since it has been expanding with its dynamics governed by its matter and energy contents. The Universe consists of matter and radiation as its "known" building blocks. The standard cosmological model with its "known" constituents cannot explain all the mass needed to explain observations of galaxy rotation curves. This matter which does not emit light is yet to be detected *directly* and is aptly termed as "Dark Matter" and accounts for $\sim 22\%$ of the mass-energy budget under the new cosmological standard model [e.g., Ostriker and Steinhardt, 2003]. In addition, the rest and most of the energy balance to explain acceleration of the Universe is lumped under "Dark Energy".

1.2.1 Expansion History Of The Universe

Prior to the 1920s it was generally believed that our Universe is static, centered on the Milky Way galaxy. This view received a major shakedown when systematic motions of recession were measured for spiral nebulae and the fantasy of a static Universe was finally toppled in 1929 when Edwin Hubble announced his velocity-distance law

[Hubble, 1929], also known as the *Hubble's Law* ($v = H_0 * r$), which tells us that Universe is expanding with galaxies moving away from one another. EFEs provide the theoretical basis for describing the dynamics of the Universe. For a uniformly expanding Universe, which is also homogeneous and isotropic, these reduce to the Friedmann Equation:

$$\left(\frac{\dot{a}(t)}{a(t)}\right)^2 = H^2(t) = \frac{8\pi G\epsilon(t)}{3c^2} - \frac{k}{a(t)^2} \tag{1.6}$$

where, $\epsilon(t)$ represents the energy density and k represents the curvature of the Universe. $a(t)$ is the scale factor and is related to redshift by, $a = (1+z)^{-1}$

Rewriting the expansion in terms of separate energy densities,

$$H^2(a) = H_0^2[\Omega_m a^{-3} + \Omega_r a^{-4} + \Omega_k a^{-2} + \Omega_\Lambda] \tag{1.7}$$

where Ω's are the different energy density components for the matter, radiation, curvature and constant dark energy, respectively, in terms of the critical energy density $\rho_{cr0} = 3H_0^2/8\pi G$, which is the current energy density for a flat Universe.

Once again, the Friedmann equation can be written as a sum of all the different energy density components,

$$H^2(t) = \frac{8\pi G}{3}\sum_i \rho_i \tag{1.8}$$

Separating the matter density term from the sum we can write this as,

$$\frac{H^2(a)}{H_0^2} = \Omega_m a^{-3} + \sum_{i'} \Omega_{i'} \exp\left(3\int_a^1 [1 + w_{i'}(a')]\frac{da'}{a'}\right) \tag{1.9}$$

or,

$$\frac{H^2(a)}{H_0^2} = \Omega_m a^{-3} + \frac{\delta H^2}{H_0^2} \tag{1.10}$$

where the set i' does not include matter part and $w(a)$ refers to the equation of state of each component [Linder, 2005]. We can think of the δH^2 part of the equation above as being either due to an energy density component or as a modification of the Friedmann equation and interpret it to be related to some "acceleration physics" responsible for accelerated expansion of the Universe. If we define,

$$w(a) = -1 - \frac{1}{3}\frac{d \ln \delta H^2}{d \ln a} \tag{1.11}$$

The effective acceleration physics equation of state can then be written as,

$$w(a) = -\frac{1}{3}\frac{d \ln[\Omega_m(a)^{-1} - 1]}{d \ln a} \tag{1.12}$$

where,

$$\Omega_m(a) = \Omega_m a^{-3}/(H(a)/H_0)^2 \tag{1.13}$$

Different cosmological models can have the same expansion history if their $\Omega_m(a)$ and $w(a)$ are the same. Even high precision measurements of the expansion history of the Universe are therefore not sufficient to distinguish the different physical origins for the same expansion behaviour, and hence the true nature of the acceleration of the Universe cannot be studied by expansion history alone.

1.2.2 Growth History Of The Universe And Structure Formation

The Universe is homogeneous and isotropic only on scales larger than $\sim$ 100 Mpc. Any window below that size will reveal inhomogeneties that exist in the form of galaxies and stars, planets, animals and so on. This structure we see in the form of galaxies and clusters has resulted from initially tiny fluctuations in the matter density, which were present in the early Universe.

The Matter Power Spectrum

At some early time in the history of the Universe, these fluctuations in matter density can be represented by an overdensity field. The overdensity at any given location is given by [e.g., Voit, 2005],

$$\delta(x) = \frac{\rho(x) - \bar{\rho}}{\bar{\rho}} \tag{1.14}$$

where $\bar{\rho}$ is the average matter density.

The Fourier components of the overdensity field can be written as,

$$\delta_k(k) = \int \delta(x) e^{ikx} d^3x \tag{1.15}$$

For the isotropic case, the power spectrum of the matter density field is defined as,

$$P(k) \equiv \langle |\delta_k|^2 \rangle \tag{1.16}$$

The power spectrum essentially describes the amount of fluctuation power contained in at different length scales, k^{-1} and hence gives a complete statistical description of the initial fluctuations from which the later structures emerged.

A related and equally important concept is the "variance in mass". Variance in mass within identical volume elements corresponding to the length scale k^{-1} is given by,

$$\frac{\delta M(r)}{M} = \int \delta(x) W(|x - r|) d^3x \tag{1.17}$$

where, $W(r)$ is a spherical window function which goes to zero outside comoving radius r and whose integral over all space is unity. The variance in mass on this scale is then given by,

$$\sigma^2 \equiv \left\langle \left| \frac{\delta M}{M} \right|^2 \right\rangle = \frac{1}{(2\pi)^3} \int P(k) |W_k|^2 d^3k \tag{1.18}$$

where, W_k is the Fourier transform of $W(r)$.

An important cosmological parameter in the Cold Dark Matter models of structure formation is the mass variance at the length scale of $8h^{-1}$ Mpc, also known as σ_8. Observations suggest that the variance in mass is of the order unity at that length scale, $\delta M/M \sim 1$. This has been the motivation for expressing the normalisation of power spectrum in terms of σ_8.

$$\sigma_8^2 = \frac{1}{(2\pi)^3} \int P(k) |W_k|^2 d^3k \tag{1.19}$$

where W_k is the Fourier transform of $W(r)$ with r is the comoving radius having a value of $8h^{-1}$ Mpc.

Growth Of Initial Fluctuations

As the Universe expands, gravity acts, and as a result overdense regions become more overdense and underdense regions become more underdense. After a certain limit when the amplitude of a perturbation becomes non-linear, it will separate from the Universe and collapse to form separate structures like the galaxies and galaxy clusters we see in the Universe today.

The growth of perturbations with time in the linear theory is given by,

$$\ddot{\delta}_m + 2\frac{\dot{a}}{a}\dot{\delta}_m = 4\pi G \rho_m(a) \delta_m \tag{1.20}$$

The second term in the above equation features the Hubble expansion and acts as a frictional term. The term on right hand side features gravity and acts as a forced driving term. The perturbations grow as long as the gravitationally driven force term is greater than damping introduced by Hubble expansion, and matter dominates.

IMPORTANCE OF GROWTH HISTORY

It can be seen from the above equation that, in GR the gravitational constant G is a constant of nature and therefore the growth history of the Universe is completely determined by the expansion history, $\dot{a}/a$. Any discrepancy between the growth observed and growth predicted by the observed expansion history will be able to test the theoretical framework and reveal the possible modifications needed.

GROWTH FUNCTION

The function used to describe the growth of linear perturbations is called the growth function, $D(a)$. For a simple case of a density fluctuation in the form of a uniform density sphere which is slightly denser than its surroundings, its growth function can be approximated by,

$$D(a) \sim \frac{\delta\rho}{\rho} \sim \frac{\dot{a}}{a} * \int_0^a \frac{da}{\dot{a}^3} \tag{1.21}$$

where, the growth function $D(a)$ is normalised at present times, $D(1) = 1$. The rate of growth of fluctuations is scale independent, meaning all fluctuations grow at the same rate. In the general case with dark energy, the growth function cannot be solved analytically and at best can be approximated for different epochs in the evolution of the Universe. Several different and useful approximate expressions exist for the growth function. For a Universe with negligible radiation density, Wang and Steinhardt (1998) derive a useful approximation,

$$D(a) \sim a * \exp\left(\int_a^1 (1 - [\Omega_m(z)]^{\alpha_w})\frac{da}{a}\right) \tag{1.22}$$

with α_w defined such that,

$$\frac{d\ln\delta}{d\ln a} = [\Omega_m(z)]^{\alpha_w} \tag{1.23}$$

where, $\Omega_m(z)$ is the matter density at z in terms of critical density $\rho_{cr0} = 3H_0^2/8\pi G$.

This will be revisited in the next Chapter where we will see how the growth history of the Universe can be described by one single parameter.

In order to differentiate between various gravity theories and to understand the physical mechanism behind the dynamics of the Universe, it is essential to measure the growth of structure as well. In GR the growth history of the Universe is completely determined by its expansion history. Therefore, comparing the expansion history and growth history would be an ideal test of the underlying physics. Any discrepancy between the two would point towards modifications of GR on cosmological scales.

1.3 Cluster Cosmology

1.3.1 Cluster Of Galaxies

Galaxies are gregarious in nature, mostly. They are preferentially found in associations, either in groups, which generally have about ≤ 50 galaxies or in still larger agglomerations called the galaxy clusters. A cluster of galaxies typically has anywhere from ~ 50 galaxies (a poor cluster) to some thousands of galaxies (a rich cluster) within a space of about $6h^{-1}$Mpc across. Clusters are the largest and most massive gravitationally-bound objects in the Universe as of now. They are semi-independent, self-gravitating units that have detached from the Hubble Expansion recently.

The mass of a typical galaxy cluster is $\sim 10^{14} - 10^{15}h^{-1}M_\odot$, $(h \equiv H(z)/H_0)$ The Mass-to-Light ratio of clusters reveals that most of the cluster's mass emits no light and exists as "Dark Matter". Much of the "normal" mass in a cluster exists in the form of hot gas ($\sim 10^7 - 10^8 K$). Some of this gas accumulated over the ages when mass was unlocked from stars in galaxies and then probably was pushed outside of a galaxy's potential well by catastrophic events triggered by violent mechanisms such as SNe explosions and mergers of galaxies. Most of the intracluster gas never collected into stars and now occupies most of the cluster's volume. The gas loses energy through thermal bremsstrahlung and its characteristic X-ray spectrum is usually used to determine the cluster mass. The spectrum of a cluster is used to find its temperature. Assuming that the galaxy cluster is in hydrostatic equilibrium, and approximating the cluster to be a singular isothermal sphere, the gas temperature then can be related to its mass through a simple equation,

$$k_B T = (8.2\,\mathrm{keV}) \left(\frac{\mathrm{M}}{10^{15}\mathrm{h}^{-1}\mathrm{M}_{\odot}} \right)^{2/3} \left(\frac{\mathrm{H(a)}}{\mathrm{H}_0} \right)^{2/3} \tag{1.24}$$

The third term in above equation shows that the $M-T$ (or any mass-observable) relation *evolves* with time. Departures from the hydrostatic equilibrium assumption are usually not large. However, for any cosmological study, adequate care must be taken to account for the dispersion that exists in any such relation.

1.3.2 Clusters As Cosmological Probes

Clusters are the largest collapsed structures in the Universe. They are also huge and luminous which makes them very detectable even from very large distances. Hence they are excellent candidates for studying the structure growth over cosmological scales and times. The number density of clusters in a comoving volume element traces the large-scale structure growth. The large scale structure growth is exponentially sensitive to cosmological parameters like σ_8 and a statistical analysis of this growth in the form of cluster counting can put powerful constraints on the underlying cosmology governing the Universe, including the forces responsible for its newfound acceleration. A study of the evolution of cluster number counts over a redshift interval can therefore provide powerful constraints on cosmological parameters.

1.3.3 Problems With The Cluster Counting Method

A galaxy cluster survey with a large yield and having a well understood cluster redshift distribution is an invaluable probe of cosmology. However, unbiased and precise constraints require an understanding of the nature of cluster mass-observable relations.

The only astrophysical parameter on which cluster number density depends is its mass. Cluster mass is not a directly observable quantity and we need to infer it from some directly observable quantity such as its temperature or luminosity. However mass-observable scaling relations are not very well established mainly because the astrophysics of clusters is not well known. As a result there exists considerable scatter in such relations.

Evolution of these mass-observables in redshift domain as well as in mass domain and the scatter present therein is another problematic aspect of cluster scaling relations that is not well known. These uncertainties not only lead to degradation of constraints but can also lead to biased and possibly faulty estimation of cosmological parameters, and for our case it might just masquerade as a possible wrong signal for a different gravity theory which will make this whole exercise of growth function detection pointless if enough care is not taken into consideration. These topics are further explored in Chapter 2.

1.3.4 Cluster Surveys

Many galaxy cluster surveys, ongoing and in the past, have progressively improved our knowledge of the dynamics of the Universe. Coupled with new advances in telescope technology as well as improved theoretical understanding derived from advances in other areas of research like the CMB; precision cosmology using large scale cluster surveys is giving us exciting new results. Some of the surveys completed or in operation now are as follows:

Sloan Digital Sky Survey (SDSS)

The SDSS is the biggest sky survey to date and is described in detail in Chapter 7 later on when we talk about the second project that forms Part B of this thesis. SDSS, however, it is not exclusively a galaxy cluster survey in a strict sense. Nevertheless, the cluster data from SDSS have been used to put some very interesting constraints on various cosmological parameters like σ_8 [Rozo et. al., 2009].

Red Sequence Cluster Survey (RCS)

The RCS Survey was designed exclusively to identify a large sample of galaxy clusters over a wide range of redshifts. Two optical telescopes, The Canada-France-Hawaii 3.6 m for the northern hemisphere and Cerro-Tololo Inter-American Observatory 4 m telescope for the southern hemisphere were used for this survey, with a sky coverage of 90 deg^2. The study resulted in improved constraints on cosmological parameters including Ω_m and σ_8 [Gladders et. al., 2009].

Massive Cluster Survey (MACS)

MACS was derived from the ROSAT (Rontgensatellit) All-sky survey done using the German X-Ray Satellite Telescope, which ended its mission in the late 1990s.

Together with other X-ray Surveys like the Bright Cluster Survey (BCS) and REFLEX (the ROSAT-ESO flux-limited X-ray sample), the data from MACS has been used to obtain statistically significant constraints on the cosmological parameters [e.g., Mantz et. al., 2008].

Grand as they may be, the present galaxy cluster surveys however have not been able to reach the point of precision where they are capable of distinguishing between the Dark Energy and Modified Gravity models of acceleration of the Universe, among other unanswered questions of cosmology. In the coming decade, ever bigger and better galaxy cluster surveys will see the light of day. These surveys will arm us with even more statistical power with catalogues containing tens to hundreds of thousands of galaxy clusters based on various selection criteria having a quality and quantity unmatched before. Let's now take a look at some of the upcoming surveys:

South Pole Telescope Survey (SPT)

The first of the large cluster surveys using the Sunyaev-Zeldovich (S-Z) effect [Sunyaev and Zeldovich, 1970], SPT is presently conducting a survey over 4000 $\deg^2$ of southern sky using a 10 metre diameter telescope based in Antarctica.The *S-Z effect* is the Compton up-scattering of CMB photons by gravitationally bound hot gas in clusters and this creates a local distortion in the CMB blackbody spectrum. The SPT is expected to yield many thousands of clusters out to high z. One of the main attractions of an S-Z based detection is that it is essentially redshift independent and hence a survey like SPT can detect clusters out to very high redshifts as opposed to optical or X-ray surveys which are limited in this area [Staniszewski et. al., 2009].

PLANCK

ESO's PLANCK is a major space based mission which has been mapping the whole sky bit by bit for the past one year, looking for CMB anisotropies, with unprecedented sensitivity ($\Delta T/T \sim 2 * 10^{-6}$) and angular resolution better than 10 arcmin. As a side job, it will also yield a catalogue of hundreds of thousands of S-Z detected galaxy clusters [Tauber, 2004].

Large Synoptic Survey Telescope (LSST)

This is the biggest optical ground based wide-field survey coming up in the next decade. It will use a 8.4 m telescope to scan 20,000 $\deg^2$ of the southern sky with each patch of sky repeatedly scanned 1000 times in a span of 10 years [*www.lsst.org*].

Dark Energy Survey

Dark Energy Survey (DES)[www.darkenergysurvey.org] is a deep optical-near infrared survey which aims to map a 5000 deg^2 patch of the southern sky with a 500 Mega Pixels CCD Camera mounted on a 4-metre telescope. It will make extensive observations in in g, r, i, z bands within a redshift up to, $z \sim 1.3$. They will detect clusters and supernovae as well as make measurements of weak lensing.

eROSITA

Extended ROentgen Survey with an Imaging Telescopic Array or eROSITA is a German X-Ray instrument that will fly on board the Russian satellite Spectrum-X-Gamma, which is scheduled to be launched from Baikonur in 2012 [ref., eROSITA Mission Document, 2005]. eROSITA is expected to perform an All-sky survey as well as a wide field survey of nearly half the sky in the medium X-ray range up to 10 keV with an unprecedented spectral and angular resolution. One of the main motivations behind the design of this instrument is to unravel the nature of the force responsible for the acceleration of the Universe. It is expected to detect around a hundred thousand galaxy clusters within its flux-limit of $\sim 1.0 * 10^{-15}$ ergs/sec.

Wide-Field X-Ray Telescope Survey

Wide-Field X-ray Telescope (WFXT) is a proposed NASA mission which will be performing three extragalactic sky surveys in the soft X-ray band (0.4 keV - 6 keV) with a sky coverage of 20,000 deg^2. With a sensitivity and angular resolution far better than achieved ever before and a flux-limit, $f_x \geq 3 * 10^{-14}$erg/s/cm^2, it intends to generate a dataset of $\geq 500,000$ galaxy clusters up to a $z \sim 2$.

The comparison of survey parameters for some of the past, ongoing and the next generation X-Ray galaxy cluster surveys is shown in Figure 1.1 [Murray et. al., 2010].

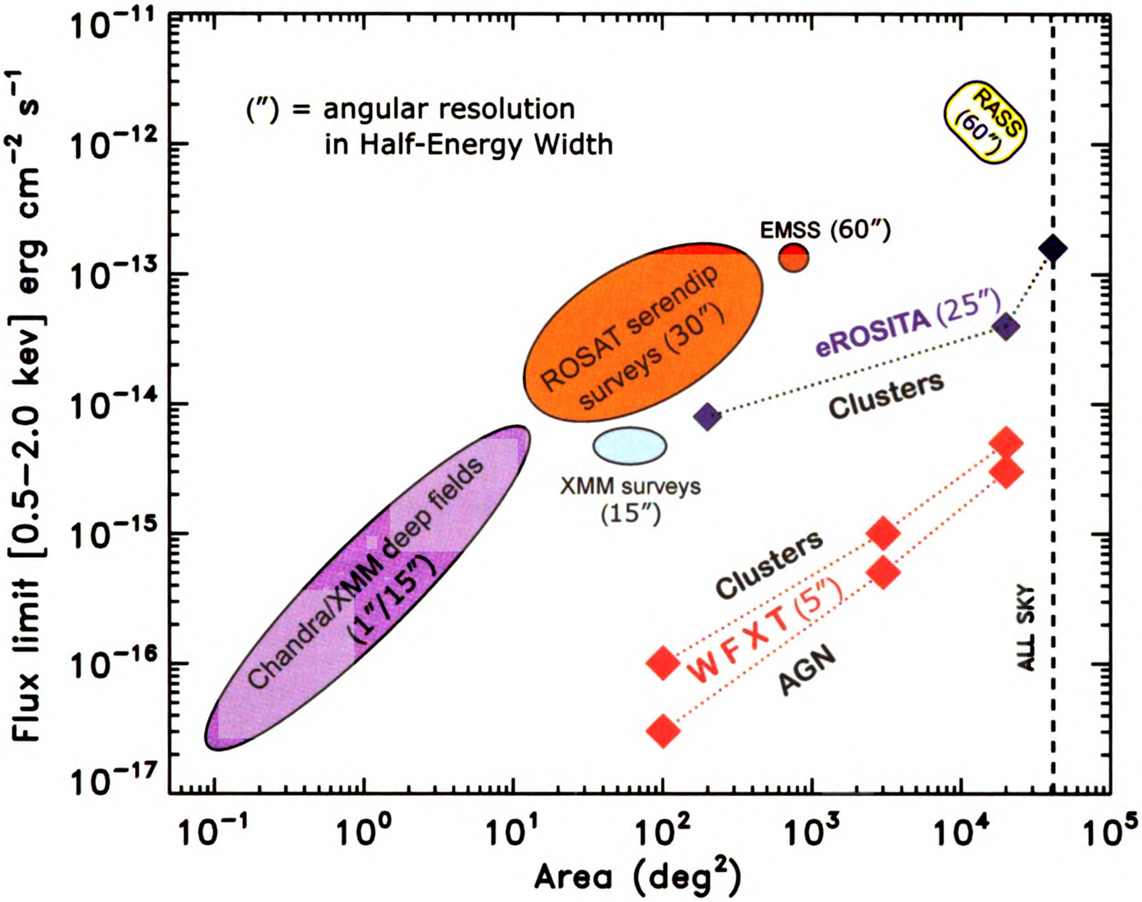

Figure 1.1 *This figure shows the comparison of survey parameters, the effective flux-limits and sky coverage for past, current and upcoming X-ray galaxy clusters (taken from Murray et. al., 2010).*

1.4 Conclusion

From this Chapter, we learned that:

The Universe is expanding and this expansion is accelerating. In order to explain this acceleration, The Standard Model of the Universe needs a *Dark Energy* component or GR needs a *modification* on large scales. We intend to see which of these theories is correct. The expansion history of the Universe is not sufficient to distinguish between them since both of these can result in the same expansion, thereby resulting in no conclusion. Therefore it is important to study growth history of the structure formation in the Universe as competing gravity theories will result in different growth history.

In this project we plan to study the growth history using the galaxy clusters, using the statistical power of upcoming surveys. However the inherent problems in this method exists due to the insufficient knowledge of the implications of astrophysical processes going on in galaxy clusters. Taking into account the uncertainty due to this, our goal in this project is to see if the next generation surveys will be able to rule out one or the other of these theories while trying to ascertain the nature of cosmic acceleration.

CHAPTER 2: THE BASICS

In order to inch towards an understanding of the underlying cause of acceleration of the Universe, one needs to know whether GR is valid on large scales or not. One way to test GR on large scales is to study the growth history of density perturbations in the Universe *independently* of the expansion history, since GR makes very specific predictions about how perturbation growth is linked to expansion history.

2.1 GROWTH FUNCTION PARAMETERISATION

Growth of linear density fluctuations in the Universe over a period of time is characterised by the Growth function $D(a)$, the slope of which determines the growth rate of structure. One such model independent parameterisation of the growth function is given by the following equation [Peebles, 1980; Wang and Steinhardt, 1998; Linder 2005; Linder and Cahn, 2007],

$$D(a) = a * g(a) = a * \exp\left(\int_0^a [\Omega_m(a)^\gamma - 1]\frac{da}{a}\right) \tag{2.1}$$

where, $g(a)$ gives the growth rate at a given time. Here a single parameter γ (the gravitational growth index) can signal a deviation of the growth function from the predictions of GR. Figure 2.1 shows the difference between the growth functions of GR gravity model and DGP gravity model. The difference between the two models increases at higher z's.

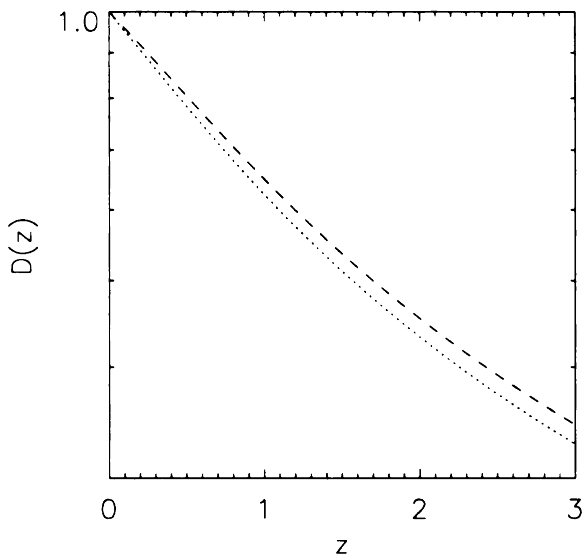

Figure 2.1 *Growth Function plotted as a function of z, for the GR gravity model (dotted line) and the DGP gravity model (dashed line).*

Another advantage of such parameterisation is that for the GR directed growth, γ is confined to a narrow range of values near 0.55, independent of the nature of the dark energy models, so we can focus on the one question we are interested in answering for the purpose of this thesis: How well γ can be constrained by a large galaxy cluster survey to measure the growth function, $D(a)$?

2.2 Growth History From Galaxy Clusters

Observing the evolution of galaxy clusters over a period of time can give us powerful insights about the growth history of the Universe and can therefore reveal the nature of the dynamical forces governing the Universe on cosmological scales. Because of this tremendous cosmological implication, counting of galaxy clusters at different redshifts in a given comoving volume of space has become a very important area of research in cosmology.

2.2.1 Cluster Mass Function

The most important physical property of a galaxy cluster for cosmological purposes is its mass. The Cluster Mass Function is defined as the number density of clusters greater than mass M at a redshift z in a comoving mass element. The following is a good approximation of the cluster mass function [Voit, 2005],

$$n_M(M,z) = \frac{\Omega_m \rho_{cr0}}{M} \mathrm{erfc}\left(\frac{\delta_c}{\sqrt{2}\sigma(\mathrm{M,z})}\right) \tag{2.2}$$

Here, δ_c represents the critical threshold density contrast δ, with a value of 1.686 above which a density perturbation collapses and virializes. The differential mass function on mass scale M and redshift z is then given by,

$$\frac{dn_M}{d\ln\sigma^{-1}} = \sqrt{\frac{2}{\pi}} \frac{\Omega_m \rho_{cr0}}{M} \frac{\delta_c}{\sigma} \exp\left(-\frac{{\delta_c}^2}{2\sigma^2(M,z)}\right) \tag{2.3}$$

where,

$$\sigma(M,z) \equiv D(z) * \sigma(M) \tag{2.4}$$

where, $\sigma(M)$ is given by Eqn. (1.18) and is normalised to σ_8. And, $D(z)$ is a strong function of Ω_m and γ as seen in Eqn. (2.1).

We see from Eqn. (2.2) above that the number density has an exponential dependence on various cosmological parameters *via* $\sigma(M,z)$. The large-scale structure growth is therefore exponentially sensitive to these cosmological parameters and a statistical analysis of this growth in the form of cluster counting can put powerful constraints on the underlying cosmology governing the Universe, including the forces responsible for its newfound acceleration.

The growth rate of galaxy clusters can be assessed by measuring the cluster mass function, meaning that we need to *weigh* the clusters in a survey. Now, since a cluster "mass" cannot be "observed", we need a physical property of clusters which can be directly observed, *a mass-observable*, and a well calibrated relation linking the observable property to cluster mass. But first of all how is a cluster's mass defined?

2.3 Mass Of A Galaxy Cluster

2.3.1 Defining The Cluster Mass

Observational studies have indicated that the velocity dispersion of galaxies in a cluster remains relatively constant, which implies that the underlying matter density in the cluster diverges with its radius, $\rho_M(r) \sim r^{-2}$. A consistent definition of *cluster mass* is, therefore, needed in order to measure the cluster mass function because a cluster's mass and all the relations linking that mass to its observable quantities depend on how one defines the outer boundary of a galaxy cluster.

Mass of a galaxy cluster is defined as M_Δ which is the amount of matter contained in a spherical region of radius r_Δ with a mean density of $\sim \Delta * \rho_{cr}$. While observing clusters, the factor Δ is usually taken to be 200 or 500. It has been shown that using Δ taken to be 200 leads to a mass-velocity dispersion relation which is independent of cosmology [Evrard, 2004] and is the preferred definition in cluster simulations as well. We will use this definition of a cluster's mass, M_{200}, the mass contained within a radius r_{200}, for the purpose of this work.

2.3.2 Observing The Cluster Mass: Mass-Observable Relations

Of the many observables of galaxy clusters used as proxy for mass, gas temperature and X-ray luminosity have been the most popular choices.

Mass-Temperature Relation

The deep potential wells of galaxy clusters compress the intergalactic baryonic gas and heat it to X-ray emitting temperatures. This gas temperature, therefore, reveals the depth of a cluster's potential well and is inferred from the cluster's X-ray spectrum. In most clusters, the intergalactic gas seems to be close to hydrostatic equilibrium. Using this assumption a relation between gas temperature and the cluster's mass can be derived.

$$T_X = T_0 \left(\frac{M}{M_0} \right)^{\alpha_{MT}} \tag{2.5}$$

where T_0, M_0 and α_{MT} are the normalisation and exponent parameters, respectively, which define the Mass-Temperature relation. However, the relation is only an approximate one because several systematic as well as astrophysical processes going on in clusters affect the ideal behaviour outlined above.

Mass-Luminosity Relation

A galaxy cluster's mass can also be inferred from the correlation between mass and its X-ray luminosity and is of the general form,

$$L_X = L_0 \left(\frac{M}{M_0} \right)^{\alpha_{ML}} \tag{2.6}$$

which is defined by the normalisation parameters, L_0 and M_0 and the exponent of the relation, α_{ML}. This correlation is not as tight as that between mass and temperature. However, one advantage of using luminosity as a mass tracer is that it is easier to measure than the gas temperature.

2.3.3 Evolution Of The Mass-Observable Relation

All mass-observable relations evolve with redshift. One of the reasons is that the definition of mass used in these relations is linked to the critical density of the Universe ρ_{cr} (the energy density required for flat Universe), $M_{\Delta}(z) \sim \Delta * \rho_{cr}(z)$. Since the Universe is expanding, for a given mass M, clusters would be hotter earlier in time than now because the density was greater. This leads to an inclusion of z dependent term in the mass-observable relations. In addition to the evolution of the mass-observable relation due to the expansion of the Universe, the physics of galaxy formation and evolution may also result in additional evolution of these relations. In light of the above discussion, we rewrite the $M - L$ relation as,

$$L = L_0 \left(\frac{M}{M_0}\right)^{\alpha_{ML}} \left(\frac{H(z)}{H_0}\right)^{\beta} \tag{2.7}$$

The parameter β is an index giving the strength of this evolution. For the *self-similar* models where the expansion of the Universe is the only source of evolution of the $M - L$ relation, this parameter takes a value of 7/3.

2.3.4 Scatter In Mass-Observable Relations

The mass-observable relations described above are not exact and there exists considerable scatter in such relations as has been shown by various observational studies of clusters [Pratt et. al., 2009]. Figure 2.2 shows the amount of scatter present in the $M - L$ relation from one such study, [Popesso et. al., 2005].

The presence of scatter in such relations is a large source of uncertainty in studies involving estimation of cluster mass using a mass-observable. For the cosmological studies, it is very important to take this into account due to the exponential dependence of cluster mass function on cluster mass.

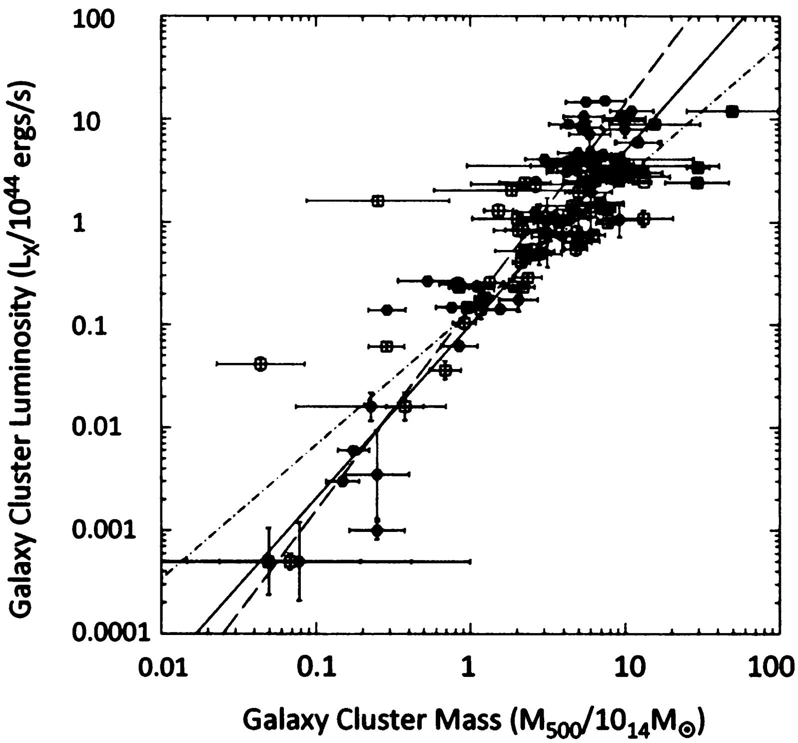

Figure 2.2 *(from Popesso et. al., 2005) This figure shows the presence of scatter in $M - L$ relation in galaxy clusters.*

Evolution In Scatter

It is also possible that the scatter present will be different at different z. This evolution in the presence of scatter in the mass-observable relations can be due to many factors. One reason could be that at earlier times when the clusters were in the primitive stage of formation, the proportion of *relaxed* clusters might be smaller than at late times [e.g., Pratt et. al., 2009], resulting in higher amount of scatter. This evolution in scatter also needs to be taken into account for a complete study in addition to the scatter itself. The scatter in the $M-L$ relation is parameterised by following equation,

$$\sigma_{ml} = \sigma_{ml0}(1 + z)^{\eta} \tag{2.8}$$

where, σ_0 gives the scatter present in the M-L relation currently and its evolution in time is given by the term $(1 + z)^{\eta}$, with η as the index describing the evolution strength of scatter in z. In addition to its evolution with z, scatter may also depend on mass M, leading to a *mass* dependent term in its definition,

$$\sigma_{ml} = \sigma_0(1+z)^\eta * M^\psi \tag{2.9}$$

with ψ giving the strength of evolution of scatter with M.

2.4 Counting The Clusters: Redshift Evolution Of The Cluster Number Density

The evolution of cluster number counts in redshift space is a powerful function of the underlying cosmology and therefore can give tight constraints on various cosmological parameters. Since we can only observe some mass-proxy, we are actually observing the redshift evolution of that observable.

For a cluster sample in a given survey, we can find the number of clusters dN within a given solid angle $d\Omega$ in a redshift bin dz, lying between $[z, z+dz]$, that fall into the range $[X, X+dX]$ of the mass-observable X, defined by relation $X(M,z)$. The redshift evolution of the cluster mass function is then given by [Voit, 2005],

$$\frac{d^3N}{dXd\Omega dz}(X(M,z),z) = \frac{dn_M}{dX}(X(M,z),z) * \frac{d^2V_{co}}{dzd\Omega}(z) \tag{2.10}$$

where, dn_M/dM is the mass function evolution factor and $d^2V_{co}/dzd\Omega$ is the comoving volume element. How accurately we can tell about the background cosmology is heavily dependent on how well we understand mass-observable relation as well as its evolution with the redshift. The cluster number count at a given z is then given by,

$$\frac{dN}{dz} = \frac{dV}{dz}(z)\int_M \frac{dn_M}{dM}(M,z)dM \tag{2.11}$$

where, the first term gives the volume of the region in the redshift interval dz at z, and the second term gives the number density of clusters of *all* masses that are there. This is what we would see *ideally* if we had a perfect telescope with no flux-limit and could scan the full sky. In the real world that does not happen and therefore in addition to the usual cosmological parameters, galaxy cluster detection is sensitive to the survey parameters such as the flux-limit and solid angle coverage. At far away distances low luminosity clusters will not be seen if the flux-limit of a survey is high. This flux-limit is implemented by having a *selection function*, $f(M, z)$, for the survey to describe the cluster number counts.

$$\frac{dN}{dz} = \frac{dV}{dz}(z) \int_M \frac{dn_M}{dM}(M, z) f(M, z) dM \tag{2.12}$$

Instead of *mass* we observe *luminosity* thus what we measure is,

$$\frac{dN}{dz} = \frac{dV}{dz}(z) \int_{L_{min}}^{L_{max}} \frac{dn_M}{dL}(l, z) f(L, z) dL \tag{2.13}$$

Also because of the fact that $M - L$ relation is not perfect and there exits considerable scatter in this relation, the above expression for cluster number count gets modified as,

$$\frac{dN}{dz} = \frac{dV}{dz}(z) \int_{L_{min}}^{L_{max}} \int_M \frac{dn_M}{dM} P(L|M) f(M, z) dM dL \tag{2.14}$$

where, $P(L|M)$ is the probability density for a cluster of mass M to have a luminosity L. For our luminosity range we use $L_{min} = 10^{40}$ erg s^{-1} and $L_{max} = 10^{47}$ erg s^{-1}. All the clusters lie roughly in this luminosity range. However the flux-limit of the survey generally imposes a more stringent constraint on L_{min} which goes on increasing as we go higher in z, since L is a function of z. The minimum observable luminosity at a given z is given by,

$$L_{min}(z) = f_x * d_l^2(z) = f_x * (r(z) * (1 + z))^2 \tag{2.15}$$

where, d_l is the *luminosity* distance, r is the coordinate distance to redshift z and f_x is the flux-limit of the survey.

In addition to z, their redshift evolution, the cluster number counts also evolve with mass. The cluster number density at a given z is a strong function of *mass*, as can be seen from Eqn. (2.2).

2.5 Cluster Power Spectrum

2.5.1 Cluster Bias

Observations have long shown that galaxy clusters show a spatial bias towards other clusters, that is, they tend to cluster with one another [Bahcall and Soneira, 1983; Bahcall et. al., 2003]. The fluctuation in the number density of galaxy clusters on large scales is much more pronounced than fluctuations of the underlying matter density. This is quantitatively characterised by a *bias parameter* $b(M)$, which gives the ratio of the fluctuation in the number density of clusters of mass M to the perturbation amplitude of the matter density.

$$\frac{\delta N_M}{N_M} = b(M) * \frac{\delta \rho_m}{\rho_m} \tag{2.16}$$

The bias parameter is taken to be independent of the length scale as long as that length scale is large compared to that of a galaxy cluster. An analytic expression for $b(M)$ is given by [Sheth and Tormen, 1999; Mo and White, 1996]

$$b(M, z) = 1 + \frac{a\delta_c^2/\sigma^2 - 1}{\delta_c} + \frac{2p}{\delta_c(1 + (a\delta_c^2/\sigma^2)^p} \tag{2.17}$$

with, $a = 0.75, p = 0.3$.

2.5.2 Measuring The Cluster Power Spectrum

The power spectrum of the spatial distribution of galaxy clusters is given by,

$$P_{cl}(k, z) = b_{eff} * P(k, z) \tag{2.18}$$

where, b_{eff} is the cluster mass function averaged linear cluster bias $b(M, z)$ and is given by [Majumdar and Mohr, 2004],

$$b_{eff} = \frac{\int dM(dn/dM)b(M, z)}{\int dM(dn/dM} \tag{2.19}$$

For the primordial power spectrum of density perturbations, $P(k) \sim k^{n_p}$, the matter power spectrum at later stages of Universe is given by,

$$P(k, z) = D^2(z) * T^2(k) * k^{n_p} \tag{2.20}$$

The symbol k refers to the comoving modes with wave number $(1 + z)k$ in physical space corresponding to the comoving length scale k^{-1}. The parameter n_p is the spectral index of the primordial density perturbations.

The Transfer Function, $T(k)$ is a function which encapsulates in it the overall effect of the modification of the primordial power by different scale-imprinting processes like the effects of pressure, and dissipation of density perturbations due to streaming particles, except for those involving mode growth in the non-linear regime. $T(k)$ gives the ratio of the late-time amplitude of a density perturbation mode to its initial value [Peacock, 1998],

$$T(k) \equiv \frac{\delta_k(z = 0)}{\delta_k(z)D(z)} \tag{2.21}$$

the normalisation redshift z here, is taken to be arbitrary, so long as it refers to a time before any scale of interest has entered the horizon and $\delta_k(z)$ reflects the original power spectrum imprinted by inflation or some other process. Several fitting forms exist for the matter transfer function [e.g., Bardeen et. al., 1986; Peacock and Dobbs, 1994]. A well known fitting form for the matter transfer function for cold dark matter (CDM) cosmologies that account for all baryon effects in the large-scale structure regime is given by Eisenstein and Hu (1999).

The average cluster power spectrum over a wide comoving space between z_{min} and z_{max} is then given by [Majumdar and Mohr 2004],

$$\bar{P}_{cl}(k) = \frac{\int_{z_{min}}^{z_{max}} dz(dV/dz)n^2(z)P_{cl}(k,z)}{\int_{z_{min}}^{z_{max}} dz(dV/dz)n^2(z)} \tag{2.22}$$

Since the integration is weighted over comoving number density of clusters, the $\bar{P}_{cl}$ depends not only on cosmology, but also on the specific survey used for counting the clusters since their detection as well as their redshift dependence depends on the survey definition used.

The uncertainty in measuring the cluster power spectrum is given by, σ_{p_k}, ([Feldman et. al., 2004; Tegmark, 1997]),

$$\sigma^2_{P_{cl}} = \frac{4\pi^2 \bar{P}^2_{cl}(k)}{k^3 V_{eff}} \tag{2.23}$$

where V_{eff} is the *effective* volume utilized for measuring the power at mode k and is defined as [Tegmark, 1997],

$$V_{eff}(k) \equiv \int \left[\frac{\bar{n}(r)\bar{P}_{cl}(k)}{1+\bar{n}(r)\bar{P}(k)}\right]^2 d^3r \tag{2.24}$$

Here, $\bar{n}(r)$ gives the expected number density of galaxy clusters in the given survey at z. Only those regions where the cosmic signal $\bar{P}_{cl}(k)$ is greater than the Poisson shot noise $1/\bar{n}(r)$, will be contributing towards the effective volume, with little contribution from the other regions.

2.6 Fisher Matrix Technique Of Finding Constraints

After we get the information in different forms from different aspects of cluster detection, we need to process that information quantitatively as well as qualitatively. One widely used method of forecasting survey constraints is by using the Fisher formalism to form a Fisher Information Matrix and extract quantitative information from it. The Fisher Information Matrix translates errors on observed variables measured in a given survey into constraints on parameters of interest in the underlying model. It is an elegant way of doing propagation of errors in the case of multiple correlated measurements and observations based on some underlying multiple parameter model.

The Fisher Information of a likelihood function $L(\theta)$ is a measure of the amount of information a data set m carries about a parameter θ. If we have a cosmological model which is fully specified by such a set of parameters θ_i, the Fisher Information Matrix is then defined formally as the expectation value of the derivatives of the log of the likelihood with respect to the parameters,

$$F_{ij} \equiv -\left\langle \frac{\partial^2 \ln L}{\partial\theta_i \partial\theta_j} \right\rangle \tag{2.25}$$

where, L is the likelihood function of the given model.

2.6.1 Fisher Information From Redshift Evolution Of Galaxy Clusters

The redshift evolution from cluster survey is constructed by binning the cluster number counts in redshift. The likelihood function for an observable will be then proportional to dN/dz. The Fisher Matrix for the redshift evolution of cluster number counts is then constructed as [Holder et. al., 2001],

$$F^s_{ij} = \Sigma_n \frac{\partial N_n}{\partial \theta_i} \frac{\partial N_n}{\partial \theta_j} \frac{1}{N_n} \tag{2.26}$$

where, the matrix is summed over n redshift bins over the survey detection range z_{min} to z_{max}. N_n is the cluster number counts in a given bin n.

2.6.2 Fisher Information From Galaxy Cluster Power Spectrum

The sensitivity of the redshift-weighted cluster power spectrum $\bar{P}_{cl}$ to different parameters is studied using the Fisher Information Matrix which is constructed as follows [Majumdar and Mohr, 2004],

$$F^p_{ij} = \Sigma_m \frac{\partial \bar{P}_{cl}(k)}{\partial \theta_i} \frac{\partial \bar{P}_{cl}(k)}{\partial \theta_j} \frac{\Delta k_m}{\sigma^2_{P_{cl}}} \tag{2.27}$$

where, we sum over n bins in $k-$space between k_{min} and k_{max}.

$\sigma_{P_{cl}}$ is the variance in calculation of $\bar{P}_{cl}(k)$, and is given by Eqn. (2.19).

2.7 Problems And Their Possible Solutions

After collecting the information in form of cluster number counts and cluster power spectrum, we construct the respective Fisher Matrices to constrain different parameters of interest as described above. This, however, does not promise to be a straightforward formalism in getting tight constraints on various parameters. Several problems are encountered when the method described above is implemented both because of the nature of cosmological model as well as the non-direct detection of a galaxy cluster's mass.

2.7.1 Degeneracy Between Different Parameters

There exist complex correlations not only between different cosmological parameters but also between mass-observable scaling relations, which end up making the constraints on those parameters highly degenerate. For example, any straightforward method of measuring the cluster mass function at a particular z renders the parameters Ω_m and σ_8 degenerate.

In order to break the degeneracy which exists between various parameters we have to bring in more information from cluster surveys. As an example, the degeneracy that exists between Ω_m and σ_8 can be broken by adding information about the simple redshift evolution of cluster number counts and the shape of the cluster mass function. This is done by binning the cluster number counts not only in redshift space but also in mass space. Additional information that can be used to break degeneracies is in the cluster power spectrum. These independent pieces of information can be combined by adding up the Fisher Matrices corresponding to the each type of data.

2.7.2 Lack of Knowledge About The Mass-Observable Relations

Apart from having a strong theoretical understanding of the cluster mass function, its evolution and the selection function of the cluster survey, the most important issue concerning the cluster surveys is having a knowledge of *correct* cluster mass-observables or the *cluster scaling relations.* Uncertainties in cluster scaling relations and their evolution lead to degradation of constraints and can also lead to biased and possibly faulty estimation of cosmological parameters, and for our case it might just masquerade as a possible wrong signal for the growth function which will make these attempts to measure the growth function detection pointless if enough care is not taken into consideration.

2.7.3 Handling The Uncertainty In $M - L$ Relation: Self-calibrate vs. Only Cosmology

While modelling a survey design to estimate cosmological parameters, if the cluster scaling parameters are kept fixed, it means we are assuming *perfect* knowledge of cluster structure. This is the case of *Only Cosmology*, which however can lead to overly optimistic constraints on cosmological parameters and may well result in biased estimation of these parameters as well. One way to avoid having to *assume* perfect knowledge of cluster structure and mass-observable scaling relations is to solve for both cosmology and the cluster scaling parameters so that the survey itself *Self-Calibrates* the mass-observable scaling relations without us having to impose certain fixed values for them.

However, adding these additional free parameters will weaken our constraints on cosmological parameters which however can be improved by combining different pieces of information from a galaxy cluster survey as also mentioned in Section (2.7.1) above.

2.8 Being Realistic

The various problems and caveats in finding constraints using the Fisher formalism as mentioned above have to be properly taken into account to get realistic estimation of various parameters and particularly the growth function index γ. The next Chapter explains how we achieved this, using the following step-by-step method.

1. *Model of the Universe:* We pick a fiducial model to describe the "real" Universe having cosmological parameters' values from the best known results in literature.

2. *Model of the Cluster Structure:* For the cluster structure parameters, we use the results from the most recent results from observational studies. We also introduce the realistic estimates for parameters for the evolution of the mass-observable relations and the parameters for scatter and its evolution with z, from recent observational

studies.

3. *Redshift Evolution of the Cluster Number Counts:* We then find the redshift distribution of cluster number counts in our model Universe based on a given survey definition by binning the survey in redshift space.

4. *Information from the Shape of the Cluster Mass Function:* In addition to finding evolution of cluster number counts in redshift space, we also bin in mass-observable (luminosity) space to see how the cluster mass function evolves with redshift and mass.

5. *Information from the Cluster Power Spectrum:* We estimate the cluster power spectrum and its variance over a wide redshift range to process information from it.

6. *Varying the Model Parameters:* We then vary the model parameters of our fiducial Universe and see how each parameter affects the above three sources of information.

7. *Finding Constraints:* The constraints on various parameters are then found from the Fisher Information Matrix method, from a given information source, and for the various cases: from assuming perfect knowledge of galaxy cluster scaling relation, (Only Cosmology) to admitting the lack of this knowledge (Self-Calibration).

8. *Improving Constraints:* Finally we combine the different sources of information and see how the constraints are improved at each step.

Chapter 3: The Survey Experiment

We conduct a theoretical experiment to access the statistical power of the next generation galaxy cluster surveys in finding constraints on various cosmological as well as cluster structure parameters. A better understanding of these parameters and how they govern the structure and evolution of the Universe is needed in order to understand the underlying cosmological framework. A perfect knowledge of galaxy cluster structure gives tight constraints even for the current survey definitions [Levine et. al., 2002]. This, however, is an overly optimistic assumption due to our incomplete understanding of galaxy cluster formation and evolution.

Lack of cluster structure knowledge, its evolution with time and the scatter present in the cluster structure scaling relations as well as its evolution will degrade our knowledge of underlying cosmology when we admit our insufficient knowledge of cluster structure parameters and let the analysis of a given survey solve, or *self-calibrate*, for these parameters itself. We are interested in understanding how this degradation happens, and given the huge power of the upcoming surveys, whether we will be able to better our understanding of both, the cosmological as well as cluster structure parameters.

Since cosmic acceleration is a major mystery of the present times, and one interesting explanation is the nature of underlying gravitational framework [Linder and Cahn, 2007], the focus of this study will be on constraining the gravitational growth index parameter γ, which is a parameter describing such a framework. For this study, our fiducial model will be the GR model with a Dark Energy component, corresponding to $\gamma \sim 0.55$. For the comparative study we will use the DGP Braneworld Gravity model [Dvali, Gabadadze and Porrati, 2000], with $\gamma \sim 0.68$, and see if the two models can be distinguished in this experiment.

In this project we intend to determine whether the upcoming galaxy cluster surveys will be able to provide strong enough constraints on γ to make this distinction. Constraints degrade when the survey must be self-calibrated, however we can model the inclusion of additional information by adding *priors*, which could come from independent studies such as weak lensing studies of galaxy clusters. In particular, we intend to see how the interplay between degradation of constraints from insufficient knowledge of cluster structure parameters, and improvement of constraints from cluster mass function and cluster bias measurements affects our ability to distinguish GR from non-GR (e.g. DGP) after the evolution of cluster scaling relations, the scatter present in such relations and its evolution have been taken into account. If the two models cannot be distinguished, we would like to know what priors from other independent studies will be needed to make a clear distinction for a given survey.

3.1 Survey Definition: Galaxy Cluster Surveys Studied

The force responsible for the acceleration of the Universe affects both the abundance and the spatial distribution of galaxy clusters. The number of clusters detected is a strong function of the type of survey definition used which in turn depends on the technological parameters of the instrument detecting clusters as well as the detection technique (e.g. S-Z Detection, X-ray, Weak Lensing, etc.). For X-ray detection of galaxy clusters, the survey definition is mainly determined by the flux-limit of the X-ray survey and the sky area to be covered by it.

Various sky surveys are in the process of implementation and/or design and were introduced in Chapter 1. Of these we study the statistical power of the surveys designed for *eROSITA*[www.mpe.mpg.de/heg/www/Projects/EROSITA/main.html] and *WFXT*[wfxt.pha.jhu.edu] [Murray et. al., 2010]. We build up mock cluster survey catalogue based on survey parameters characteristic of the surveys to be undertaken by these instruments.

3.1.1 eROSITA

eROSITA (extended ROentgen Survey with an Imaging Telescope Array) will be the primary instrument on-board the Russian satellite "Spectrum-Roentgen-Gamma" (SRG), which will be launched from Baikonur in 2012 and placed in an L2 orbit [ref.: eROSITA Mission Document].

Based on the ΛCDM cosmological model, eROSITA will discover about 50,000 – 100,000 clusters. The three surveys designed for this mission are *the All-Sky Survey*, *the Wide-Field Survey* and *the Deep-Field Survey.* The parameters for these surveys envisaged for galaxy cluster detection by eROSITA are summarised in Table 3.1.

Instrument	Survey Definition	flux-limit (erg $s^{-1} cm^{-2}$)	Solid Angle (deg^2)
eROSITA	All Sky Survey	$1.6*10^{-13}$	42,000
	Wide-field Survey	$3.3*10^{-14}$	20,000
	Deep Survey	$8*10^{-15}$	200
WFXT	Wide-field Survey	$5*10^{-15}$	20,000
	Medium Survey	$1*10^{-15}$	3000
	Deep Survey	$1*10^{-16}$	100

Table 3.1 *Survey parameter values for various surveys to be undertaken by eROSITA and WFXT.*

3.1.2 Wide Field X-Ray Telescope

The Wide-Field X-ray Telescope *WFXT* is a proposed NASA mission dedicated to performing surveys of the sky in the soft X-ray band (0.4-6 keV). Based on the ΛCDM cosmological model, the WFXT will discover about 500,000 clusters. The three surveys planned for this mission are the *Medium Survey*, the *Wide-Field Survey* and the *Deep-Field Survey*. The survey parameters for WFXT are also summarised in Table 3.1.

We wish to see which survey and which instrument would be most effective in constraining the parameters studied.

3.2 Modeling The Universe

3.2.1 The Cosmological Parameters

The large-scale structure as well as the expansion history of the Universe is essentially contained in a few cosmological parameters which are given below. For our *most probable* model, we use the values of these parameters from the latest WMAP7 results [Larson et. al., 2010] which gives the most confident results to date. The values for the same are given in Table 3.2.

1) Density Parameters give the density of an energy component at present times in terms of critical density parameter ρ_c.

(a) Ω_m, This gives the total matter density in the Universe at present and is given by, $\Omega_m = \Omega_c + \Omega_b + \Omega_n$, where Ω_c, Ω_b and Ω_n are the cold dark matter, baryon and neutrino density parameters respectively.

(b) Ω_r, gives the radiation density at present times.

(c) Ω_Λ is a term to account for the acceleration of the Universe. Based on the latest WMAP7 results we take our model Universe to be flat. Therefore, $\Omega_\Lambda = 1 - \Omega_m - \Omega_r$.

2) w is the equation of state for the Dark Energy.

3) σ_8, gives the root-mean-square fluctuations of overdensity within spheres of $8h^{-1}Mpc$ radius and is given by Eqn. (1.19). It is used in the normalisation of the matter power spectrum $P(k)$.

5) Hubble Constant H_0, gives the current rate of expansion of the Universe.

6) n_p, is the index of the primordial power spectrum.

7) Gravitational growth index parameter γ: This parameter has a value of 0.55 for the GR model and 0.68 for the DGP model.

Models with same expansion history will have the same values for above-mentioned parameters. We will therefore use the same values of these parameters for the two models since our main aim is to study the growth history of the Universe, rather than the xpansion history.

3.2.2 Cluster Structure Parameters

The cluster structure parameters describe the model used to extract mass from some other observable property of a galaxy cluster. Since we use X-ray luminosity as the mass-observable in this study, we parameterise the Mass-Luminosity ($M-L$) relation as Eqn. (2.7) (see below),

$$L = L_0 \left(\frac{M}{M_0}\right)^{\alpha} \left(\frac{H(z)}{H_0}\right)^{\beta}$$

The values used for $M-L$ scaling parameters, L_0 and α are those given by Reiprich and Bohringer (2002). For the $M-L$ evolution parameter β, we use the value predicted by the self-similar models as has been found by recent observational studies [Pratt et. al., 2009].

The presence of scatter in $M-L$ relation and its evolution is also modelled in our fiducial cluster structure using Eqn. (2.8) (see below),

$$\sigma_{ml} = \sigma_{ml0}(1+z)^{\eta}$$

where, the value used for σ_0 is taken from Pratt et. al. (2009). We parameterise the evolution in scatter by parameter η, as shown above, however for our fiducial model we take it to be zero, meaning that in our model Universe the scatter in $M-L$

relation does not evolve with z. Table 3.2 also describes the values used for these parameters for building up our experiment.

Model	Parameter	fiducial value
Cosmology	w	-1
	n_p	0.963
	Ω_m	0.2660
	σ_8	0.801
	Ω_b	0.045
	Ω_ν	0.00
	Ω_r	0.00
	Ω_Λ	$1 - \Omega_m$
	H_0	71 km s^{-1} Mpc^{-1}
	γ	0.55 (GR), 0.68 (DGP)
Cluster Structure	α	1.81
	β	0.233
	σ_0	0.38
	η	0.00
	L_0(10^{45}erg s^{-1})	1.0
	M_0(10^{15} $M_\odot$)	1.0

Table 3.2 *Model Parameter values used for the Survey Experiment.*

3.2.3 Parameters Studied In This Experiment

For the purpose of this experiment, we assume a perfect knowledge of the expansion of the Universe as well as the primordial power spectrum index n_p. Also the Universe is assumed to be flat with Ω_Λ value determined entirely by Ω_m value. Hence in the whole study we keep H_0 and n_p fixed at their WMAP7 values and let Ω_Λ to be determined by the Ω_m value, since Ω_r has a value of zero according to the WMAP7 results. The parameters studied are Ω_m, w, σ_8 and γ. The cluster structure parameters are unfrozen successively at each step to study how they degrade the constraints.

3.3 Progression Of The Experiment: From Only Cosmology To Self-Calibration

When solving the *Only Cosmology* case for a particular survey, the mass-observable parameters for a galaxy cluster are given fixed values thereby assuming a perfect knowledge of cluster structure. This is, however, an overly optimistic assumption and may well result in a biased estimation of cosmological parameters. One way to avoid this is to let the survey solve for both cosmology and the cluster parameters or *Self-Calibrate* which is more realistic, however, it weakens the constraints progressively as more and more parameters are allowed to be free.

3.3.1 Only Cosmology:

Only Cosmology: In the case of Only Cosmology *(OC)*, all the cluster structure parameters are held constant. As a result this case gives very tight constraints on cosmological parameters. Although highly irrelevant, we study this case for reference purposes.

3.3.2 Self-Calibration:

Constraints degrade at each step of unfreezing of the cluster structure parameters. The different cases under this category are as follows.

(a) *Self-Calibration I*: When we allow only the normalisation (L_0) and the exponent (α) of the $M-L$ relation to be unknown, we call it the minimal Self-Calibration case, or *SC I.*

(b) *Self-Calibration II*: Admitting total lack of knowledge about the evolution of the $M-L$ relation and letting the evolution parameter β to be free in addition to L_0 and α makes case of self-calibrate II, or *SC II*

(c) *Self-Calibration III*: Allowing the scatter present in the $M-L$ relation and its evolution with redshift to be unknown, in addition to the rest of the cluster structure parameters, forms our full self-calibration case, or *SC III*, in which all the parameters used to model mass-observable relation, L_0, α, β, σ_0 and η, are unfrozen for the purpose of finding constraints on various cosmological as well as cluster structure parameters.

3.4 Information Gathering From Galaxy Cluster Surveys

Various bits and pieces of information are needed to prepare for the analysis of the final experiment of obtaining and understanding constraints on different parameters. These and their implications are described below.

3.4.1 Information Source 1: Cluster Number Counts

Distribution of cluster number counts at different z's is an important source of information about the growth history of the Universe because it is sensitive to the growth of density fluctuations. This redshift distribution of cluster number counts is found for different surveys. Table 3.3 gives the total number of clusters detected using the GR Model and the DGP Model for each of the surveys that were mentioned in Section 3.2.

Instrument	Survey Definition	Cluster Number Counts GR Model	Cluster Number Counts DGP Model
eROSITA	All Sky Survey	72,000	78,860
	Wide-field Survey	1,72,902	1,91,406
	Deep Survey	6316	7,039
WFXT	Wide-Field Survey	9,48,113	10,58,658
	Medium Survey	4,92,728	5,54,342
	Deep Survey	61,918	71,931

Table 3.3 *Total number of galaxy clusters detected by different survey definitions of eROSITA and WFXT for the two gravity models.*

The evolution of cluster number count with redshift from the different surveys is shown and compared in Figure 3.1. The two survey parameters on which the cluster number count and its evolution depend are its flux-limit f_x, and its solid angle coverage Ω.

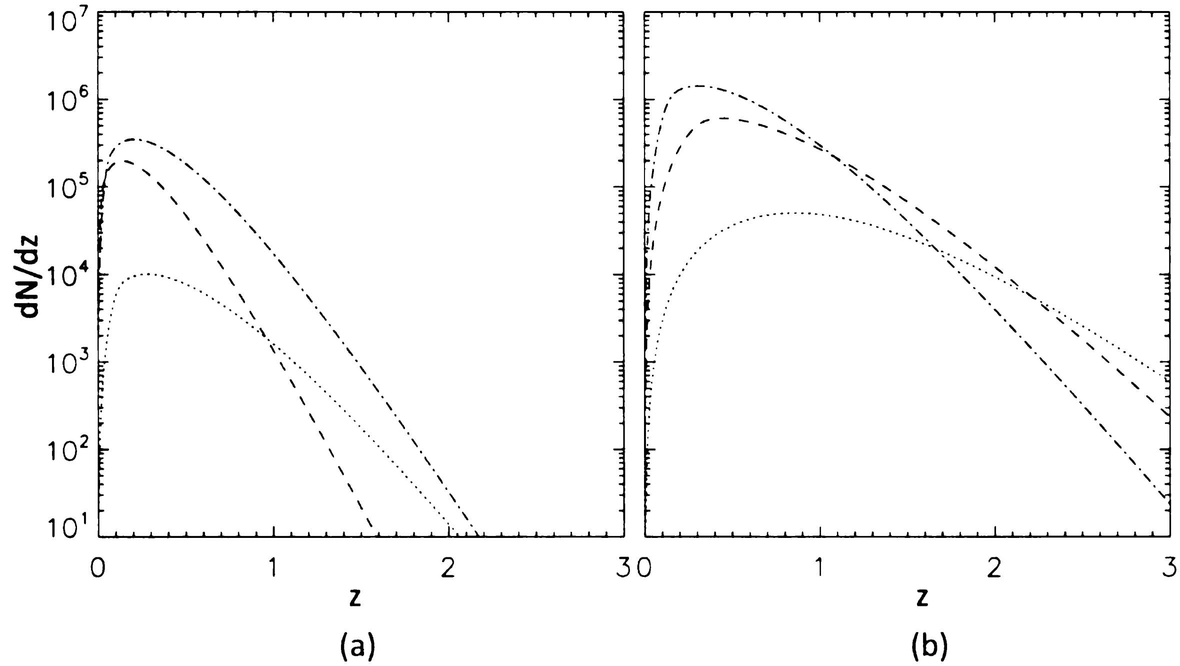

Figure 3.1 *Redshift evolution of cluster number counts based on the GR gravity model, for (a) the eROSITA wide-field (dot-dashed line), all-sky (dotted line) and deep (dotted line) surveys and for (b) the WFXT wide-field survey (dot-dashed), medium (dashed) and deep (dotted) field surveys. For a given survey DGP has more clusters at a given z. Among the two surveys, WFXT surveys detects more clusters at all redshifts and at higher redshifts where none are detected by eROSITA surveys. Of WFXT, wide-field survey detects most number of clusters in all whereas deep-field and medium surveys detect more clusters at higher z's due to their higher flux-limits.*

As can be seen from Figure 3.1, the surveys with high flux-limits are considerably more efficient in detecting not only clusters at all redshifts but they also detect clusters at highest redshift where low f_x surveys are not able to detect anything. A survey with lower f_x and higher Ω is, therefore, most effective for the purpose of counting the clusters.

Figure 3.2(a) shows the distribution of clusters per unit redshift interval from the two gravity models, and for two different surveys. For a given survey definition, the DGP model contains more clusters at any z, than the GR model. Also, the relative proportion between the two increases with z.

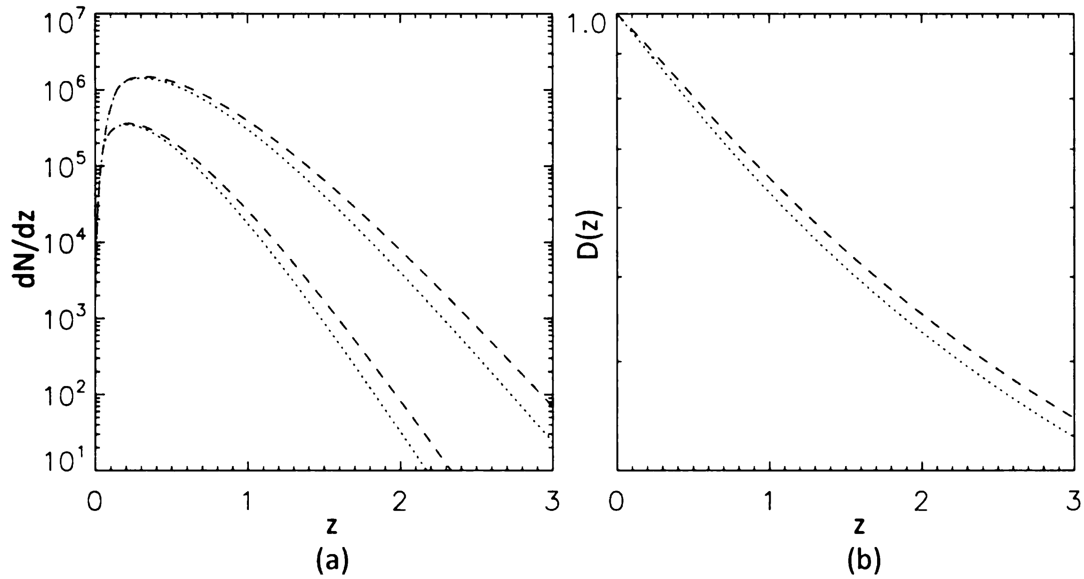

Figure 3.2 *(a) Distribution of cluster number counts per unit redshift, for the two gravity models, GR (dotted lines) and DGP (dashed lines). The higher curves are for the WFXT wide-field survey and the lower curves are for eROSITA wide-field survey. (b) Growth Function plotted as a function of z, for the GR gravity model (dotted line) and the DGP gravity model (dashed line).*

This is an implication of lower growth rate in the DGP model compared to GR model at a given z. Figure 2.1 (reproduced here as Figure 3.2(b)) shows growth function behaviour for the two cosmologies. At a given z, the growth rate is given by the slope of the growth function $D(z)$. Since the function is normalised to 1 at $z = 0$, lower growth rate results in more clusters at a given z. The effect is more pronounced at higher z's, thereby mapping the similar effect in proportionately more cluster number counts at high z. This, therefore, shows a clear distinction in the growth history resulting from the two models.

Parameter Sensitivity Of Cluster Number Count Redshift Evolution

The redshift evolution of cluster number counts is sensitive to various cosmological as well as cluster structure parameters. We studied how the change in these parameters gets reflected in the redshift cluster number count evolution. This sensitivity is shown graphically in Figure 3.3, for various parameters for the WFXT wide-field survey definition. It shows how the cluster number count per unit redshift varies when we change a given parameter by 10%.

Sensitivity to The Cosmological Parameters

(a) w: Varying w has a relatively small effect on cluster number counts at low z which, however, increases as we go to higher z's (See Figure 3.3). The effect is inverse. Increasing w decreases $N(z)$, which means, as we go to higher z's proportionately more clusters form if we have a lower w. A change $\delta w \sim 10\%$ produces only a small change $\delta N(z) \sim -4.5\%$ in total cluster number count. The dependence of cluster number counts at a given z comes *via* the redshift at which the dominance of Ω_m ends and Dark Energy starts dominating. For lower (more negative) values of w, the domination era of Dark Energy starts later. This will result in more evolution of clusters at low z. The redshift distribution of cluster number counts provides additional information *via* the expansion history. The cluster number counts in a given interval reveal the comoving volume component associated with a given interval dz, which is dependent on w.

(b) Ω_m: A change $\delta\Omega_m \sim 10\%$ produces a significant change (from 15% at low z to 96% at highest z) in cluster number counts and the percent change increases as we go back in time. The effect is directly proportional. Increasing Ω_m increases $N(z)$. Redshift distribution of the cluster number counts is highly sensitive to the matter density because of the exponential dependence of the cluster mass function on $\sigma(M)$ and $D(z)$. The dependence of $D(z)$ on Ω_m was seen in Eqn. (2.1) and the dependence

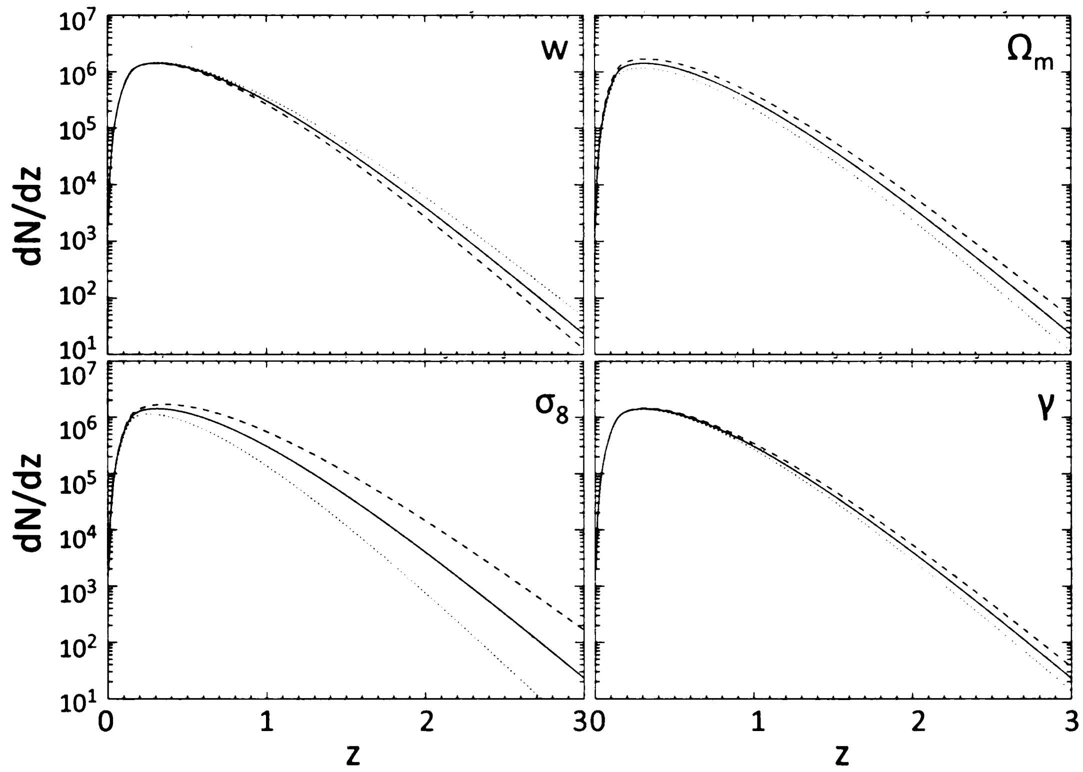

Figure 3.3 *The sensitivity of redshift distribution of cluster number counts for different cosmological parameters. The curves show the distribution of cluster number counts for a* 10% *increase (dashed lines) or decrease (dotted lines) in the parameter value. The solid curves are for the fiducial value of the respective parameter.*

of $\sigma(M)$ on Ω_m (Eqn. 1.18) comes *via* dependence of $P(k)$ on the Transfer function $T(k)$.

(c) σ_8: Change in σ_8 results in an even more pronounced change, with percent change in $N(z)$ going from 5% to 614% from lowest to highest z. Increasing σ_8 produces more clusters at all redshifts. This is a result of the exponential dependence of σ_8 on the cluster mass function.

(d) γ: This has a relatively low effect on change in cluster number counts as compared to Ω_m and σ_8. The percent change in cluster number count increases with z and reaches a high value of 50% at highest z. The dependence of $N(z)$ on γ comes *via* $D(z)$.

Sensitivity To The Cluster Structure Parameters

Of the various cluster structure parameters, the cluster number count evolution with redshift is most sensitive to α, the index of cluster structure scaling relation, followed by β, the cluster structure evolution parameter, and to a lesser extent on L_0, the normalisation of the cluster structure scaling relation.

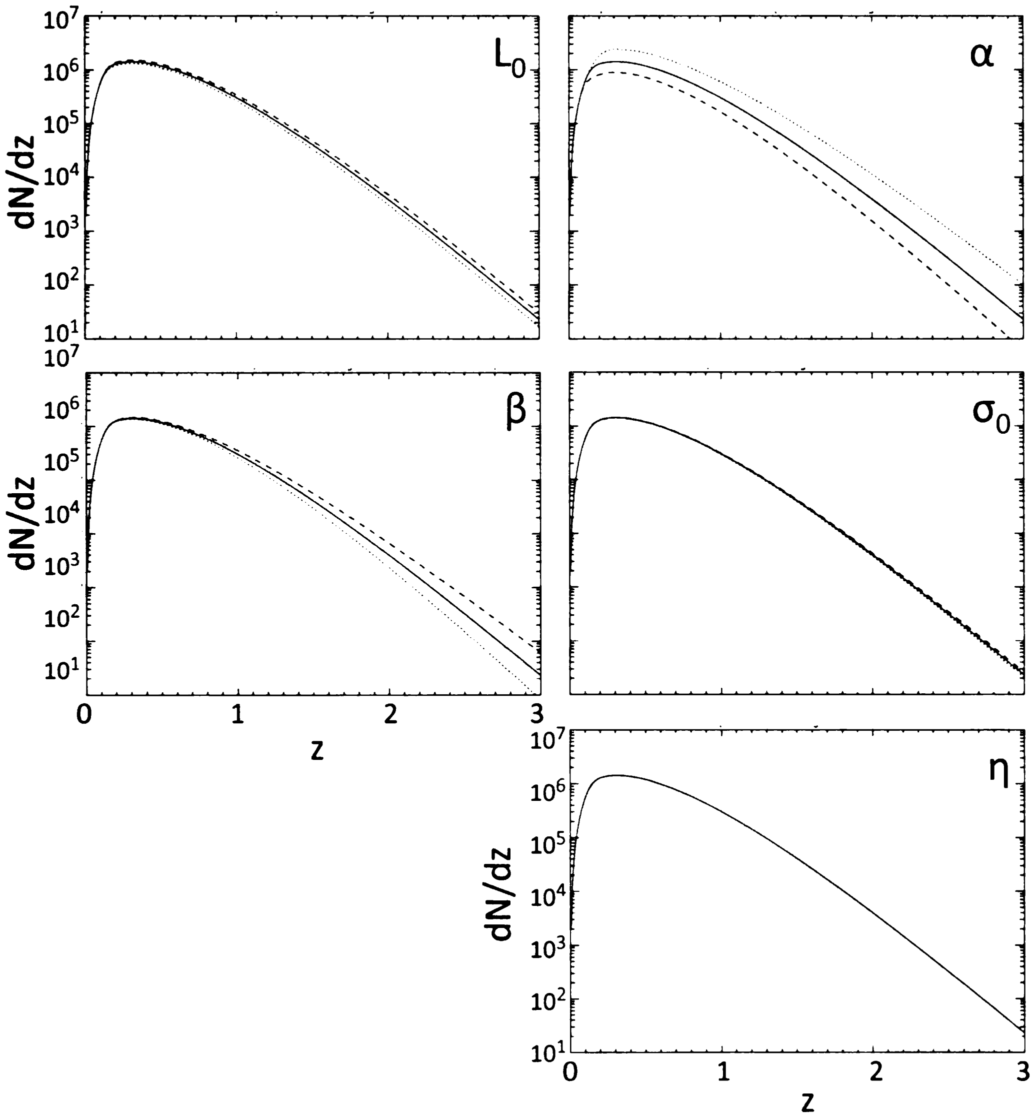

Figure 3.4 *The sensitivity of redshift distribution of cluster number counts for different cluster structure parameters. The curves show the distribution of cluster number counts for a 10% increase (dashed lines) or decrease (dotted lines) in the parameter value. The solid curves are for the fiducial value of the respective parameter.*

The scatter parameters σ_0 and η have only a marginal effect on the evolution behaviour of cluster number counts.

3.4.2 Information Source 2: Shape Of The Cluster Mass function

The cluster number density at a given z is a function of *mass* also as seen in Eqn. 2.2. The cluster number counts are, therefore, different in different mass bins at a given z, and this behaviour carries information that can be used *in addition to* their evolution with redshift to a get better understanding of how the Universe works. The variation of number density with mass comes in form of the *shape* of the function which evolves with z. In Figure 3.5 we plot the cluster mass function as a function of luminosity for three different redshifts: $z \sim 0.0$, 0.2, 0.5 and 1.0.

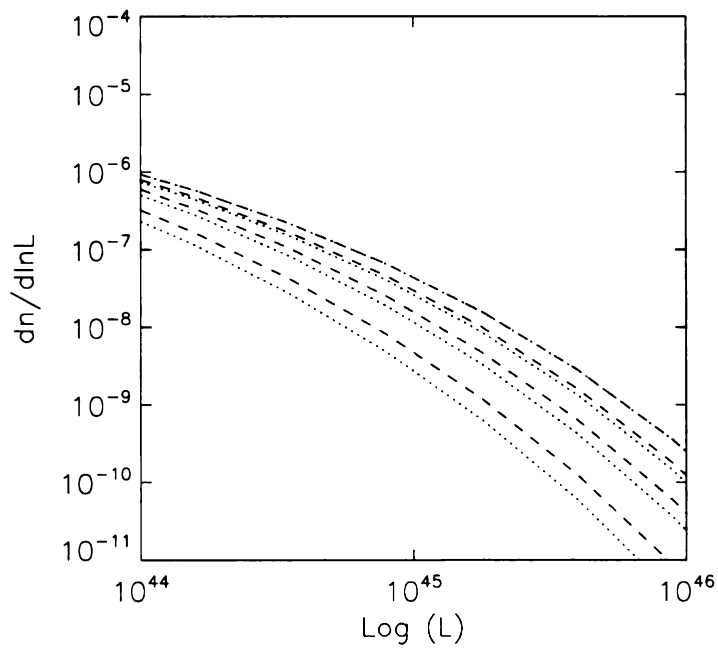

Figure 3.5 *(a) Cluster mass function evolution in mass (luminosity) for GR (dotted lines) and DGP (dashed lines) at different z's. The highest to lowest curves are from $z \sim$ 0.0, 0.2, 0.5 and 1.0 respectively. The shape of the mass function changes with z, as well as for the different gravity models.*

We see that the shape of the mass function changes with z. The shape also varies for the two gravity models, for a given z, as seen from the same figure. The difference between the two models becomes more prominent at higher z. When cluster number counts are binned in luminosity space also (which is used as our mass-proxy), the shape of the mass function and the way it changes with z provides more information in addition to the redshift evolution of the cluster mass function.

The Cluster Mass Function is a very strong function of mass M of a galaxy cluster. When the information from the shape of the mass function is added to the information from redshift evolution of cluster number counts, it improves constraints on cosmological parameters. Information from the evolution of cluster number counts with mass is therefore very essential in constraining the mass-observable relation and its evolution which is a key factor in obtaining tight constraints from the redshift evolution of cluster number counts.

Parameter Sensitivity Of Shape Of Cluster Mass Function

A change in parameter values, thereby, results in the change of the shape of the cluster mass function. Figure 3.6 shows this change in the shape of the mass function when a given parameter is varied by 10%. Of the various parameters, σ_8, Ω_m, α and L_0 are most sensitive to this variation in the decreasing order of variation strength. The $M-L$ evolution and scatter parameters are relatively less sensitive. Increased sensitivity of the cluster mass function to the cluster structure parameters results in better constraints when the cluster parameters α and L_0 are allowed to be free in an experiment.

3.4.3 Information Source 3: Cluster Power spectrum

Clusters tend to show a spatial bias towards other clusters and this peculiarity can be exploited to get more information from the cluster survey data. The Cluster Power Spectrum essentially encodes in it this biasing information and forms a vital ingredient

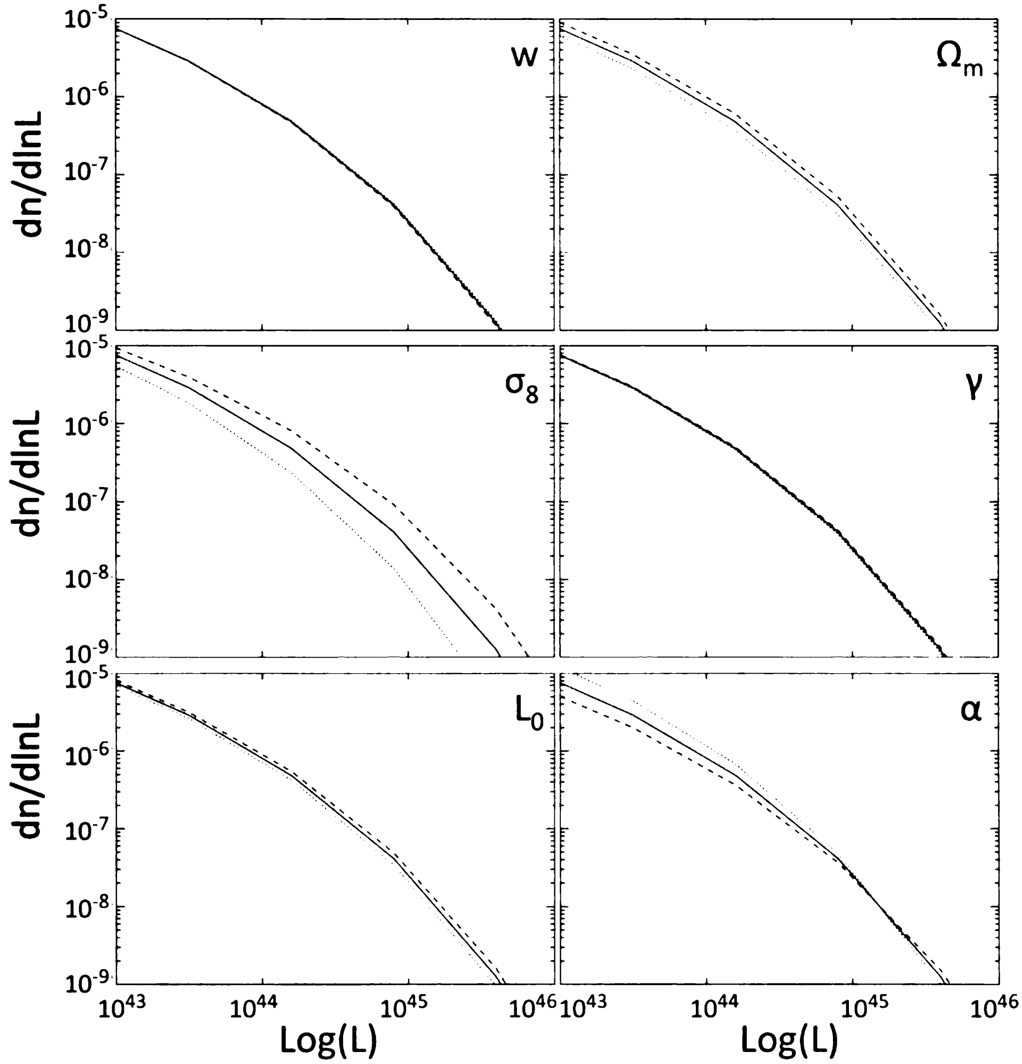

Figure 3.6 *The sensitivity of the shape of the cluster mass function for cosmological and cluster structure parameters. The curves show the change in cluster mass function evolution for a* 10% *increase (dashed lines) or decrease (dotted lines) in the parameter value. The solid curves are for the fiducial value of the respective parameter.*

in our experiment on constraining the growth history of the Universe. The amplitude and the shape of the cluster power spectrum depends on the underlying matter power spectrum and the bias of galaxy clusters. Figure 3.7 shows the cluster power spectrum for the WFXT wide-field survey and the variance in its calculation. The first source of information from the cluster power spectrum comes from its *shape* which is defined by shape of the underlying matter power spectrum. The shape reflects the Transfer

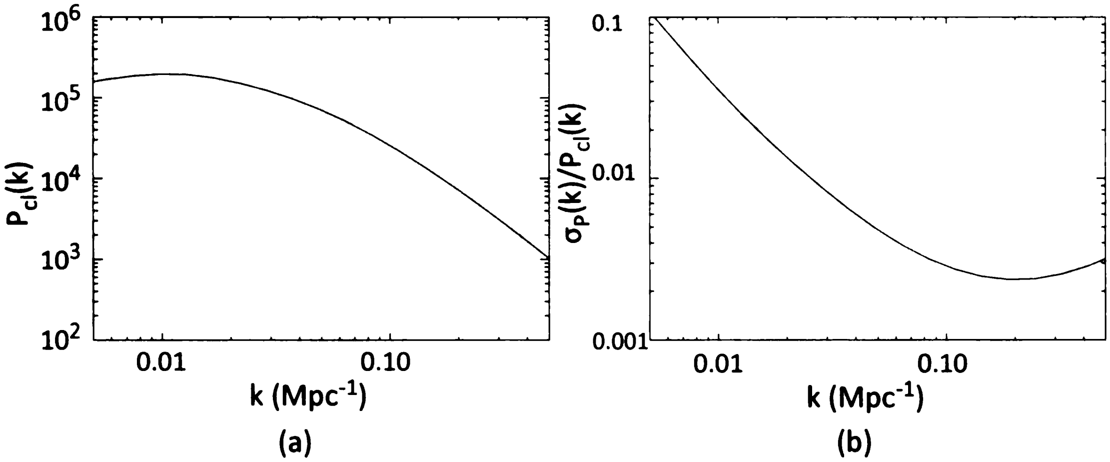

Figure 3.7 *(a) Redshift averaged cluster power spectrum for WFXT wide-field survey. (b) Fractional uncertainties $\sigma_P(k)/P_{cl}(k)$, in estimating the given cluster power spectrum.*

Function behaviour which is a very strong function of Ω_m because of its sensitivity to the redshift of the epoch of matter-radiation equality.

The second source of information is the spatial bias of clusters which is strongly dependent on the mass of a galaxy cluster. The cluster power spectrum from different surveys is essentially similar in shape as well as amplitude. However, for a given survey the power spectrum increases in amplitude as we go from low z to high z, which is opposite to the behaviour of the underlying matter power spectrum which decreases in amplitude as we go to high z. The opposite behaviour of the cluster power spectrum is a result of the bias parameter $b(M, z)$, which, for a given mass M increases with z. This offsets the decreasing amplitude of the matter power spectrum $P(k)$ and essentially reverses its behaviour in the cluster power spectrum.

The variance in the estimated cluster power spectrum $P_{cl}(k)$ increases both at the lowest and the highest k. The increase in uncertainty at the lowest k effectively shuts off the contribution to the information from the cluster power spectrum. On the other hand, the uncertainty at the highest k increases the contribution to this information. This, however, occurs in the regime where non-linear effects become important and therefore care must be taken to discard the k values when non-linearities start appearing in the estimation of the cluster power spectrum.

Parameter Sensitivity Of Cluster Power Spectrum

The cluster power spectrum is less sensitive to the variation of parameters except on Ω_m and to a lesser extent on α. It is almost insensitive to the variation in remaining parameters. This insensitivity of the cluster power spectrum is reflected in poor

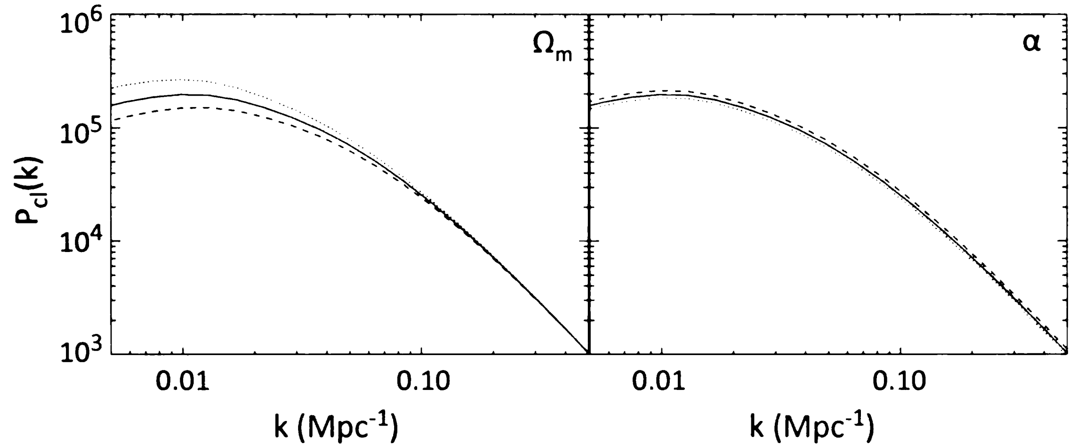

Figure 3.8 *The sensitivity of the cluster power spectrum to Ω_m and α. The curves show the distribution of cluster number counts for a 10% increase (dashed lines) or decrease (dotted lines) in the parameter value. The solid curve is for the fiducial value of the respective parameter. The cluster power spectrum is relatively insensitive to the rest of the cosmological and cluster structure parameters*

constraints on those parameters when the cluster power spectrum is used as the only source of information of the structure growth history.

3.5 Processing Information: Constructing Fisher Matrices

With the above sources of information about structure and evolution of the Universe, we determine the constraints that can be placed on the model parameters using the Fisher formalism as was described in Section 2.6.

3.5.1 Information From The Redshift-*Only* Evolution Of Cluster Number Count

We survey the redshift space over the range, $z = 0 - 3$, which is divided into 300 bins each having a width of $dz = 0.01$. Each bin is scanned for clusters in the luminosity range of $10^{40} - 10^{47}$ erg s^{-1}. Thus we use the cluster number count information from each of 300 redshift bins. The Fisher Matrix is then constructed using Eqn. (2.26) (see below) by summing over 300 redshift bins for each combination of parameter variation.

$$F^{z}_{ij} = \Sigma_n \frac{\partial N_n}{\partial \theta_i} \frac{\partial N_n}{\partial \theta_j} \frac{1}{N_n}$$

The greater the sensitivity of the cluster number counts in a bin to a given parameter, the greater the corresponding partial derivative, $\partial N/\partial \theta_i$. The Fisher Element will therefore be relatively larger for highly sensitive parameters. However, since each Fisher Element is composed of partial derivatives of two parameters, the product will therefore be coupled and the two parameters could well be degenerate. The behaviour of the Fisher Element, therefore, depends on whether the two parameters are coupled or not, which can be gauged from the corresponding information used in constructing the matrix. For the cluster number counts, Ω_m and σ_8 show degenerate behaviour.

3.5.2 Adding The Cluster Mass Evolution To The Redshift Evolution

To include the information of the shape of the mass function to the cluster number count redshift evolution, we bin the luminosity space into 20 bins in log space, in addition to, 300 bins in redshift space. The cluster counts are detected in each redshift *and* luminosity bin to construct the Fisher Element of the corresponding parameters using,

$$F_{ij}^{zm} = \Sigma_n \Sigma_m \frac{\partial N_{nm}}{\partial \theta_i} \frac{\partial N_{nm}}{\partial \theta_j} \frac{1}{N_{nm}} \tag{3.1}$$

where, n is the number of z bins and m is the number of bins in $\log(l)$ space. This way we include the mass function shape information in calculating the Fisher Matrix for redshift evolution.

3.5.3 Cluster Power Spectrum Calculations

For the purpose of cluster power spectrum calculations, the k-space is logarithmically binned into 20 bins. Also the full z-space in a given survey is divided into three wide z-bins, with each having approximately the same number of clusters. The Fisher Matrix is then constructed using Eqn. (2.27) (see below),

$$F_{ij}^{p} = \Sigma_n \Sigma_m \frac{\partial \bar{P}_{cl}(k)}{\partial \theta_i} \frac{\partial \bar{P}_{cl}(k)}{\partial \theta_j} \frac{\Delta k_m}{\sigma_{P_{cl}}^2}$$

3.5.4 Using Priors From Other Experiments

The prior on a parameter is the information that comes from some other independent study. For example, we can use priors on cosmological parameters from a Cosmic Microwave Background experiment to improve constraints on different parameters from our experiment. When we do not let any parameter vary in the experiment, it means we are using perfect knowledge of that parameter as will be done here for the curvature of the Universe, the rate of expansion of the Universe, H_0, and the primordial power spectrum index, n_p. This means that we have used full priors from the WMAP 7 results. Priors can also mean that our given parameter lies in a range of values, e.g. a 10 percent prior on α means we know that α lies in this range from some other way of finding this parameter, such as from Weak Lensing measurements. Priors are added to improve our knowledge of different parameters. This information from priors is added by constructing a *Prior Fisher Matrix*, which has all elements in it as zero except the diagonal element corresponding to the given parameter, which is given by,

$$F_{\theta\theta} = \frac{1}{\sigma_\theta^2} \tag{3.2}$$

Adding priors may or may not improve our understanding of another parameter.

The next Chapter will focus on finding constraints on various parameters using different sources of information processed using the Fisher Matrix Formalism described above and for the different cases of the Survey Experiment.

Chapter 4: Constraints From Cluster Cosmology

Using simulated galaxy cluster data based on different survey parameters of eROSITA and WFXT, we next find constraints on various parameters. Various cosmological and cluster structure parameters govern the information on the growth history which is gathered by galaxy cluster surveys. The data is processed using the Fisher Matrix formalism to extract confidence intervals on these parameters. These are plotted in the form of error ellipses which provide a convenient means of graphically interpreting the results. In Section 4.1 we will find the constraints on cosmological parameters derived from different information sources which were described in the previous Chapter. In Sections 4.2 and 4.3 we will study constraints on the gravitational growth index γ, and see if the next generation galaxy cluster surveys will have enough power to rule out either of the two gravity models: the GR and the DGP with 95% and 99% confidence.

4.1 Information Processing: Constraining Parameters

One of our purposes in this study has been to see at what stage of the experiment the constraints get worse so that we no longer can measure parameter values with sufficient certainty. Therefore, we start unfreezing the set of parameters one by one and study the degradation (or enhancement for the case of priors) at each step as we proceed through OC, SC I, SC II and SC III. In this Section we analyse 2σ constraints on the $\Omega_m - \sigma_8$ plane from the above mentioned sources of information, and study their successive degradation from OC to SC III cases for each individual information source and dramatic improvement for the case when all the three sources of information (the redshift and mass evolution of cluster counts and the cluster power spectrum) are combined.

4.1.1 Constraints From Redshift-*Only* Evolution Of Cluster Number Counts

Figure 4.1 shows 95% confidence contours on the Ω_m-σ_8 plane from the eROSITA wide-field survey for all the four cases, OC, SC I, SC II and SC III.

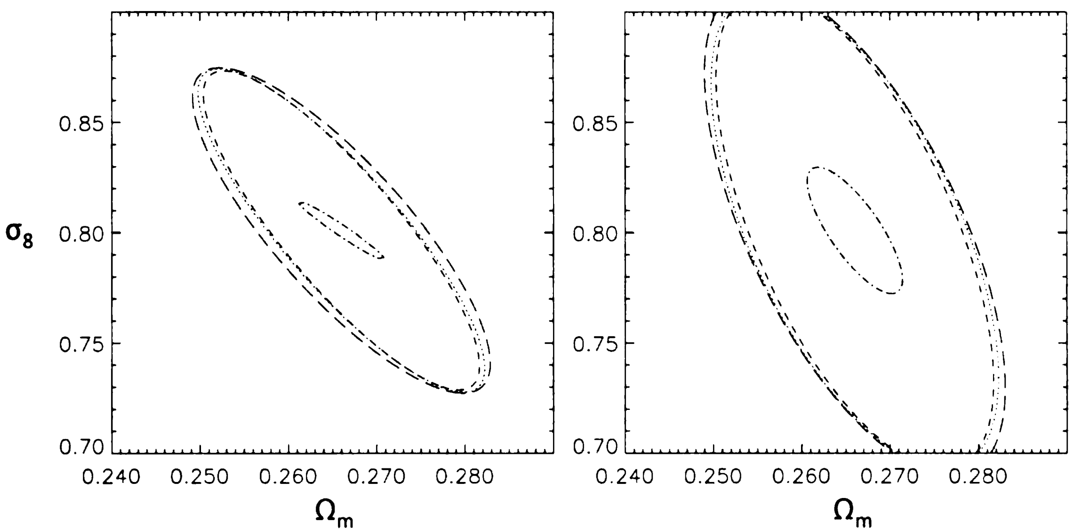

Figure 4.1 *Constraints on the Ω_m-σ_8 plane from eROSITA Wide-field Survey. The figure shows a step-by-step degradation of constraints from OC (dash-dot line) to SC I (short-dashed line) to SC II (dotted line) and finally to the full self-calibrate case, SC III (long-dashed line) for redshift-only evolution of cluster number counts when γ is held constant (left-panel) and when it is unfrozen (right-panel).*

When γ is held constant, and our only source of information is the redshift-*only* evolution of cluster number counts, the constraints on both parameters, Ω_m and σ_8

are pretty tight for the OC case, with Ω_m constrained well within $\sim 0.266 \pm 0.004$ and σ_8 having value of 0.801 ± 0.12.

These constraints degrade successively as we allow for SC I, SC II, and SC III cases; with Ω_m now constrained within $\sim 0.266 \pm 0.030$ for the SC I case and within $\sim 0.266 \pm 0.034$ for SC III case. For the redshift-only evolution, the error estimates increase by the largest percent after SC I ($\Delta\Omega_m = 0.004$ for OC and $\Delta\Omega_m = 0.03$ for SC I), when the $M - L$ relation parameters, L_0 and α are allowed to be free. There is only a little degradation on confidence contours on Ω_m-σ_8 plane when the structure evolution parameter, β and the scatter parameters, σ_0 and η are freed.

When γ is freed, the constraints for each individual case degrade. The uncertainty on Ω_m, $\Delta\Omega_m$ increases from 0.004 to 0.01 for the OC case. Figure 4.2 shows the

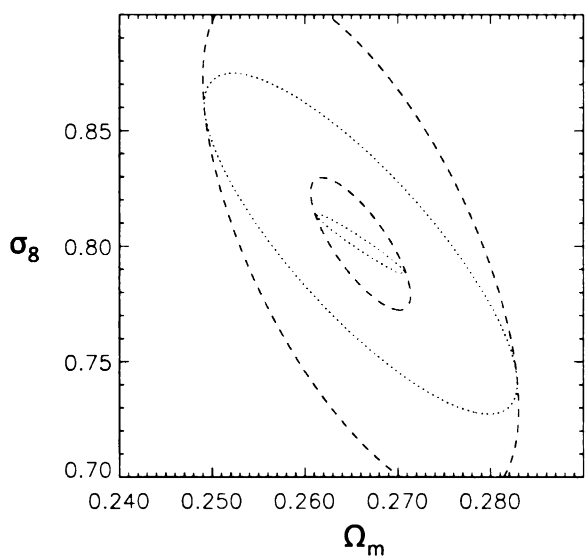

Figure 4.2 *This figure shows the relative comparison of how constraints on Ω_m-σ_8 plane degrade after making γ a free parameter for the two cases of OC (inner set of ellipses) and SC III (outer set of ellipses). The dotted lines are when γ is held constant and dashed lines are for when γ is unfrozen.*

comparison for the OC and SC III, the full self-calibrate case, when γ is held constant and when it is freed. The qualitative behaviour remains essentially the same, except that there is a little change in orientation for the two cases.

Performance Of Different Surveys

The WFXT wide-field survey will be most effective in constraining parameters primarily because of its combination of low flux-limit and large solid angle. Figure 4.3 compares the constraints in $\Omega_m - \sigma_8$ plane from different surveys when full self-calibration is allowed. The deep-field surveys are not explored here for constraining parameters owing to their small sky coverage.

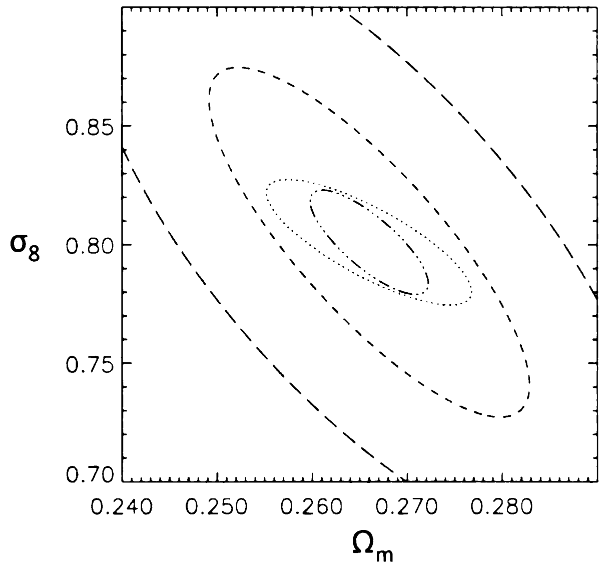

Figure 4.3 *Comparing constraints that can be obtained from different surveys to be undertaken by eROSITA and WFXT for the full self-calibrate case when γ is held constant. (eROSITA: All-sky survey - long-dashed line, Wide-field survey - short-dashed line; WFXT: Medium survey - dotted line, Wide-field survey - dot-dashed line.*

4.1.2 Constraints From Redshift *And* Mass Evolution Of Cluster Number Counts

Next we include the information about the shape of the cluster mass function by binning the clusters in luminosity space. We see the same qualitative behaviour of constraints as we go from the OC case to the SC III case (see Figure 4.4), *however* the constraints for SC cases are significantly improved, with the constraints on Ω_m for

SC III case improving from $\Delta\Omega_m = 0.034$ (from redshift-only information) to 0.006 (from redshift and mass evolution information) as shown in Figure 4.4.

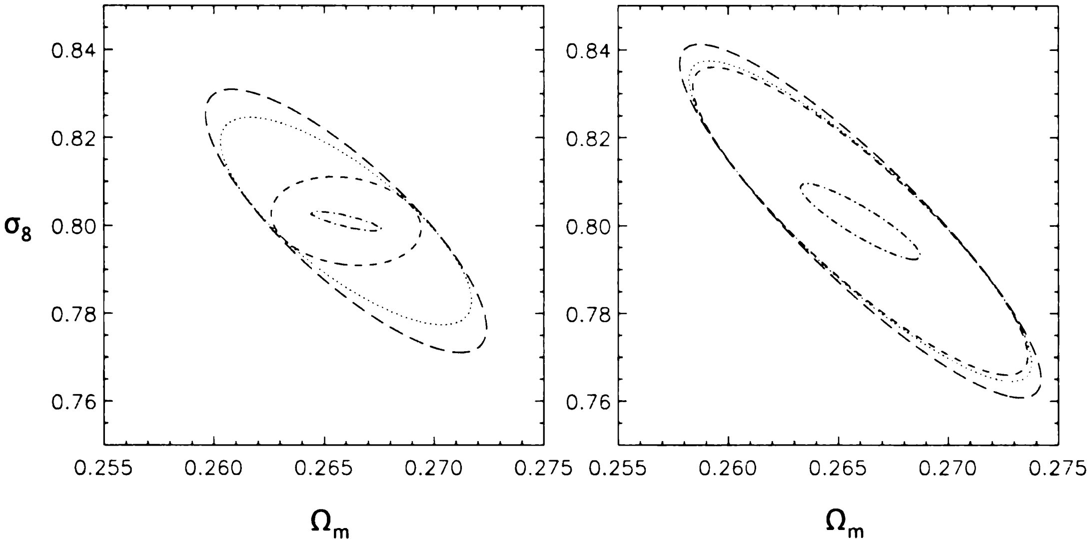

Figure 4.4 *Constraints for the $\Omega_m - \sigma_8$ plane using redshift and mass evolution of cluster number counts when γ is held constant (left panel) and when it is unfrozen (right panel). This shows a step-by-step degradation of constraints from OC (long-dashed line) to SC I (dotted line) to SC II (short-dashed line) and finally to the full self-calibrate case, SC III (dash-dotted line).*

This huge improvement especially for SC cases is seen for all parameters. The additional binning in luminosity space limits the degradation that we get after cluster structure parameters are freed. It, therefore, looks like that this binning in luminosity space is somehow constraining our lack of cluster structure knowledge.

Thus adding mass function shape information to cluster number redshift evolution provides much more information in constraining the cosmological as well as the cluster structure model parameters. Figure 4.5 shows the comparison of constraints from redshift-*only* evolution and how they are improved after *adding* the information from cluster mass function evolution to its redshift evolution, when γ is held constant and when it is freed.

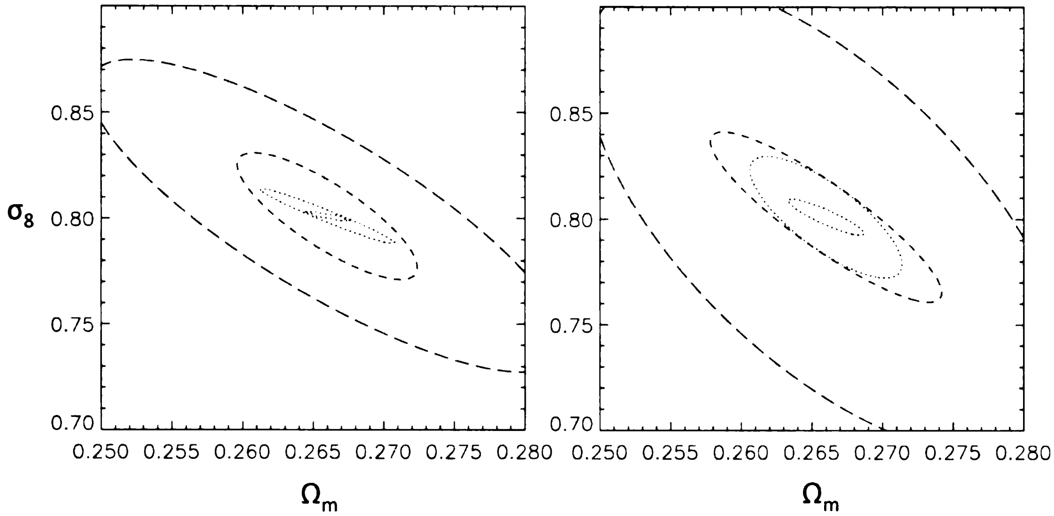

Figure 4.5 *Comparing the constraints from redshift-only (outer ellipses) and redshift and mass evolution (inner ellipses) of cluster number counts for OC (dashed lines) and SC III cases (dotted lines) when γ is constant (a), and when it is freed (b).*

4.1.3 Constraints From Cluster Power Spectrum

The cluster power spectrum is not very effective in constraining parameters other than Ω_m. In fact the constraints practically get very poor as soon as SC is allowed, on all parameters except on Ω_m. Figure 4.6 shows an illustrative example for OC case only. As was also discussed in Section (3.4.3), tight constraints on Ω_m come essentially from the shape of the cluster power spectrum, thereby reflecting the Transfer Function $T(k)$ behaviour which is very sensitive to the redshift of the epoch of matter-radiation equality. The second source of information for improvement in Ω_m is the bias factor, which is a strong function of mass of the galaxy cluster.

4.1.4 Improved Constraints By Combining Information Sources

Combining information from the cluster power spectrum and from the redshift and mass evolution of cluster number counts provides us with improved constraints on all parameters. Figure 4.7 shows that this improvement is achieved for all cases, from

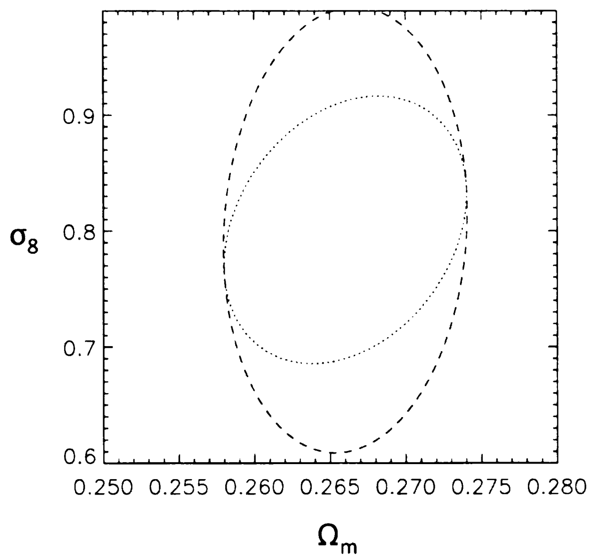

Figure 4.6 *Constraints from the cluster power spectrum only, for OC case when γ is constant (dotted line) and when it is freed (dashed line).*

OC to SC III.

From this figure we see that the constraints on Ω_m, for SC III case, improve from $\Delta\Omega_m = 0.034$ (from redshift-*only*) to 0.006 (from redshift *and* mass evolution) and finally to 0.004 (from cluster power spectrum + redshift and mass evolution of cluster counts). The constraints improve for all the cases when γ is held constant as well as when it is freed. This shows how combining the three sources of information helps in improving constraints.

4.1.5 Conclusion

In this Section we learned that for a given survey, and for a given information source, constraints degrade as we go from OC to SC III. For the $\Omega_m - \sigma_8$ plane the $M - L$ structure parameters L_0 and α are responsible for maximum uncertainty. In general, unfreezing γ also degrades confidence levels for a given case. Further, redshift-*only* evolution of cluster number counts is a very poor source of information in obtaining constraints. This weakness can be overcome by combining information from the

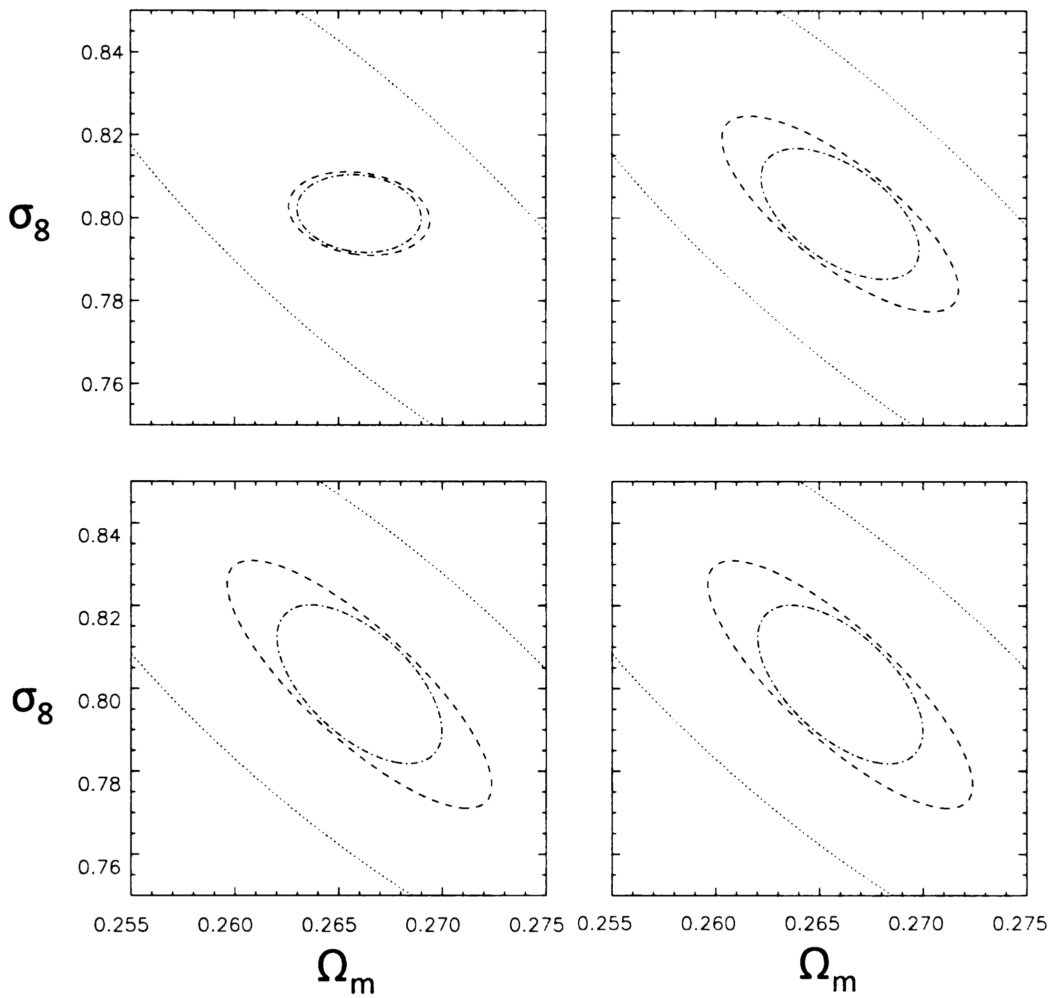

Figure 4.7 *Improvement in constraints, for OC (top-left), SC I (top-right), SC II (bottom-left) and SC III (bottom-right) cases, when the information from the redshift and mass evolution (dashed-lines) is combined with that from the cluster power spectrum (dash-dotted lines), γ is held constant here.*

cluster mass function evolution with its redshift evolution information. The cluster power spectrum is a very poor source of information on all parameters except on Ω_m, however, when used in combination with the other two information sources it helps in improving the information gained about different parameters.

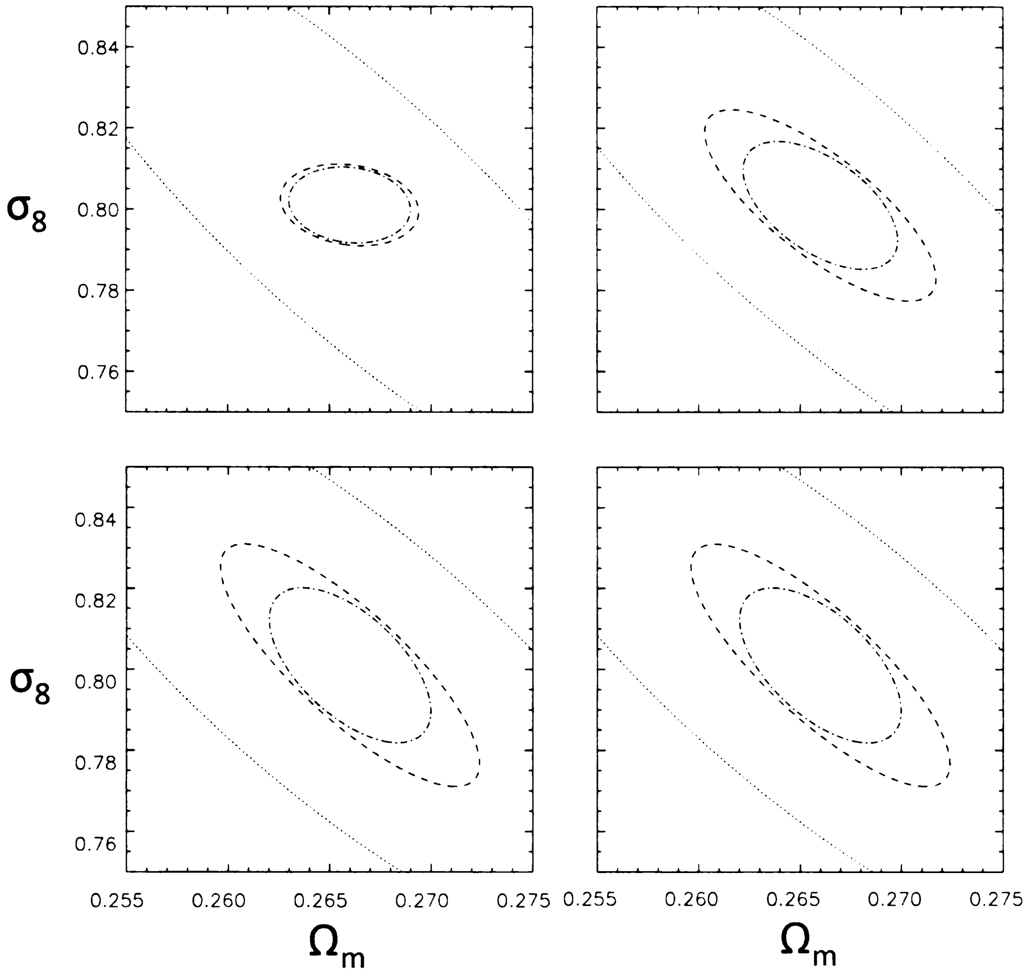

Figure 4.7 *Improvement in constraints, for OC (top-left), SC I (top-right), SC II (bottom-left) and SC III (bottom-right) cases, when the information from the red-shift and mass evolution (dashed-lines) is combined with that from the cluster power spectrum (dash-dotted lines), γ is held constant here.*

cluster mass function evolution with its redshift evolution information. The cluster power spectrum is a very poor source of information on all parameters except on Ω_m, however, when used in combination with the other two information sources it helps in improving the information gained about different parameters.

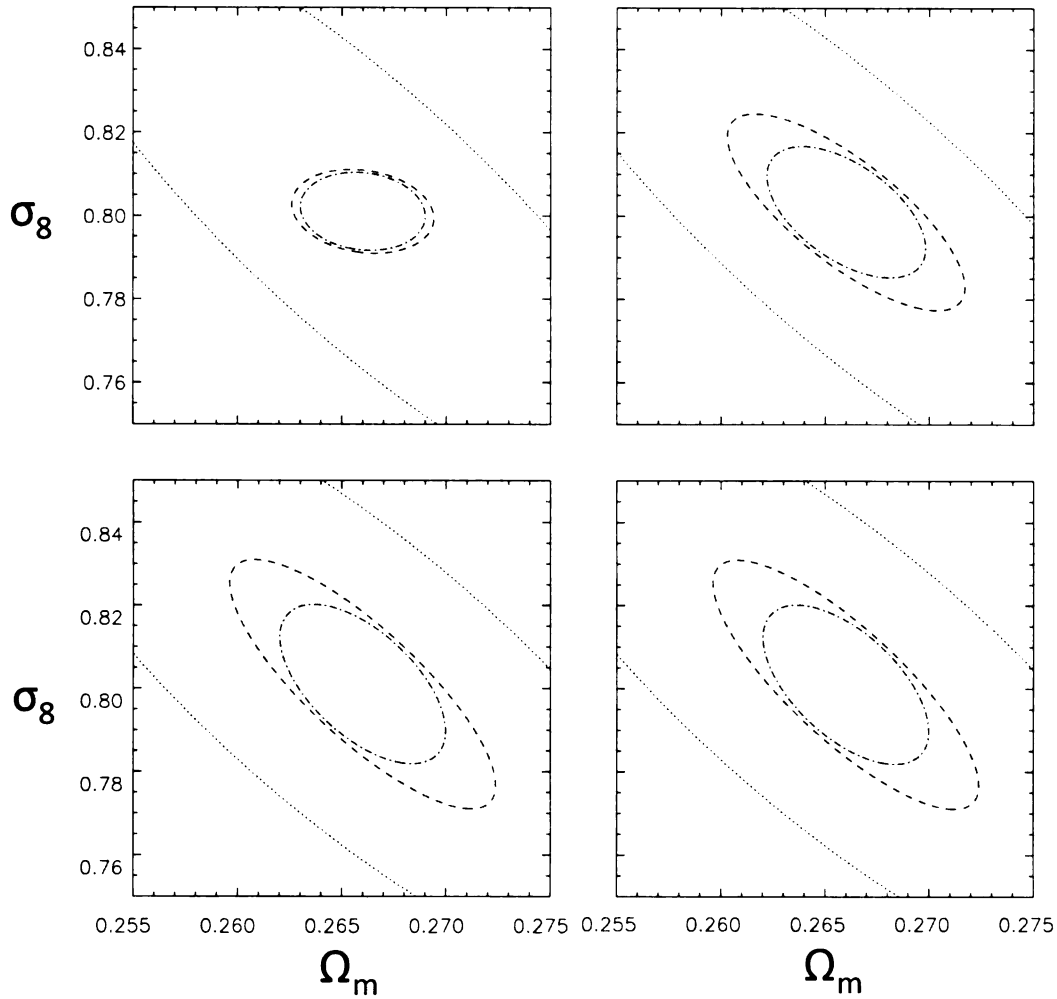

Figure 4.7 *Improvement in constraints, for OC (top-left), SC I (top-right), SC II (bottom-left) and SC III (bottom-right) cases, when the information from the redshift and mass evolution (dashed-lines) is combined with that from the cluster power spectrum (dash-dotted lines), γ is held constant here.*

cluster mass function evolution with its redshift evolution information. The cluster power spectrum is a very poor source of information on all parameters except on Ω_m, however, when used in combination with the other two information sources it helps in improving the information gained about different parameters.

4.2 THE GRAVITATIONAL GROWTH INDEX: HOW WELL IS IT CONSTRAINED?

The most widely accepted theory to explain the cosmic acceleration is General Relativity, which needs a Dark Energy component. GR directed growth of structure is different from other gravity models that have been theorised to explain cosmic acceleration. The parametric form of the growth function $D(z)$, as is given in Eqn. (2.1) models the GR directed growth for a γ value of ~ 0.55 [Linder, 2005]. The other leading candidate to explain cosmic acceleration is Modified Gravity. The DGP Model is one such example and has a γ value of ~ 0.68. The two models GR and DGP predict different growth history as was seen in Section (2.1) and in Section (3.4). Observing structure growth in the Universe will therefore differentiate between the two models if the cluster survey will have enough power.

We have seen the effect of unfreezing the γ on the Ω_m-σ_8 plane in the last Section. Accepting a lack of complete knowledge about γ essentially degrades the constraints. In this Section we will see how well the GR model can be constrained, given the power of next generation surveys. In the next Section we will return to the question of distinguishing growth from the two gravity models to see if one or the other of the these models can be ruled out using information on galaxy clusters that these surveys will gather, in light of insufficient knowledge of cluster structure including the $M - L$ scaling relation, its evolution, the scatter present as well as scatter evolution.

4.2.1 CONSTRAINTS ON GR GROWTH

Figure 4.8 shows 2σ constraints on the $\gamma - \Omega_m$ plane that can be obtained from the eROSITA wide-field survey, as we proceed from the OC case to the SC III case, using information from the redshift-mass evolution and combined information from the cluster mass function and the cluster power spectrum. Constraints degrade from OC to SC cases, as is expected. For the full SC case and using combined information from

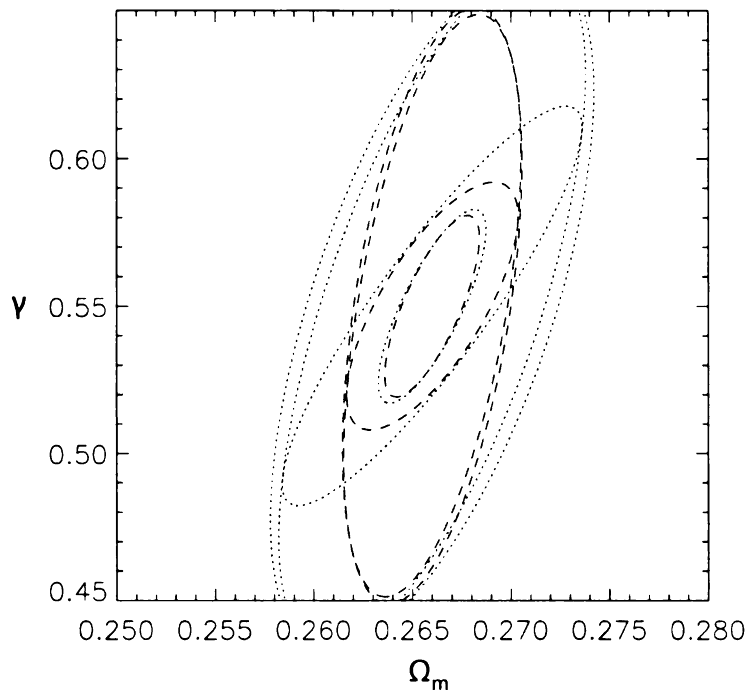

Figure 4.8 *Constraints on $\gamma - \Omega_m$ plane in the GR Model for cluster mass function evolution (dotted lines) and cluster mass function evolution + cluster power spectrum (dashed lines) as we go from OC (innermost ellipses) to SC III (outermost ellipses).*

the cluster mass function and the cluster power spectrum, GR growth is constrained well within 0.55 ± 0.10.

Figure 4.9 shows the performance of different surveys in constraining the GR growth. The 2σ contours plotted here are for the SC III case and use combined constraints from the three information sources. WFXT is expected to constrain the GR Model twice as strongly than eROSITA, with its wide-field survey constraining γ to well within 0.55 ± 0.05 on a 95% confidence level.

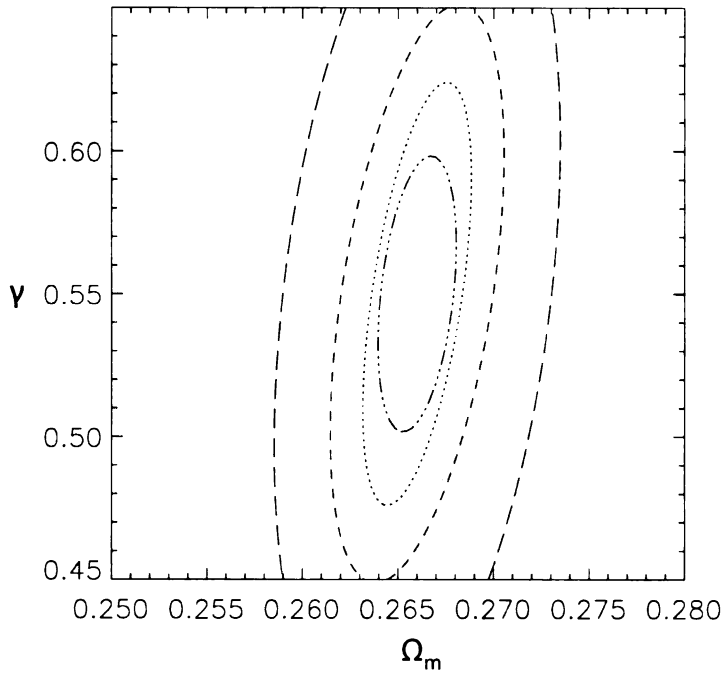

Figure 4.9 *Combined constraints from cluster mass function evolution and cluster power spectrum on $\gamma - \Omega_m$ plane for the full SC case from different surveys, WFXT: wide-field (dash-dotted line) and medium survey (dotted line); eROSITA: wide-field (short-dashed line) and all-sky survey (long-dashed line).*

4.3 Is It GR Or Is It Not GR? Will The Next Generation Surveys Be Able To Tell?

In this Section we compare the two gravity models to see if either of them can be ruled out for the full SC case at the 2σ level using the galaxy cluster survey power of eROSITA and of WFXT. Ruling out one or the other of the gravity models for full *Self-Calibration* case is important because the presence of scatter and/or evolution of scaling relations can masquerade as a different gravity model if the statistical power of the survey is not enough. We then need to find ways to add more information through the use of priors for the purpose of distinguishing the growth history of the Universe. For this purpose we conducted an experiment where Fisher Matrices were constructed for two model Universes based on the two gravity models GR and DGP.

4.3.1 eROSITA Performance

Figure 4.10 compares the 2σ error ellipses for the two gravity models, GR (lower ellipses) and DGP (upper ellipses) at each step of information loss.

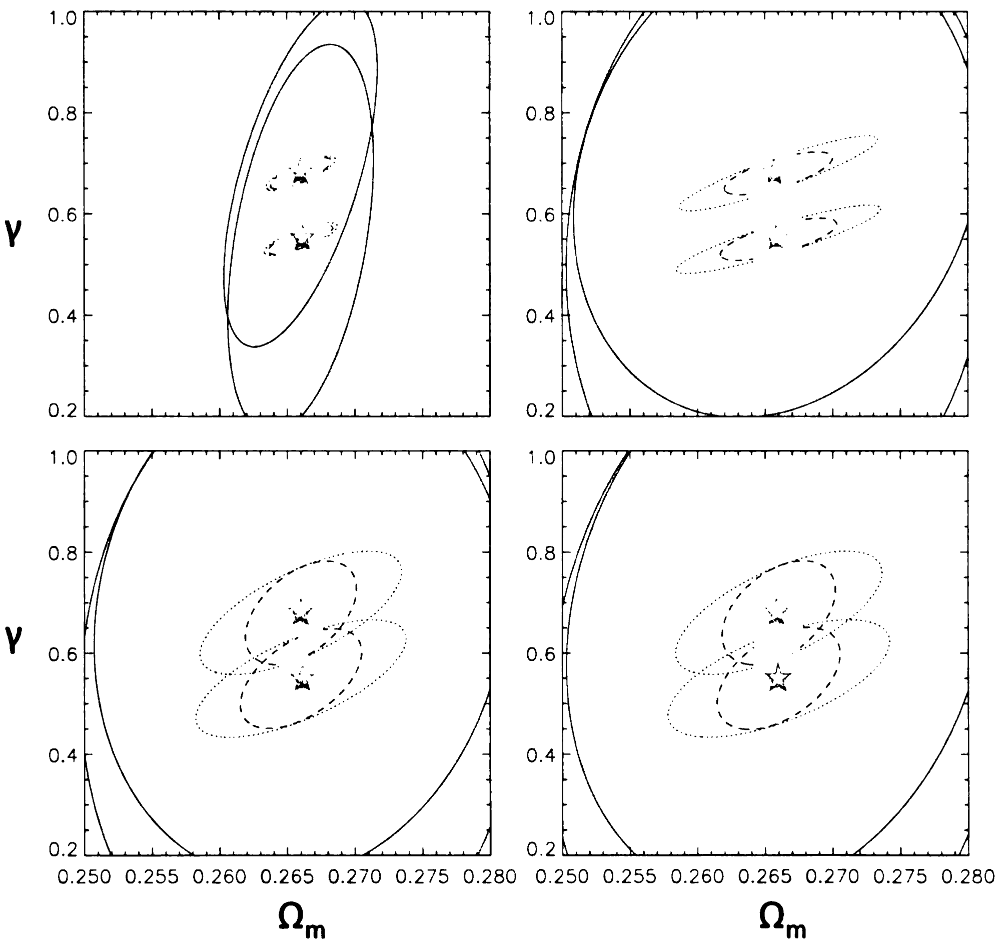

Figure 4.10 *Degradation in the ability to distinguish the two gravity models from the OC case (top-left) to the SC I (top-right) to the SC II (bottom-left) and to the full self-calibrate case SC III (bottom-right) for eROSITA wide-field survey. The contours shown are for redshift-only evolution (solid lines), redshift and mass evolution (dotted lines) of cluster number counts and for the combined constraints with cluster power spectrum (dashed lines).*

If redshift-*only* evolution of cluster number counts is our only source of information, the two gravity models will not be distinguished, even after we assume perfect knowledge of cluster structure. Combining redshift-*only* evolution with other sources of information allows us to distinguish the two models at the 2σ level for the OC case. Constraints degrade when the structure parameters, L_0 and α are allowed to be free, however the information from cluster mass function evolution will still be able to differentiate growth from the two models. When the structure evolution parameter β is unfrozen, the combined information from cluster mass function evolution and cluster power spectrum will not be able to completely distinguish growth from the two models.

Adding Priors: Essentially for SC II and SC III cases, we see that the eROSITA Wide-field Survey is not able to distinguish between the growth from the GR and the DGP models. In order to improve constraints further, we need to add *priors*. To see what more information is needed to distinguish the models when the survey power is not enough, we decided to study this further by adding artificial priors on different parameters in order to see what parameter is the reason behind this degeneracy.

Any knowledge of scatter or its evolution is of little help in constraining growth further. Only a marginal improvement is seen in constraints after adding even strong priors either on scatter or on its evolution. Similarly adding priors on $M - L$ scaling relations cannot constrain gravity further for the purpose of distinguishing the two models. However, when we add strong priors on the evolution of cluster scaling relations β, it is very effective in improving the constraints and for eROSITA wide-field survey it does distinguish growth when strong priors $\sim 5\%$ are added on β.

eROSITA Wide-Field Survey

Figure 4.11 shows constraints on the $\gamma - \Omega_m$ plane for the no prior case and how they it improve after we add $\sim 10\%$, 5% and 3% priors on β. From this we see that for eROSITA wide-field survey to be able to separate GR physics from DGP physics, we need to add priors on β better than $\sim 5\%$ when full *self-calibration* is allowed.

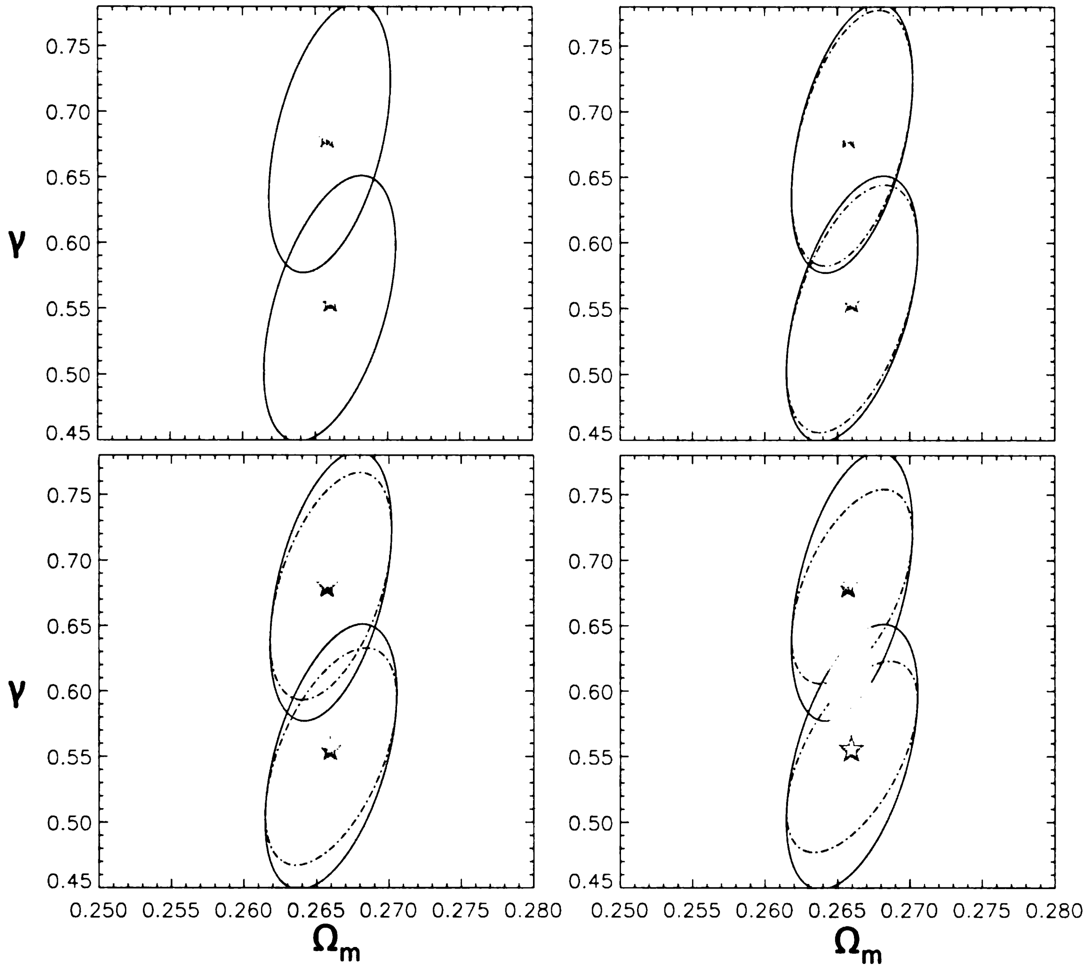

Figure 4.11 *Indistinguishability of the growth models and the improvement in constraints on growth as a result of adding priors on β, $\sim$ 10% (top-right), $\sim$ 5% (bottom-left) and $\sim$ 3% (bottom-right). The top-left panel shows no prior case. The 2σ contours shown are for the combined constraints from the cluster mass function with the cluster power spectrum for SC III case. The survey definition used is that of eROSITA Wide-field Survey. The dash-dotted lines show the improved constraints when priors are added. The stars show the location for the respective fiducial models. As we see from figure, the two models are completely distinguishable on 2σ level after adding strong priors on β.*

eROSITA All-Sky Survey

The picture is worse for the case when the survey power of eROSITA All-sky survey definition is used. Figure 4.12 shows the result of constraining growth using its survey parameters.

Thus, we see from this figure that the growth is not completely distinguished, on

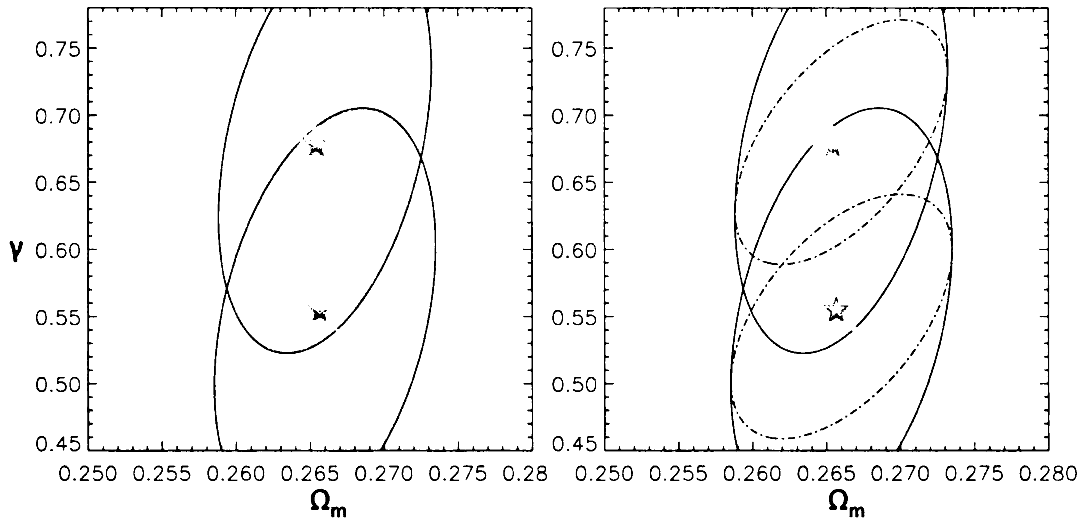

Figure 4.12 *Indistinguishability of the growth models and the improvement in constraints on growth as a result of adding strong ($\sim 3\%$) priors on β (right panel) The left panel shows no prior case. The contours shown are for redshift and mass evolution (dotted lines) of cluster number counts, for the combined constraints from cluster mass function with the cluster power spectrum for the SC III case. The survey definition used is eROSITA All-sky survey.The dash-dotted lines show the improved constraints when priors are added. The stars show the location for the respective fiducial models. As we see from figure, the two models are not completely distinguishable on 2σ level even after adding strong priors on β.*

a 2σ level, even after adding priors as strong as $\sim 3\%$. Again, information in form of priors from other cluster structure parameters is of little help in constraining growth.

4.3.2 WFXT Does The Job!

WFXT with its unprecedented flux-limits and large sky coverage, promises to be unparalleled in constraining growth history of the Universe. Figure 4.13 shows the effectiveness of the two WFXT surveys to distinguish the two gravity models on a 95% confidence level.

However, the survey power of WFXT medium survey will not be enough to distinguish growth, and strong priors on β will be needed to be able to completely rule out either of the two gravity models with a 99% confidence. Figure 4.14 shows 2σ and 3σ constraints on $\gamma - \Omega_m$ plane.

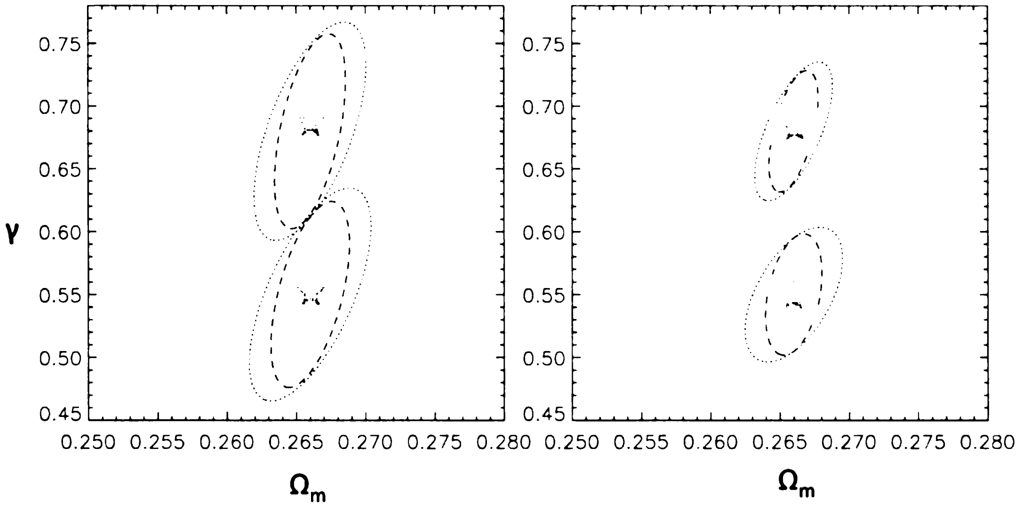

Figure 4.13 *2σ constraints on $\gamma - \Omega_m$ plane for the two gravity models from cluster mass function evolution (dotted lines) and the combined constraints with cluster power spectrum (dashed line) when full self-calibration is allowed. WFXT medium survey (left panel) and wide-field survey (right-panel) definitions are used. Both surveys are able to distinguish between the two models on a 2σ level. The stars show the location for the respective fiducial models.*

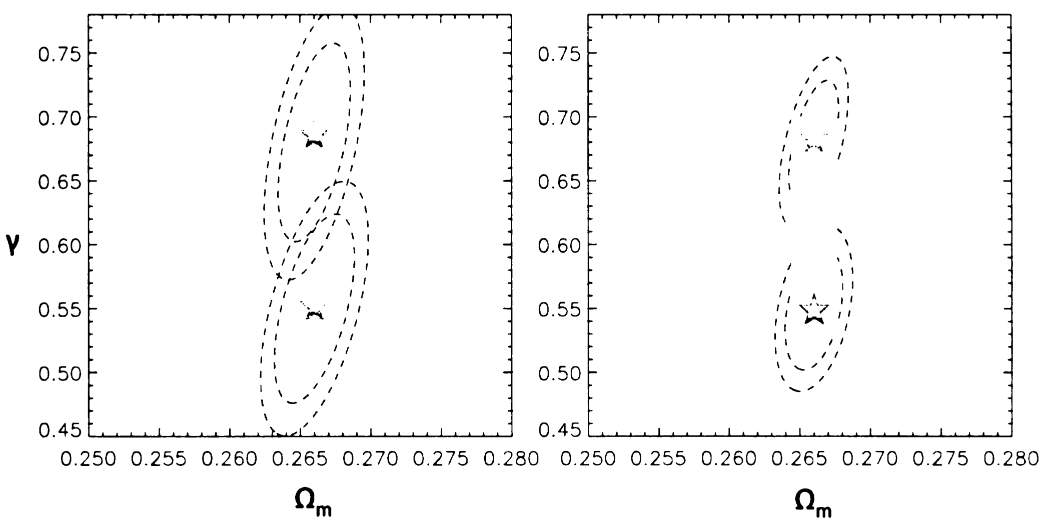

Figure 4.14 *2σ and 3σ constraints on growth from the WFXT medium (left-panel) and wide-field survey (right-panel) for full self-calibrate case, from combined information from cluster mass function evolution and cluster power spectrum. WFXT wide-field survey will be able to distinguish between GR and DGP model with 99% confidence. The stars show the location for the respective fiducial models.*

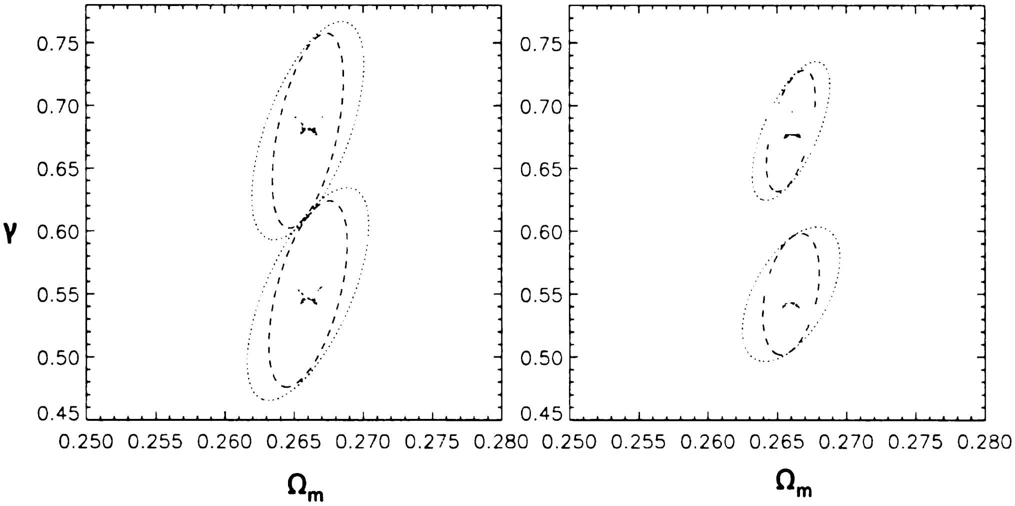

Figure 4.13 *2σ constraints on $\gamma - \Omega_m$ plane for the two gravity models from cluster mass function evolution (dotted lines) and the combined constraints with cluster power spectrum (dashed line) when full self-calibration is allowed. WFXT medium survey (left panel) and wide-field survey (right-panel) definitions are used. Both surveys are able to distinguish between the two models on a 2σ level. The stars show the location for the respective fiducial models.*

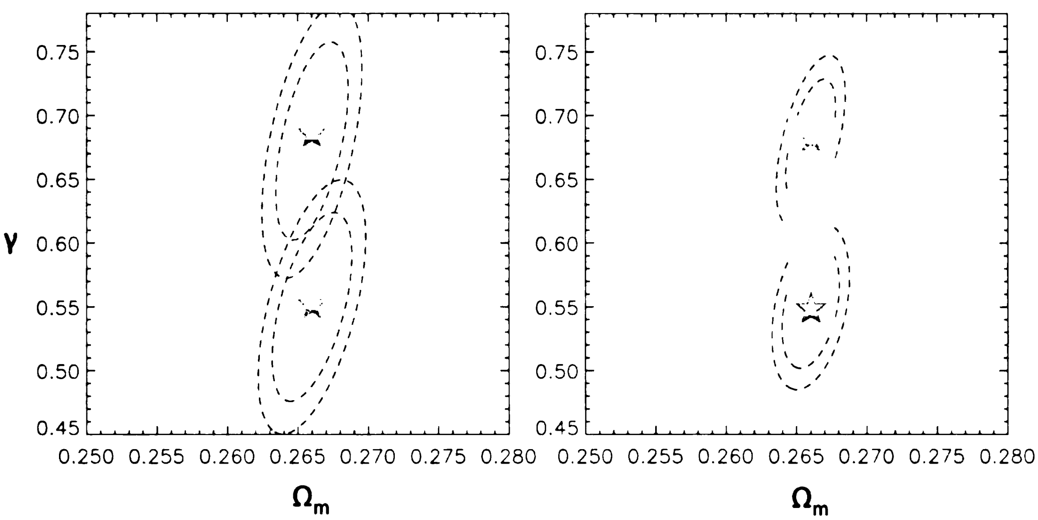

Figure 4.14 2σ *and* 3σ *constraints on growth from the WFXT medium (left-panel) and wide-field survey (right-panel) for full self-calibrate case, from combined information from cluster mass function evolution and cluster power spectrum. WFXT wide-field survey will be able to distinguish between GR and DGP model with* 99% *confidence. The stars show the location for the respective fiducial models.*

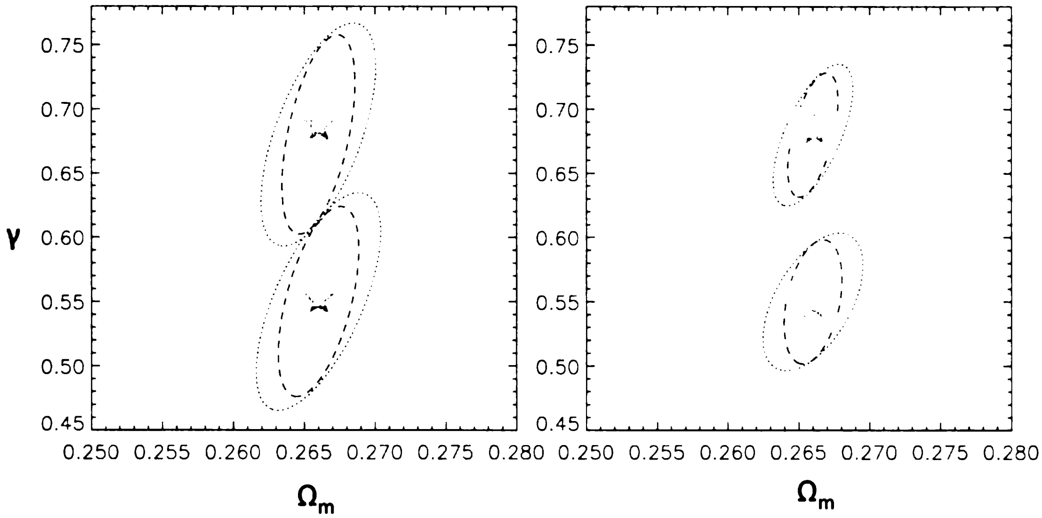

Figure 4.13 *2σ constraints on $\gamma - \Omega_m$ plane for the two gravity models from cluster mass function evolution (dotted lines) and the combined constraints with cluster power spectrum (dashed line) when full self-calibration is allowed. WFXT medium survey (left panel) and wide-field survey (right-panel) definitions are used. Both surveys are able to distinguish between the two models on a* 2σ *level. The stars show the location for the respective fiducial models.*

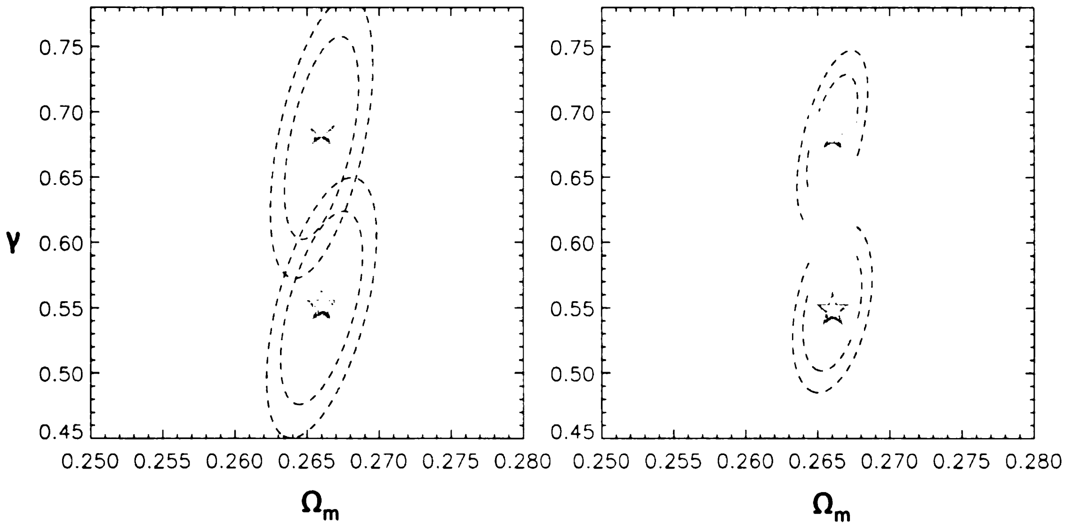

Figure 4.14 2σ *and* 3σ *constraints on growth from the WFXT medium (left-panel) and wide-field survey (right-panel) for full self-calibrate case, from combined information from cluster mass function evolution and cluster power spectrum. WFXT wide-field survey will be able to distinguish between GR and DGP model with* 99% *confidence. The stars show the location for the respective fiducial models.*

We see from Figure 4.14 that the WFXT wide-field survey will thus be carrying enough information in its galaxy cluster data to be able to tell us with 99% confidence whether it is GR or not.

Chapter 5: Summary And Conclusions

Acceleration of the Universe is one of the biggest mysteries which is haunting the current generation of cosmologists since the last decade. To explain it, the standard model needs hitherto unobserved *Dark Energy* or Einstein's *cosmological constant* Λ. While the current constraints are consistent with Λ, the uncertainties are still enormous. The other alternative is to go *beyond Einstein* and test the large-scale structure for deviations from GR, since expansion alone is not sufficient to differentiate between the different gravity models.

For this we studied the statistical power of next generation galaxy cluster surveys which will soon be scanning the skys. Their combination of lower flux-limits and larger sky area to be covered will push the discovery space far beyond the limits achieved by current surveys. The information from these galaxy cluster surveys in the form of the evolution of cluster number counts in redshift and mass and in the form of the cluster power spectrum derived from statistical correlations of galaxy clusters on the sky, can be used to constrain various cosmological parameters. In light of the present uncertainty about the galaxy cluster structure and its evolution, it is practical to let the survey solve for (or *self-calibrate*) these scaling relations as well as the scatter present therein.

From this study we found that the statistical power of the next generation surveys will arm us with better constraints on various cosmological parameters even after admitting a lack of complete knowledge about the cluster structure, when we combine the information from the evolution of cluster number counts' redshift and mass evolution together with the information from the cluster power spectrum. Based on this we studied the ability of different surveys to constrain the growth history of the Universe. It was found that eROSITA surveys will need strong priors ($\geq 5\%$) on cluster structure evolution parameter β to rule out, at the 95% confidence level, one or the other of the two gravity models GR and DGP which were studied here. However, WFXT surveys do hold the special promise of differentiating growth and telling us whether it is GR or not, with its wide-field survey having the ability to say so even with a 99% confidence level.

In brief, WFXT will do the job!

CHAPTER 6: INTRODUCTION TO QUASARS

Discovered in 1963 by Maarten Schmidt [Schimdt, 1963], Quasars form a part of the larger AGN family as its most luminous member. Their most visible characteristic is the enormous amount of luminosity generated, which can be as much as 10^4 times that of a typical galaxy. This has earned them the title of the light beacons of the early Universe. Quasars can be seen out to the farthest reaches of the Universe and hence they are a powerful source of information about early times in the evolution of the Universe. Also known as Quasi-stellar objects (QSOs), they appear as point-like objects in the sky.

However, it is the spectrum of a quasar which is its most distinguishing feature and contains a wealth of information. The spectrum is unique in the sense that it extends over the widest range of frequencies, right from the X-ray to far in the radio regime. In addition to the continuum, which is roughly constant over thirteen orders of magnitude in frequency, the most prominent part of a quasar spectrum in the optical and UV wavelength range is the plethora of emission lines superimposed on this continuum.

Quasars and in general active galactic nuclei (AGN) show a very strong cosmological evolution. It has been observed that these objects were much more numerous at a redshift $(z) \sim 2.5$ than they are in the recent Universe. Their luminosity is a strong function of redshift, which suggests that there is something special about the youthful galaxies that promotes the creation of AGN. Another interesting connection between quasars and the evolution of the Universe comes from the fact that the intervening gas clouds in the inter-galactic medium (IGM) absorb the photons coming from quasars, as a result, their spectrum is changed by galaxies and clusters of galaxies along the line of sight.

6.1 Salient Features

The salient features of quasars include:

Very small angular size: In the night sky, as seen through a telescope, they appear as star-like objects (hence the name QSO), and their structure is usually unresolved. This is because they are very far away. Most often they outshine their host galaxies and hence only the nucleus is seen.

Huge redshifts: While the first object identified as a quasar had a redshift of 0.158 [Schimdt, 1963], quasars at redshifts $z \geq 6$ are now known [Jiang et. al., 2009]. These are accepted to be cosmological redshifts, indicating that we see QSOs at great distances and hence at large lookback times. We can find the distance to a quasar by comparing the displacement of emission lines of known atoms and ions to measure its z in a given cosmological model.

Very High Luminosity: Given the moderately bright apparent magnitudes of these objects, the luminosities must be huge. They produce huge energy output in very small area, resulting in enormous luminosities.

Characteristic Spectrum: The spectrum of a quasar is its most distinguishing feature and is unlike that of a star or a galaxy. It has a broad-band continuum emission on which are superimposed the strong emission lines. Usually the spectrum is variable in time. Also the light coming out is often polarized.

6.2 The Quasar Spectrum

Figure A.1 (see Appendix A for figures) shows a characteristic quasar spectrum from Sloan Digital Sky Survey (SDSS) [Vanden Berk et. al., 2001].

6.2.1 The Continuum

The broad-band spectral energy distribution (SED) is one of the defining characteristics of quasars. Tk have been observed in every wavelength. As a result, their spectra cannot be described in terms of one single physical process. The broad-band SED of a quasar continuum can be roughly described by a power law, $F_{\nu} = C\nu^{-\alpha}$ where α is the power-law index, C is a constant, and F_{ν} is the flux per unit frequency interval. Several thermal and non-thermal processes have been invoked in an attempt to explain the continuum emission. The UV and optical region is dominated by the *big blue bump*, coming mainly from the thermal emission from an accretion disc surrounding a black hole. X-ray continuum gets a major contribution from inverse Compton scattering of photons by relativistic electrons. The IR spectrum is generated by the dust emission whereas the radio emission, *if present*, is coming from synchrotron emission in strong magnetic fields associated with the quasar.

6.2.2 The Emission Lines

The spectral lines in a quasar spectrum are generally in emission and are a very prominent feature in the optical, UV and X-ray with equivalent widths (EW) ~100Å. This is in contrast to the spectrum of stars and galaxies, which has very weak lines that are predominantly in absorption. Another interesting thing about these lines is their remarkable uniformity from one object to another. The spectrum of very many objects looks very similar. The formation of emission lines is governed by basic laws of atomic physics, which is well studied by the experiments on Earth and hence we can use them with confidence as the diagnostics of physical conditions in the environments where these lines are formed.

Broad And Narrow Emission lines

The main difference in the emission lines of different quasars comes from the fact that some have lines with broad wings extending out to many tens of thousands of km/s, and hence are called Broad Emission Lines (BEL), whereas others have very narrow widths, called Narrow Emission Lines (NEL), not reaching more than a few hundred km/s in width. Permitted and semi-forbidden lines are seen in both BELs and NELs. When there is a broad wing, there is usually a narrow core as well. However, forbidden lines are only seen in NELs indicating a lower gas density in the region where they are formed. These emission lines are useful for deducing information about the physical conditions existing in the gas surrounding the central Black Hole (BH).

Other than the redshifts these emission lines tell us about various other things such as:

Velocities: By studying the widths of emission lines, we can deduce how fast the gas is moving in that region, and hence using kinematics we can find the mass of the central black hole.

Physical size: Studying the variability of the emission lines with respect to the continuum tells us about the physical size of the line emitting region.

6.2.3 Line Formation Process

Line formation is a result of atomic transitions. The various transitions occurring in a region include radiative and collisional transitions. The heating/cooling balance between these transitions determine what line is formed and what would be its strength. This balance between various heating and cooling processes is governed by various factors.

Energy of Photons incident on the Region: The incident photons from the central engine photoionise the broad emission line region (BELR) gas, which further results in line formation through radiative recombination and/or collisional de-excitation.

The Critical Densities: The electron densities in the region determine whether or not forbidden emission lines can be formed. There exists a competition between radiatively and collisionally de-excited lines in cooling the gas. The density at which collisional de-excitation starts to dominate is called the *critical density.* Usually the densities in the BELR are $\sim 10^9 - 10^{11}$ cm^{-1}. Since critical densities governing different lines vary, we also see some semi-forbidden lines like CIII] along with mostly permitted lines. In addition the *transition probabilities* of different elements and their *abundances* as well as the *electron temperature* in the region are among the deciding factors in the line-formation process.

6.2.4 Absorption Lines

In addition to the very prominent emission lines, some atomic absorption features are also present in some quasar spectra. These absorption features are formed because of the absorption and/or scattering of quasar photons by the gas present in the IGM along the line-of-sight. Usually the further away a quasar is the more absorption features it has. The Lyman α forest ubiquitously present in the quasar spectra is a well-known example.

6.2.5 Quasar Abundance Analysis Using Broad Emission Lines

The BELs come from the region just outside of the accretion disk. The gas in this region is moving very fast $\sim 10,000$ km/s . The quasar spectrum is dominated by these lines in the rest-frame optical and UV regions. Because of the ease of their detection and measurement in many objects they form a very good source for measuring abundances in that region. However many of these lines suffer from the disadvantage of severe blending with other nearby emission features. A careful deblending procedure therefore needs to be followed in deducing abundances from them.

The line-intensity ratios of different emission lines can be used to determine the relative abundances of the elements that enriched that region. However, there exists a plethora of lines even in the UV-optical part, so deciding which lines and more importantly which line-intensity ratios to use while making any such analysis becomes important. Flux in the lines depends on the heating vs. cooling balance. Furthermore, many line-intensity ratios are strongly sensitive to other physical conditions like gas temperature and ionisation level as well as to metallicity. So just *any* ratio will not work. Usually Nitrogen (N) is a good indicator of the enrichment in the region and scales directly with metallicity hence different N lines like NV, NIV], NIII] form the primary source of information on abundances in the BELR.

Over the past decade a technique has been developed to measure the overall metallicity (Z) of these BELRs. $(Z/Z_{\odot}) \sim (O/H) - (O/H)_{\odot}$, where O and H indicate the abundances of these elements by number. The approach [Hamann and Ferland, 1993; Hamann and Ferland, 1999; Hamann et. al., 2002] is to directly measure the N/O and N/C line-intensity ratios and then use the strong correlation between these two ratios and Z that is observed in our own Galaxy [e.g., Pettini et. al., 2002] to determine Z. The physical origin of the observed correlation is the build up of N as a secondary product of hydrogen (H) fusion via the CNO cycle in higher mass stars. This approach of measuring BELR chemical abundances is needed because it is impossible to directly measure the O/H or C/H ratios due to the fact that the H emission lines are primarily recombination lines that record the ionisation and heating rate in the BELR gas while the lines of elements heavier than Helium (He), (including C, N, O) record the cooling rate; and the heating and cooling rates always adjust to be in balance. This technique, instead, compares the strengths of emission lines that are competing to carry the cooling load, including lines of C, N and O. When the abundance of N is higher relative to C and O, lines of N are able to carry a greater fraction of the cooling, at the expense of the collisionally excited lines of the other elements. This makes the N/O and N/C line-intensity ratios sensitive to the relative abundances of these elements.

When connecting the line-intensity ratios to Z we also need a *model* which relates these two. Since most of the N is from secondary enrichment in the CNO cycle in massive stars, it is safe to assume that most of the stars that enriched the region were massive ones. The underlying model considered here is the Locally Optimally-emitting Cloud (LOC) Model of the BELR in a quasar [Baldwin and Ferland, 1995]. The LOC Model considers a stratified BELR with wide range of electron densities and wide range in incident photon flux. Furthermore, it says that each line forms prefentially wherever its emission is most favoured by the atomic physics and the observed spectrum is the sum over many diverse BELR components.

6.3 The Elemental Abundances In Quasars

The presence of BELs in the spectrum indicates the presence and abundance of heavy elements near the central engine of the quasar. This gives a unique measure of the star formation and chemical evolution in young galactic nuclei, since the gas emitting these elemental lines must have undergone some amount of chemical enrichment *via* the various processes, mentioned below. The abundance measurements in high z quasars put strong constraints on the properties of star formation in the very early Universe. One important goal of quasar abundance studies is to develop a better picture of star formation and galaxy evolution at early times. Quasar abundances studies also help us to better understand the local physics and environment of quasars themselves.

6.3.1 Sites Of Chemical Enrichment In A Galaxy

The stars in a galaxy are the primary source of metal enrichment in a galaxy. When they die, they release the metals formed/locked up in them into the Inter-Stellar Medium (ISM) [Hamann and Ferland, 1993],

Envelopes of intermediate mass stars ($1M_{\odot} - 7M_{\odot}$): The envelopes of these stars are important sources of He, N and C. There is no further burning after C is formed in their cores because of low mass. These stars end their lives as He or CO white dwarfs.

Type IA SNe: Type IA SNe are assumed to be main source of Iron (Fe) present in a galaxy.

Exploding He cores of massive stars as Type II and Type Ib SNe: These are important contributors of the major metals found in galaxies.

Envelopes above He cores of massive stars ($M \geq 7M_{\odot}$): These contribute to the enhancement of secondary CNO cycle elements in the ISM of a galaxy.

Low mass stars: These stars do not contribute much because they live too long and hence don't release their locked up metals in the ISM soon enough.

6.4 Quasar Abundances And The Evolution Of Galaxies

The main question we explore in this project in studying the elemental abundances in quasars is to search for the relationship of the QSO phase to the overall evolution of massive galaxies. It is well evident from the relation between $M_{SMBH} - M_{gal}$ that there exists a coupled evolution between spheroids and the Super Massive Black Holes (SMBHs) [Tremaine et. al., 2002]. The abundance studies help us in exploring this evolutionary relationship by telling us how much star formation occurs in spheroids before the quasars are lit. However there exist at least two diverging schools of thought on the nature of this evolution.

6.4.1 Mergers Vs. In-Situ Star Formation

Galaxy Mergers

Proposed first by Toomre (1977) and later expanded upon by Soltan (1982), this line of thought believes that massive spheroids are formed by major gas-rich galaxy mergers. The quasar phase is triggered by the merger between two spirals of roughly the same mass. The quasar is essentially the final stage of this merger process at which the spheroid is largely formed and has begun to relax. The observed relationship between spheroids and BHs residing in them indicates strong correlation between them. There are no bulges without Black Holes, and there are no bulge-less systems with Black Holes. This implies the same origin (common physical trigger) for SMBH and spheroids. The merger-driven model accurately predicts the observed excess (clustering) of quasars as a function of L and z, i.e., the observed sharp rise and fall of quasar luminosity density over cosmic time [see e.g., Hopkins et. al., 2007].

In-Situ Star Formation

The major blow against the merger theory as being the quasar phase trigger comes from surveys like DEEP2 and GOODS, neither of which shows any evidence of a connection between mergers and quasars at $z \sim 1$. DEEP2 [Cooper and Newman, 2003] maps about 20,000 galaxies in the redshift range, $0.4 \leq z \leq 1.35$ and studies the relationship between the galaxy colour and environment. It concludes that the fraction of red galaxies depends strongly on local environment out to a z of 1. Red galaxies favour overdense regions at low z relative to their counterparts at high $z(\geq 1.3)$. This suggests that the build-up of red galaxies has occurred prefentially in overdense environments at $z \leq 1.5$. Therefore it seems that the correlations between morphology and colour-density are the result of *nurture* (environment-driven) rather than being imprinted by *nature* (e.g. mergers) during their epoch of formation.

6.4.2 What Does Quasar Metallicity Tell Us About Any Of This?

What information can we get about the role of quasars in the evolution of galaxies by studying their abundances? The metallicity of a quasar is representative of the population of stars which were formed in the galaxy sometime back before the cosmic time corresponding to the observed z. The catastrophic events resulting from explosions and/or mergers ripped apart the stars and pushed some of the expelled gas to the centre of the galaxy toward the BH which grew supermassive as a result. The BELs we see come mainly from the region which most likely has formed from the winds of an accretion disk [Peterson, 1988]. A knowledge of quasar metallicity therefore points to the stellar population which might have enriched this gas in the BELR. The typical mass of the gas in BELR is about $M_{BELR} \sim 10^3 - 10^4 M_\odot$ and the mass of a BH is, $M_{BH} \sim 10^9 M_\odot$. Simple scaling arguments based on normal galactic chemical enrichment and solar or higher BELR metallicities show that the minimum mass of the enriching stellar population is of the order of 10 times the BELR mass, or more than $10^4 \sim 10^5 M_\odot$ [Baldwin et. al., 2003]. This stellar population needed to enrich this gas should be already there or still rapidly forming, when luminous quasars become observable.

6.4.3 Previous Results And New Questions

Previous studies about the elemental abundances in quasars have found no significant trend in metallicity (Z) and redshift (z) relation. However a stronger trend for larger N line-intensity ratios and hence high Z is seen in more luminous quasars at every z [Hamann and Ferland 1999; Warner et. al., 2003; Nagao et. al., 2006]. Shemmer and Netzer (2002) find that NV/CIV is more strongly correlated with the normalised accretion rate, L/L_{EDD}, than with Luminosity (L) or the central black hole mass, M_{BH}, thereby implying that quasars with higher L/L_{EDD} have higher Z. However contrary to this, Warner et. al., (2003, 2004, 2007) do not find any significant relationship with L/L_{EDD} but instead with M_{BH} even if the L is constant. This suggests that more massive BHs reside in more massive spheroids which characteristically have higher Z. Also, the slope of $M_{BH} - Z$ roughly mimics the galactic mass-metallicity relation, in that Z is higher in more massive hosts, consistent with the normal mass-metallicity relation in galaxies.

The metallicity of a quasar, or more specifically that of the BELR gas is, $Z_{gas} \sim 1 - 5Z_{\odot}$, implying enrichment by at least a galactic bulge-like population. Also, most star formation must have happened before the start of the quasar epoch. The SMBH halts the star formation and thus leads to the observed $M_{BH} - M_{gal}$ relation. The evolutionary sequence proposed by many theoretical models which go with the merger argument, is: Major merger $\Rightarrow$ Ultra-luminous infrared galaxy (ULIRG)/starburst $\Rightarrow$ possible transition object with declining star formation or partially obscured AGN $\Rightarrow$ visible quasar.

QSOs tell us about the ISM metallicity in the centre of massive galaxies. Some of the questions we can ask are:

Does the metallicity distribution fit with the expected age distribution in galaxy evolution models? What is presently known about QSO metallicity distributions? Does BH mass or L/L_{EDD} correlate most directly with Z? There however remains a paucity of very high metallicity QSOs. Once we have more such objects we can hope to have an increased leverage in measuring correlations with metallicity.

Chapter 7: Sample Selection And Data Reduction

7.1 The Project

The direct goal of this current project is to make improved measurements of the BELR metallicity in QSOs at the high end of the metallicity distribution, and to then compare the distribution of metallicities and the dependence of metallicity on other physical parameters of the QSOs to the predictions of chemical enrichment models.

In most quasar spectra, the only N line strong enough to be measured is NV. The strength of this NV $\lambda1240$ line with respect to CIV $\lambda1549$ or He II $\lambda1640$ has consistently indicated above solar metallicities in the BELR of QSOs. Such high metallicities are also expected according to the chemical evolution models. However, it has long been known from reverberation measurements that these different quasar emission lines are formed in overlapping, but non-identical parts of the BELR [e.g., see Peterson, 1988]. This emphasizes the fact that a correction for the different ionisation levels of N (N^{+2}, N^{+3}, N^{+4}), He^{++} and C^{+3} is needed in order to properly determine the relative abundances from the observed line-intensity ratios. These ionisation corrections are usually made by assuming a model for the radial (relative to the ionising continuum source) and density distribution of the gas in the BELR, and then computing how the observed line-intensity ratios are predicted to change with changing metallicity.

The model normally used for this is the Locally Optimally-emitting Cloud (LOC) model [Baldwin et. al., 1995]. It assumes that the distributions in internal density and in the radial distribution of number of gas clouds, both have simple power-law dependences. For the abundance determinations, the usual power laws used to describe these distributions are $(number\ of\ clouds) \sim (internal\ gas\ density)^{-1}$ and $(number\ of\ clouds) \sim (radial\ position)^{-1}$, which satisfactorily reproduces the mean spectrum of all QSOs, but is not very likely to *exactly* describe the situation in any particular QSO. Indeed, the spectra of QSOs with unusually narrow emission lines often show lumpy, complex emission-line profiles; demonstrating a non-uniform distribution of clouds over internal gas density and radial position [Baldwin et. al., 1996].

Given these uncertainties in the ionisation corrections, it is important to try and use lines from other ionisation states of N, in addition to NV. Besides providing a check for errors due to overlooked ionisation/excitation effects, this will also check for errors in measuring the heavily blended NV line. The first object checked for such a case was $Q0353-383$, which had been found by Osmer (1980) to have NIII] $\lambda1750$ and NIV] $\lambda1450$ lines that are far stronger than in typical QSOs. Although they are still much weaker than the strongest BELR lines such as Lyα or CIV $\lambda1549$, the NIII] and NIV] lines in $Q0353-383$ are strong enough to be accurately measured, which is not usually the case. Baldwin et. al. (2003b) obtained new Optical/UV spectra of this luminous QSO, and showed that line-intensity ratios involving all three measurable ionisation states of N (N^{++}, N^{+3} and N^{+4}) all give the same result that $N/C \sim 15(N/C)_{\odot}$ and hence the metallicity $Z \sim 15Z_{\odot}$ in this particular object. This supported the idea that the high metallicities determined for other QSOs in which just the NV line can be measured are also generally correct.

In a follow-up paper [Dhanda et. al., 2007] we studied the validity of the abundance measurements in two additional QSOs which had unusually strong, and therefore accurately measurable, NIII] and NIV] lines. The objects were $SDSS\ J\ 125414.27+024117.5$ and $SDSS\ J\ 154651.75+525313.1$. In the first of these objects, the lines of all the different observed N ionisation states again turned out to imply similar values of Z, with $Z \sim 10Z_\odot$. However, in the second case the different line-intensity ratios indicated different metallicities. This implies that in this later object, the standard LOC model does not correctly describe the structure of the BELR. Thus, two out of three of the "N-Loud" QSOs studied to date give results that support the use of the NV line strength as an abundance indicator, but the third object provides a warning that this line is not 100% trustworthy.

These results also led us to conclude that many of the quasars with relatively strong NIII] and NIV] lines are representative of very highest metallicity galaxy cores in the highest redshift Universe. The high metallicity in these quasars raises interesting questions about the unusual chemical properties of such objects as well. Such quasars can therefore be used to test chemical enrichment models.

This current project is a study in using the N-line technique for measuring Z in a larger sample of QSOs with strong NIV] and NIII] emission lines, and to map out the general properties of these super-metal-rich QSOs in order to understand how they fit into the general picture of the early evolution of massive galaxies.

7.2 Sloan Digital Sky Survey

The observations for this project have been taken from the Sloan Digital Sky Survey (SDSS).

The Sloan Digital Sky Survey (SDSS)[www.sdss.org] is one of the most ambitious cosmography projects ever undertaken. The SDSS is systematically mapping a quarter of the entire sky producing a detailed image of it and determining the positions and absolute brightnesses of more than 100 million galaxies, giving us a three-dimensional picture of the Universe through a volume one hundred times larger than that explored to date. The SDSS is also recording the distances to 100,000 quasars, giving us the unprecedented knowledge of the distribution of matter to the edge of the visible Universe. The SDSS uses a dedicated 2.5-meter telescope at Apache Point, New Mexico, with a 3 degree field, and a mosaic CCD camera and two fiber fed double spectrographs to carry out the imaging and surveys respectively. A separate 20" photometric telescope is used for photometric calibration.

The SDSS is obtaining spectra of complete samples of galaxies and quasars. These spectroscopic targets are selected from the imaging data via various target selection criteria. Quasar target selection is based on the non-stellar colours of quasars and matching unresolved sources to the FIRST radio catalogue. The colour selected quasar candidates are those objects that lie more than 4σ from the stellar locus and have i-band PSF magnitudes, $15.0 \leq i \leq 19.1$. The SDSS spectra are taken with two fiber fed spectrographs, covering the wavelength range 3800-9200 Å over 4098 pixels. The fibers plug into plates that are the focal plane of the telescope. Each plate can hold 640 fibers with a fixed aperture of 3". The plates are positioned by a tilting algorithm and fibers are assigned to targets. The finite diameter of the fiber cladding prevents fibers on any given plate from being placed closer than 55" apart.The resolution varies between, $R = \delta\lambda/\lambda \sim 1850 - 2200$. The relative spectrophotometry is accurate to about 20%. Each spectrum is accompanied by an estimated error per pixel, based on photon statistics and the amplitude of sky residuals.

The spectroscopic data are reduced through the spectroscopic pipelines, spectro1d, spectro2d and specBS. Spectro2d reduces the two dimensional spectrograms produced by the spectrographs to flux and wavelength calibrated spectra, while specBS determines classifications and redshifts via a χ^2 fit to the spectrum in question with series of rest-frame star, galaxy and quasar templates.

7.3 The SDSS Quasar Catalogue IV

We use the fourth edition of the SDSS Quasar Catalogue as the base sample for our abundance studies. The catalogue contains a total of 77,429 objects and comes from the SDSS fifth data release (SDSS DR5) [Schneider et. al., 2007]. It consists of objects that have luminosities greater than $M_i \sim -22.0$ (in a cosmology with $H_0 = 70$ km sec^{-1}, $\Omega_M = 0.3$, $\Omega_\Lambda = 0.7$) and have at least one BEL with FWHM larger than 1000 km sec^{-1} or have interesting/complex absorption features, are fainter than $i \sim 15.0$ and have highly reliable redshifts. This catalogue covers an area of about 5740 deg^2. The quasar z's range from 0.08 to 5.41, with a median value of 1.48 and a 70% of all detected quasars have z's below 2.0. The data are presented in tabular form and were downloaded from the SDSS website. More than 90% of the objects in here were discovered by the SDSS.

7.3.1 Selection Effects In SDSS Quasar Sample

This Quasar Catalogue is not a statistically complete sample. There are two reasons for this. It includes objects from all categories of target selection in SDSS, not just those selected as quasar candidates. While the catalogue contains both the TARGET selection flags used to select spectroscopic targets, and the BEST selection flags obtained by applying the final target selection version (sometimes to better photometric data obtained later during the survey), use of the BEST data produces a different set of quasar candidates than the TARGET version that was used to define spectroscopic plates, even for those parts of the sky that were targeted using the final quasar target selection algorithm described in Richards et. al. (2002). Secondly, the survey targets the areas of high galactic latitudes only.

7.4 Sample Selection And Data Reduction

The 77,429 Quasars in the SDSS Quasar Catalogue IV formed the base sample for this project. Not all spectra are, however, useful for this study.

7.4.1 Main Sample

As the very first step in narrowing down the sample base, we apply a redshift restriction. In this study of abundance analysis we need to find flux-ratios of various ions present in the BELR of a quasar, such as NIII]/CIII] and NV/CIV. We therefore need the quasars for which all the emission lines of interest fall within the observed wavelength range. The CIII] line lies at 1909 Å rest wavelength and forms one extreme of the picture. NV lies at 1215 Å rest wavelength and forms the other extreme. In order to have both these lines of interest present in the spectrum, the quasar should have, $2.29 \leq z \leq 3.61$. Putting this *redshift restriction* into use reduces our sample base to 8122 objects. This is only about 20% of the total number of quasars in the base sample.

7.4.2 Initial Data Reduction Steps

Various IRAF[iraf.noao.edu] routines have been used for the initial data reduction steps. A random sample of 100 QSOs was checked for spectrum quality, using the IRAF task SPLOT.

Extinction Correction

The spectra were corrected for Galactic Extinction using the A_u values given in the SDSS Quasar Catalogue, which are based on the maps of Schlegel, Finkbeiner and Davis (1998). We used the IRAF task, DEREDDEN, for this purpose.

Redshift Correction

The next step is to correct the spectra to rest frame wavelengths. This was done by applying redshift correction, using z values given in the catalogue, using the IRAF routine, DOPCOR.

Smoothing The Spectra

The spectra as downloaded are still noisy and not of much use in the raw form. In order to process the data further, the IRAF smoothing routine contained in the SPLOT task was applied to all the spectra, with a seven pixel smoothing.

Continuum Subtraction

All 8122 spectra were continuum subtracted using a polynomial fitting routine with maximum power law of 3 and applying two rejection iterations of three sigma each, to allow rejection of spurious signal from atmospheric emission lines, residual cosmic rays etc. These 8122 reduced quasar spectra formed the intermediate sample base, to be used for further data reduction and analysis.

7.4.3 Data Reduction II

This Section explains the narrowing down of the intermediate sample base to 42 Quasars for precise abundance measurements.

Signal-To-Noise Ratio

First, all 8122 quasar spectra were examined by eye and $\sim$ 2000 of them which were too noisy (e.g., see Figure A.2(a)) for detailed abundance analysis were discarded. The S/N threshold for this rejection was roughly 5.

Missing Lines Of Interest

A Fortran routine was applied to check for any spectrum with no data in the regions of emission lines we needed for further processing (e.g., see Figure A.2(b)). This step then eliminated all spectra with missing lines of interest.

CIV Absorption

The CIV $\lambda1549$ emission line strength is important for our study as it is used in finding the line-intensity ratios. Many times this line is absorbed either by intervening gas clouds or quasar outflows. We therefore checked the database for spectra with heavily absorbed CIV lines, using a Fortran routine to check the fraction of absorbed CIV emission line flux and rejected spectra where CIV emission line flux is more than 50% absorbed (see, e.g., Figure A.2(c)).

Checking The Authenticity Of NIV] And NIII] Lines

The NIII] and NIV] lines are relatively weak in the QSO spectrum. Even when the lines are unusually strong, it is still quite difficult to be sure that they are real because they are blended with the broad wings of CIV (for NIV]) and Fe II (for NIII]) (see e.g., Figure A.2(d)). To check for the authenticity of these N-lines, we checked to see if they had roughly the same profile as the CIV line. This was done by automatically measuring fluxes in the NIV], CIV and NIII] lines through a wide velocity window (approximately 10,000 km s^{-1}) and then again through a narrower velocity window (approximately 7000 km s^{-1}). The NIV]/CIV and NIII]/CIV flux ratios were computed separately for each velocity window size, and then the ratio of ratios (narrow/broad) was computed. We discarded cases where this ratio of ratios fell outside the range: $0.7 - 1.3$. In the rejected spectra, the apparent N-lines were either just noise, or were dominated by blending with other features.

7.4.4 Automated Measurements Of Intermediate Sample

Next we performed automated measurements to calculate the full width at half maximum of the CIV emission line (FWHM(CIV)) and the continuum luminosity, L_λ at 1450 Å. using IRAF and FORTRAN routines. This was done for the full intermediate sample except for the spectra with heavy CIV absorption.

7.4.5 Final Sample With Measurable NIII] And NIV] Lines

The rejection steps described in Section 1.4.3 reduced our sample base to about 1000 spectra. We then ordered the surviving spectra by $NIV]/CIV$ ratio. Of these about 42 quasars had $NIV]/CIV$ ratios stronger than in $SDSSJ1254+0241$. An example of quasar spectra with strong N lines is shown in Figure A.2(e). Final data reduction and full abundance analysis was then performed on these 42 quasar spectra.

7.5 Final Data Reduction

7.5.1 Fe Subtraction

After the spectra have been corrected for redshift and continuum subtracted, the next step is to fit and subtract templates of FeII emission. A grid of such templates based on the Vestergaard and Wilkes (2001) study of I Zw 1, but broadened in velocity by different amounts, was kindly provided to us by M. Vestergaard. These particular templates do not include FeIII. For each QSO further analysed, we used the template with the broadening which most closely matched the measured widths of strong and relatively unblended emission lines (NIV] or C IV). To the extent possible, the fit was guided by the strength of the UV bump in the $\lambda\lambda 2240-2650$ Å rest wavelength region, where the FeII emission normally is strongest. However a few spectra which showed no visible Fe emission, were not Fe-subtracted. Also, none of these QSOs for which it was possible to fit FeII have very strong FeII bumps, so this correction was modest in all cases. The FeII $\lambda 2450$ strengths relative to the continuum are given in Table B.1 (all Tables for this project are given in Appendix B).

7.5.2 Profile Fitting And Flux Estimation

We then measured the emission-line strengths by finding and isolating individual lines which we could use as template velocity profiles for fitting to weak and/or blended lines. This is the same technique that was used by Baldwin et. al. (2003b) to measure the emission line strengths in $Q0353-383$ and recently by Dhanda et. al. (2007). The template profiles are based on different emission lines for different QSOs. Table B.2 lists which emission lines served as the template profile in each case. The measured fluxes of the emission lines are given in Table B.3, with fluxes in units of the total flux in the CIV doublet.

The Table B.3 also lists minimum and maximum fluxes for each line that are based on the best fit with alternate template profiles that did not fit as well as the best fitting template. In this or any other technique for measuring the strengths of broad and/or blended QSO emission lines, the errors usually are not due to photon counting or due to the statistics of the fit, but rather are completely dominated by the uncertainties in systematic effects such as the true shape of the line profile, whether or not additional weak lines should be included in the blend, and the level and shape of the underlying continuum. The maximum and minimum fluxes listed in Table B.3 are our best estimates of these effects.

This measurement technique has the advantage that it uses empirically determined line profiles, which in real life exhibit a wide variety of non-Gaussian shapes. It has the disadvantage that different lines in the same QSO can have quite different profiles, so the template profile often does not provide an exact fit. The initial fits were done by eye, and then the exact line strengths were finalized automatically using a χ^2-minimisation technique.

Apart from the usual lines used in the abundance analysis, mentioned before, OVI line at 1035 Å can also be used for this purpose. Out of a total of 42 quasar spectra in the final sample, 19 of these also have this OVI line present in their observed spectra. These spectra were, therefore, also fitted for the OVI line at 1035 Å. This provides us with two additional line-intensity ratios (NV/OVI and NV/(CIV+OVI)) to be used for the abundance measurements.

7.6 Abundance Analysis

We apply here the same procedure here estimating the abundances, that was used by Baldwin et. al. (2003b) for $Q0353-383$, and Dhanda et. al. (2007) for two of the QSOs from SDSS DR1 with strong N lines found by Bentz et. al. (2004).

7.6.1 Line-Intensity Ratio Measurement

Line-intensity ratios of various combinations are found simply by dividing the flux of the respective ions. Table B.4 lists the diagnostic line-intensity ratios for all 42 QSOs for which detailed measurements were made.

7.6.2 From Line-Intensity Ratio To Metallicity

The abundance measurement technique uses the observed line-intensity ratios of nitrogen lines to cooling lines of other elements, and compares them to the ratios predicted by the LOC model of the BELR for a segmented power law [Hamann et. al., 2002]. Here we have also adjusted the Hamann et. al. (2002) predictions to the revised solar C, O, and Fe abundances found by Allende Prieto et. al. (2001, 2002) and Holweger (2001). This modifications means that the same NV (relative to other strong lines) now occurs at about 30 percent lower Z than before, which was accounted for by subtracting 0.11 from $(Z/Z_{\odot})$ values given by Hamann et. al.

(2002). Figure A.3 shows the plot of these measured metallicities, separately for each QSO, onto the curves of line-intensity ratios versus metallicity predicted by the LOC Model, for each line-intensity ratio. Table B.5 lists the resulting best metallicity value for each line-intensity ratio Z for each QSO, along with the corresponding minimum and maximum values.

7.7 Mass Measurements

The mass of the SMBH of each quasar is estimated using the following equation [Warner et. al., 2004],

$$M_{SMBH} = 1.4 \times 10^6 M_\odot \left(\frac{FWHM(CIV)}{10^3\mathrm{km/s}}\right)^2 \left(\frac{\lambda L_\lambda(1450\text{Å})}{10^{44}\mathrm{ergs/s}}\right)^{0.7} \tag{7.1}$$

here, the FWHM is the full width at half maximum intensity of the CIV $\lambda1549$ line.

This equation estimates the SMBH masses by applying the virial theorem, $M_{SMBH} = rv^2/G$, to the line-emitting gas [Kaspi et. al., 2000],

$$M_{SMBH} = 1.5 \times 10^5 M_\odot \left(\frac{R_{BLR}}{1\mathrm{lt-day}}\right) \left(\frac{FWHM}{10^3\mathrm{km/sec}}\right)^2 \tag{7.2}$$

where R_{BLR} is the radial distance between the BELR and the central engine and FWHM applies to the broad emission line profile. The R_{BLR} can be estimated on the basis of observed relation between R_{BLR} for a particular line and the continuum luminosity. CIV has been used for the calculation of FWHM and Luminosity.

CHAPTER 8: THE RESULTS

8.1 METALLICITY OF QUASARS WITH STRONG NITROGEN LINES

We found the metallicity of 42 QSOs with strong N lines using six (eight for 19 QSOs) line-intensity ratios and the predictions from the LOC model. In our analysis, we also include the Quasar, $SDSS\ J\ 125414.27 + 024117.5$ which was found to have a metallicity of $Z \sim 10Z_{\odot}$, as mentioned in the last Chapter.

8.1.1 BEST METALLICITY ESTIMATE: MEAN VS. MAXIMUM LIKELIHOOD

The metallicities from different line-intensity ratios for all the QSOs are not exactly the same. In order to have the best metallicity estimate from all the measurements we calculated the mean metallicity Z_{mean}, from all the line-intensity ratios as well as the maximum likelihood estimate of metallicity, Z_{ML}.

MEAN METALLICITY (Z_{mean})

This is simply the mean of the best estimate of metallicity from the individual line-intensity ratios. To find the error range on mean metallicity estimates, we used the minimum and maximum estimates of individual line-intensity ratios. This, however, puts huge error bars on the Z_{mean} and we essentially loose the big picture. This might result from the fact that our minimum and maximum values of metallicities for individual line-intensity ratios are highly conservative estimates in nature. Using the standard deviation of the mean (SDOM) also gives a fair representation of the error on Z_{mean} values, so finally we decided to use the SDOM as our error estimate in Z_{mean}.

Maximum Likelihood Estimate Of Z (Z_{ML})

We also used the maximum likelihood method to estimate the best Z using all the line-intensity ratios. To estimate the error in metallicity from this method we used the lowest and the highest metallicity values from the individual line-intensity ratios.

Comparing The Two Methods

The metallicity estimates from these two methods are compared in Figure A.4. These two estimates point towards similar metallicities in QSOs. We finally decided to use the mean estimates (Z_{mean}) for our further analysis because of the simplicity of the method.

8.1.2 Metallicity From Individual Line-Intensity Ratios

To see how well the metallicity from individual line-intensity ratios (Z_{ind}) compares with the Z_{mean} we plotted the Z_{ind} as a function of Z_{mean}. Figure A.5 illustrates the comparison graphically. As seen from it, the Z_{ind} for all line intensity ratios matches quite well except those from NIV]/CIV and NV/He II. $Z_{ind}(NIV]/CIV)$ for most quasars lies well below the Z_{mean} line. This means that this line consistently indicates lower metallicity when compared to Z from other line-intensity ratios. Likewise, $Z_{ind}(NV/HeII)$ indicates consistently higher Z when compared to Z from the other line-intensity ratios.

8.1.3 Best Metallicity Estimate (Z_{best})

Since the metallicity from these two line-intensity ratios (NIV]/CIV and NV/He II) is on average very different from that indicated by other line-intensity ratios we decided not to use them in our best metallicity estimate. The best metallicity estimate (Z_{best}) is now simply the mean metallicity of all line-intensity ratios sans the two deviant ones. Figure A.6 compares the mean metallicity values for all QSOs before and after we neglect the two line-intensity ratios. We see that that on the average it does not change the results drastically. However, after removing the two deviant line-intensity ratios, the new best metallicity estimate, Z_{best}, agrees quite well with the metallicities from individual line intensity ratios which have been used to arrive at the mean value. The SDOM is used to give error in Z_{best}. Table B.6 lists the best metallicity estimates, Z_{best}, and the corresponding error values. Figure A.7 plots the distribution of Z_{best} among the N-loud sample, in form of a histogram.

Important Points About The Measured Metallicity Trend

The metallicity values as determined from the individual line-intensity ratios agrees well with one another except for $Z_{ind}(NIV]/CIV)$ and $Z_{ind}(NV/HeII)$, for most of the QSOs in our N-Loud sample. Even though there were some cases for which these metallicities from two these line-intensity ratios matched quite well with others, e.g. $SDSSJ1430+4811$; based on the statistics we decided to neglect these two lines to compute our best metallicity estimate. The main points we gathered from our abundance measurements in N-loud QSO sample are:

1. The line-intensity ratios, except NV]/CIV and NV/He II, give consistent Z estimates and can be used as valid metallicity indicators. Table B.7 gives the slopes and intercepts from all the relation between $Z'_{ind}s$ for different line-intensity ratios and Z_{mean} for quantitative comparison.

2. The mean of metallicity from all these line-intensity ratios sans the two described

above, is used as the best metallicity estimate (Z_{best}).

3. There are lone cases like $SDSSJ1159 + 6638$ where none of the line-intensity ratios agree with one another in metallicity. There were a total of three such QSOs, which is about 7% of total QSOs in the sample. This might be due to some complex BELR structure or excitation processes peculiar to that Quasar which are not found in QSOs in general.

4. On the whole the NIV]/CIV line-intensity ratio shows consistently *lower* metallicities. Here, the metallicities have been derived using the LOC model, which assumes a very simple distribution of gas clouds. The fact that the Z from this line-intensity ratio is, in general, not in agreement with Z from other line-intensity ratios suggests that either the simple distribution of clouds is not a sufficiently accurate description of the structure of the BELR, or that the Z from these line-intensity ratios are not being correctly predicted by the photoionisation code $CLOUDY$ [Ferland, 1996].

5. Similarly, the NV/He II line-intensity ratio, which shows on the average *higher* metallicities, suggests that the gas distribution might not be accurately described by the LOC model. Also, there might be errors due to the fact that the NV line is heavily blended with Lyα emission line, however that might not be the reason because the NV/CIV line-intensity ratio gives reasonable Z estimates.

6. Finally, the Quasars with strong N lines indeed have high Nitrogen abundance and are super-solar in metallicity, with Z reaching up to a maximum of $Z \sim 22Z_{\odot}$ in our N-loud sample. Figure A.7 also shows the distribution of measured Z_{best} in the N-loud sample in log space.

8.1.4 Distribution Of Other Physical Properties

The redshift distribution of the two sample sets is shown in Figure A.8. Figure A.9 shows the distribution of $FWHM(CIV)$ for the intermediate sample as well as for the final sample, measurements of which are described in Section 2.2.4. The measurement results for the continuum luminosity at $\lambda \sim 1450$ Å, $L_\lambda(1450)$, are shown in Figure A.10, which shows the distribution of L_λ for the intermediate sample as well as the final sample of N-Loud Quasars. The CIV Equivalent Width $EW(CIV)$ was measured for the N-Loud sample and the Figure A.11 shows its distribution among the N-loud QSOs sample only. The Mass of the supermassive blackhole (M_{SMBH}) was estimated using the virial theorem as described in the previous Chapter. The distribution of M_{SMBH} is illustrated in Figure A.12 for the intermediate as well as for the full sample. Figure A.13 gives the distribution of M_{SMBH} as a function of redshift (z) for both sample sets. The M_{SMBH} is of the order of $10^7 M_\odot - 10^{14} M_\odot$. No evolution is seen in mass of the supermassive black hole with redshift.

8.1.5 Relations Involving The Supermassive Black Hole Mass

We wish to see if there exist any interesting correlations among various measured physical properties of Quasars in general and the N-Loud Quasars in particular. Also, we want to see how do the N-Loud Quasars stand in relation to the overall QSO population in SDSS DR5. We, therefore, compare various measured properties of the intermediate sample and the N-Loud sample.

From the data of M_{SMBH} distribution in the two sample sets, we conclude that the N-Loud sample has on the average lower masses M_{SMBH}, than the general sample of Quasars. We verified this using the *Student's t test*. We found $t \sim 5.3$, corresponding to a probability, P value ≤ 0.0001 that the two samples are drawn from the same distribution. See also Figure A.14 which shows the comparison graphically.

Comparing Mass And Metallicity

We compare M_{SMBH} with the metallicity results of the final sample M_{SMBH} as function of metallicities from individual line-intensity ratios (Z_{ind}) as seen in Figure

A.15. A comparison of M_{SMBH} was also made with the best metallicity estimate, Z_{best}. This is illustrated in Figure A.16.

The M_{SMBH} showed essentially no trend with most Z_{ind}, as can be seen from Figure A.15. However, it is interesting to note that the only line-intensity ratio (Z_{ind}) which showed some correlation with M_{SMBH} was $Z_{ind}(NV/HeII)$, one of the line-intensity ratios we decided to neglect in our final metallicity analysis due to their deviant behaviour as compared to other line-intensity ratios.

Comparing Mass And Luminosity

To compare the relation between the mass of the supermassive black hole and continuum luminosity for the N-quiet sample and N-loud sample, M_{SMBH} is plotted as a function of L_{λ} in Figure A.17, for the two sample sets.

Comparing Mass And $FWHM(CIV)$

Figure A.18 shows the comparison of M_{SMBH} as a function of $FWHM(CIV)$ for the two sample sets. There is a strong correlation, as is expected from the way in which M_{SMBH} is calculated (see Section 2.5). The lower M_{SMBH} for the N-Loud sample comes mainly from the narrower line widths found in those objects. Given the relative weakness of the N-lines, this might in principle be due to a selection effect where narrower N-lines are easier to detect. However, we identified the N-Loud objects using an automated procedure which our tests show are insensitive to such effects for lines-widths at least up through $(FWHM(CIV)) = 3.5$, which are essentially the broadest lines seen in either the Intermediate or the N-Loud Quasar Sample.

Comparing Mass And $EW(CIV)$

Finally, we check for the relation between the mass of the supermassive black hole, M_{SMBH} and the continuum reprocessing efficiency of the BELR for CIV line, quantitatively estimated by the equivalent width, $EW(CIV)$ for the N-Loud sample only. This is shown figuratively in Figure A.19. The relation between continuum luminosity, L_λ and $EW(CIV)$ is shown in Figure A.20. For the N-Loud sample, for which we measured $EW(CIV)$, it seems to follow the often seen Baldwin effect, showing an anti-correlation between M_{SMBH} or L_λ and $EW(CIV)$. The effect is, however, better pronounced in L_λ and $EW(CIV)$ relation.

Chapter 9: Discussion

9.1 Metallicity And The BELR LOC Model

In our study of BELR metallicities of N-Loud Quasars in the SDSS DR5, using different line-intensity ratios and the predictions of the LOC Model, we have found that all line-intensity ratios except NIV]/CIV and NV/He II imply similar metallicity values and therefore are valid abundance indicators. The deviant behaviour of the two ratios which we have come to know from this study suggests that the LOC Model needs to be refined.

The line-intensity ratios will indicate different metallicities if the parameters in the LOC model used by Hamann et. al. (2002) do not correctly describe the QSO in question. Now because the LOC model gives very different results for the two line-intensity ratios for the majority of the N-Loud sample, this implies that something common is going on in all QSOs as these two different values in Z_{ind} is not restricted to only a few QSOs. Previous papers on metallicity of QSOs have also reported that Z is significantly different as measured by NIV]/CIV [Dietrich et. al., 2003; Shemmer and Netzer, 2003] and NV/He II [Dietrich et. al., 2003] as compared to other line-intensity ratios.

Nagao et. al. (2006), studied 5344 QSOs from SDSS DR2, by forming composite spectra in different redshift (z) and luminosity (L) bins. They found no evolution of metallicities with z (in range $2.0 \leq z \leq 4.5$), however, some evolution was found with L. They infer the metallicities for different composite spectra based on the

LOC model predictions for various line-intensity ratios and found the average quasar metallicities in various bins to be $5Z_{\odot}$ in low L bins and reaching up to $10Z_{\odot}$ in the highest L bins. However the line-intensity ratios for Z estimation are not the same as ours except for NV/CIV and NV/He II.

Dietrich et. al. (2003) studied chemical enrichment in 70 high $z(\geq 3.5)$ QSOs and found an average metallicity of $5.3Z_{\odot}$ with highest metallicities reaching upto $10Z_{\odot}$. They found some positive correlation of Z with L but no trend between Z and z was seen.

Here we have studied the 42 QSOs with the strongest NIII] and NIV] lines, suggesting also the highest metallicities. We find a $Z_{median} \sim 6.4Z_{\odot}$, with a third of them having $Z \geq 10Z_{\odot}$ and and a highest value of $Z_{max} \sim 22Z_{\odot}$. This is consistent with our sample representing the upper end of the same Z distributions studied by Nagao et. al. (2006) and Dietrich et. al. (2003).

9.2 Chemical Evolution Models And Extreme Metal Rich Quasars

The metallicity of the N-rich sample is super-solar and can reach up to and above $20Z_{\odot}$. This can be used to constrain the chemical evolutionary history of the BELR gas and hence it is possible to rule out certain models of chemical evolution in quasars.

Quasars have been linked to massive galaxies based on several observational results. In particular, QSOs are now believed to be a stage in the evolutionary histories of galaxies. Thus chemical evolution models of galaxies have been used in the study of BELR abundances in order to understand the physical conditions therein and its link to the host galaxy. Several models of chemical evolution of galaxies have been developed over the years. These differ from one another mainly in the input parameters like *Initial Mass Function* (IMF) and the *gas infall timescales* as well as details of the various physical processes going on in the ISM of the galaxy.

An important set of such models were computed by Hamann and Ferland (1993) (HF93). They are one-zone closed box models of chemical evolution in galaxies in order to explain the line-intensity ratios observed in the QSOs. Figure 3 in their paper shows the metallicity (Z) predicted by each of these models as a function of time (t), since the beginning of star formation in the galaxy. We reproduce that figure here as the main part of our Figure A.21. HF93 start by developing a reference solar neighborhood model, M1 in order to calibrate the nucleosynthesis contributions from different types of stars. The three free parameters used in the calculation of chemical evolution in a given model are, *the shape of the IMF*, *the star formation rate* and *the timescale for gas infall* which essentially accounts for the mass buildup of the system. The IMF is normalised and is a power law of the form $\phi \sim M^{-x}$. The timescale for gas infall comes in the form of the *stellar birthrate function*, $\psi(t)$, which scales linearly with gas density. It is of the form, $\psi(t) \sim \nu G(t)$, where ν is a constant input parameter and is a measure of *star formation rate* (SFR) and $G(t)$ is the *gas density at time t*. The results are mainly sensitive to the timescale of gas infall and star formation. Finally in all models the chemical evolution is halted when the remaining gas is less than 3% of the total mass.

In the solar neighborhood model M1, in HF93, the IMF has a slope, $x \sim 1.1$ for $M \leq 1M_{\odot}$ and is $x \sim 1.6$ for higher mass stars. The timescale of gas infall is taken to be 3 Gyr. This model has the lowest Z at all epochs and reaches only up to $1Z_{\odot}$. Model M2 uses a flatter IMF with $x \sim 1$ for all masses and the timescale for gas infall remains the same as in model MI. The flatter IMF leads to more processing by high mass stars leading to higher Z at all epochs compared to M1. However the metallicities reached are not yet quite as high as those seen in QSOs. The model M3 uses an IMF similar to that in M1 but with a shorter infall timescale of 0.05 Gyr. This is also the infall timescale used in the models of massive galaxies. The star formation rate, as a result shoots up to be 20 times higher than that of M1. Also, Z rises more quickly here than either in M1 or in M2. and then declines because star formation is halted when gas fraction reaches 3%. The model M4 combines a relatively flat IMF ($x \sim 1.1$) with the shorter timescale of 0.05 Gyr. These parameters are appropriate for the Giant Elliptical galaxies. This model provides a good fit for the observed metallicities in high z QSOs. The metallicity peaks at $10Z_{\odot}$, and then falls off to about $6Z_{\odot}$, which is the median metallicity of the N-Loud QSOs studied here. However, this still does not explain the highest metallicity QSOs found in our study. The last two models of HF93, put a cut-off limit on miminum mass of stars at $2.5M_{\odot}$. Model M5 has a slightly higher star formation rate than M4, it has a flatter IMF, $x \sim 1$, and shorter infall timescale of 0.05 Gyr, with the minimum mass cut-off of $2.5M_{\odot}$. The lack of low mass stars leads to much less mass locked up in stars and stellar remnants and therefore this model reaches even higher Z. Model M6 uses a steeper IMF of $x \sim 1.6$, yet reaches higher Z because of the minimum mass cutoff limit. These models do reach a high metallicity of 35 $Z_{\odot}$, although they are rather unphysical owing to absolute lack of low mass stars.

An additional set of chemical evolution models was developed by Friaca and Terlevich (1998). They differ from the HF93 models in some important details which intend to more realistically describe a galactic environment. They are multi-zone models which follow the dynamical evolution of the gas by including the several episodes of gas inflows and outflows and in particular the evolution of a galactic wind; instead of the simple one-zone models of HF93. Further they do not put a sharp cut off limit of 3% for the remaining gas as the halting point of star formation in the galaxy. Instead, they include inhibition of star formation when the gas density is too low or when the gas is expanding. Finally they adopt the Saltpeter's IMF with $x \sim 1.35$. In the example for which they describe results, the evolution in the chemical abundances is very similar to HF93 model M3 (which uses a similar IMF), with a maximum value of $Z \sim [O/H] \sim 4$ reached after 1 Gyr.

Romano et. al. (2002) also discusses the chemical evolution in massive spheroids at high z, using one-zone ISM and taking into account the effects of cooling and stellar feedback. They found a similar 1 Gyr timescale for reaching the peak metallicity, but that the peak metallicity reached ($Z \sim 1.3Z_{\odot}$) is much lower than that in the HF93 models. It is also possible that the metal enrichment occurs on more localised scales closely associated with the AGN central engine [see e.g., Collin and Zahn, 1999].

Based on our findings we can rule out models where metallicities do not reach the same as we have found in our study. The HF93 models M1and M2 can most certainly be ruled out (see Figure A.21 which shows the qualitative location of Z in the our N-loud sample set on the chemical evolution models). This cannot be explained based on the high redshifts of the Quasars where the age of the Universe is considerably less ($\sim$ 1 Gyr) than the time needed for metallicities to reach as high as $20Z_{\odot}$. The observed metallicities in N-Loud QSOs can also be used to put constraints on the IMF favourable to evolution of galaxies resulting in such high metallicities in such short amount of time.

The only models that predict $Z \geq 5Z_{\odot}$ are those of HF93. These are admittedly very simplified models, but they do serve to bring out the interplay between the shape of the IMF and the maximum metallicity that is reached. It is important to keep in mind that our metallicity results do not depend on any of these enrichment models. They convert measured emission line-intensity ratios to metallicities using just the physics contained in $CLOUDY$, and the LOC Model to then describe the distribution of clouds. While the LOC Model obviously is not quite a rigorously correct description of the average QSO, and the individual QSOs will be different from the average, it still does produce the same Z for 6 of the 8 line-intensity ratios used here and therefore does seem to be fairly accurate. Our results therefore do appear to show that some QSOs do indeed reach high metallicities, with $Z \geq 10Z_{\odot}$

and probably in the neighborhood of $20Z_{\odot}$. The only way to escape this conclusion would be to abandon our basic assumption that N is a secondary element, so that the N/O abundance ratio, which is what we actually measure, would no longer be proportional to O/H, which is what we call metallicity, Z.

The model which best explains the high metallicity in quasars is the Giant Elliptical model. However this model also reaches only up to $Z \sim 10Z_{\odot}$ and then flattens out. Models M5 and M6 of HF93 do reach higher metallicities. They put a cut-off limit on minimum mass stars that can be formed, that may not be very physical, but they may still be indicating that a very top-heavy IMF is needed. An alternative explanation of the extreme metallicity QSOs in the context of Giant Elliptical model is the infall of gas from the outer regions of the Quasar host galaxy right after it reached its peak, causing a further burst of star formation not included in the enrichment models. Mergers of galaxies might also result in enhanced metallicities.

Our sample of 42 N-Loud QSOs has presumably picked off the highest metallicity end of a broader range in Z among the thousands of SDSS QSOs. One possible way to interpret these results is in the context of the proposal by Silk and Rees (1998) that QSOs gestate out of sight, enshrouded by dust in the centers of galaxies, and then only become visible at the very end of the process of building the massive black hole, when the luminosity becomes high enough to blow away or evaporate the remaining dust. This carries with it the implication that in most QSOs we are seeing the final end-state reached in the chemical enrichment process. If so, then the different metallicities measured here would indicate that different host galaxies shut off metal enrichment at different metallicities. One explanation for such differences, suggested by the HF93 models, would be that there are differences in the IMFs in the host galaxies in a situation where chemical enrichment is stopped because essentially all of the gas has been turned into stars as is inherent in the HF93 models.

However, an alternate possibility fitting within the same general picture is that the enrichment is in fact halted by feedback from the QSO, and that $L \sim L_{EDD}$ is reached at different points in the enrichment process for different QSOs. A third possibility is that the QSOs are not as enshrouded as was suggested by Silk and Rees (1998), and that in fact we are seeing similar objects, all of which will reach, $Z \sim 20Z_{\odot}$, at different moments in their chemical evolution. This could be tested by converting the predicted $Z(t)$ curves for each model into histograms of the expected number of QSOs as a function of Z, and seeing if any of the models come at all close to fitting the observations. However, that would require a very careful combining of the distribution of metallicities measured here for our N-Loud sample with the distribution of metallicities measured for lower-metallicity objects by using just the NV/CIV ratio, in order to get the widest possible range in Z. Such a test is beyond the scope of this present work.

CHAPTER 10: SUMMARY AND CONCLUSIONS

A detailed abundance analysis was done on QSOs with strong nitrogen (N) lines (N-Loud QSOs) drawn from the SDSS DR5 Quasar Catalogue. A total of 42 such QSOs were found in the catalogue in the desired redshift range of $2.29 \leq z \leq 3.6$, which ensured the presence of required emission lines (NV λ1240, NIV] λ1486, NIII] λ1750, CIV λ1549, He II λ1640, OIII] λ1666 and CIII] λ1909) used in our abundance analysis method. Of these 42, 19 QSOs also had the OVI λ1034 emission line present in the observed range and hence that emission line was also used for abundance analysis. We then carefully deblended the blended regions to find the line-intensity ratios and the corresponding metallicity Z estimates using the predictions from the photoionisation code $CLOUDY$. In addition we also measured the $FWHM(CIV)$ and the continuum luminosity, $L_\lambda(1450\text{Å})$, to find the mass of the supermassive black hole, M_{SMBH} for the intermediate sample which consisted of all QSOs in the desired redshift range as given above, barring the ones where the CIV line was heavily absorbed or the data were missing. The Equivalent Width, *EW* of CIV line was also measured for N-Loud QSOs. In all above measurements, we used various IRAF and FORTRAN routines.

In order to get the best estimate of metallicity, we averaged the metallicity (Z_{mean}) from individual line-intensity ratios. However we found that the metallicity from line-intensity ratio NIV]/CIV shows a consistently *lower* Z value compared to the Z_{mean}. Also the line-intensity ratio NV/He II consistently shows *higher* values when compared to Z_{mean}. The fact that $Z's$ from these two line-intensity ratios do not agree with those from the other line-intensity ratios implies that either the gas density distribution as given in the LOC model is not accurate or the Z from these line-intensity ratios is not being correctly predicted by $CLOUDY$. In both cases LOC model needs to be improved if these two line-intensity ratios are also to be used in the final Z estimate, which is beyond the scope of present work.

We, therefore, decided to drop these two line-intensity ratios from our final best metallicity estimate, Z_{best}. The error in Z_{best} is taken to be its SDOM. We found that these N-Loud QSOs have super-solar metallicities with all of them having $Z_{best} \geq Z_{\odot}$, and about a third of these with $Z_{best} \geq 10Z_{\odot}$. The mean of this sample was $\sim 8Z_{\odot}$.

We found no evolution in M_{SMBH} with z. Also no trend was seen in the relation of M_{SMBH} and Z_{best}. While studying the relation between M_{SMBH} and Z from individual line-intensity ratios we found no correlation between the two variables as well. However a weak trend was seen with the two line-intensity ratios which we had decided to neglect from our best metallicity estimate, (NIV]/CIV and NV/He II). The $EW(CIV)$ showed a weak correlation with M_{SMBH} and $L_{\lambda}(1450\text{Å})$.

To see the implications of the very high metallicities found here, we compared our results to the predictions of published galactic chemical evolution models. The Hamann and Ferland (1993) models show that flat IMFs and rapid gas infall are needed to reach $Z \sim 10Z_{\odot}$, the value reached by 1/3rd of our sample. The highest metallicity that we found is $Z \sim 22Z_{\odot}$. The HF93 models require an exceedingly top-heavy IMF to reach such a high metallicity. We suggest the alternative that a recent starburst due to a merger might have pushed up the metallicity in a host galaxy that had already reached $Z \sim 10Z_{\odot}$.

APPENDICES

Appendix A: Figures For The Quasar Project

The following pages of Appendix A contain the figures for the Quasar Project of this thesis. They appear in the order in which they have been mentioned in the text in the earlier Chapters.

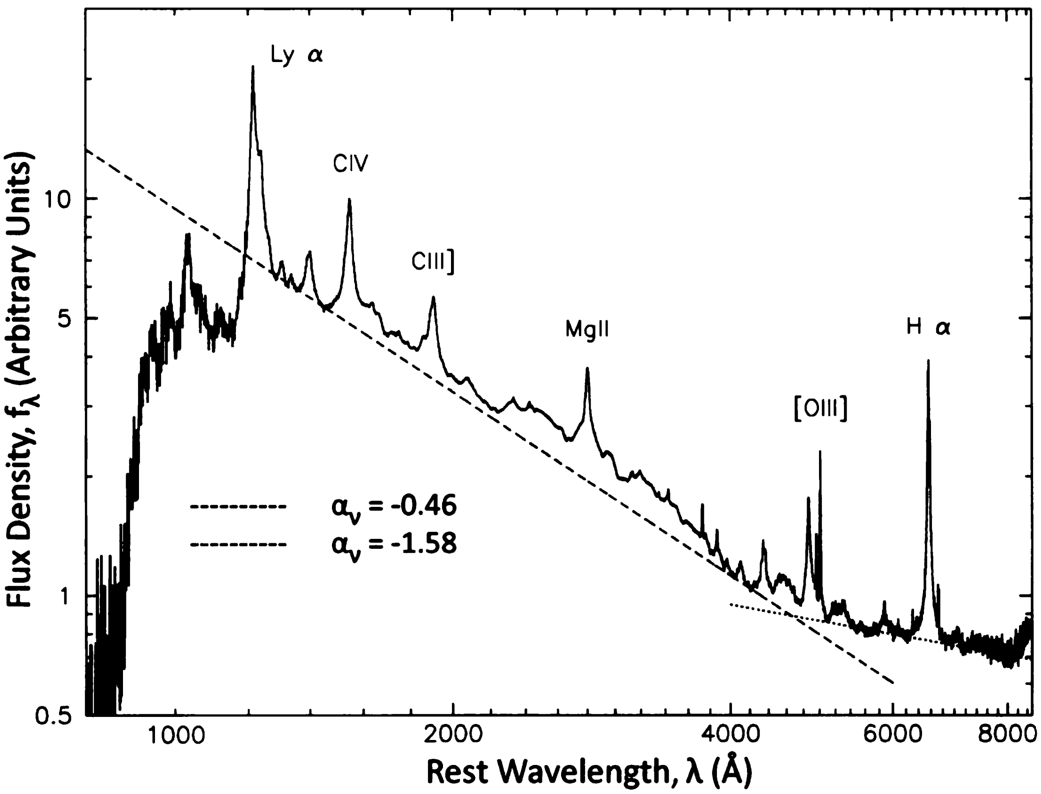

Figure A.1: Characteristic Quasar Spectrum.
This image is a composite spectrum from SDSS Data Release 1. Power-law fits to the estimated continuum flux are shown. The resolution of the input spectra is $R = \lambda/\Delta\lambda \sim 1800$, which gives a wavelength resolution of about 1 Å in the rest frame (Vanden Berk et. al., 2001).

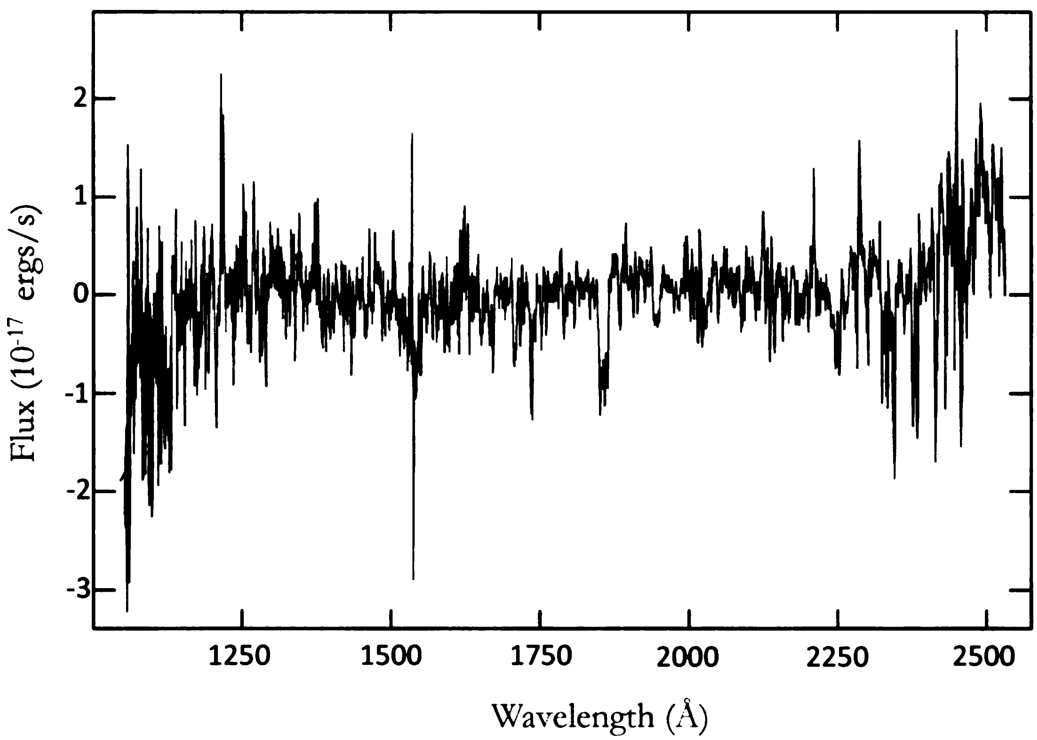

Figure A.2: Quasar Spectrum: An Example
(a) SDSS J 165806.76+611858.9, A Quasar with poor Signal-to-Noise ratio.

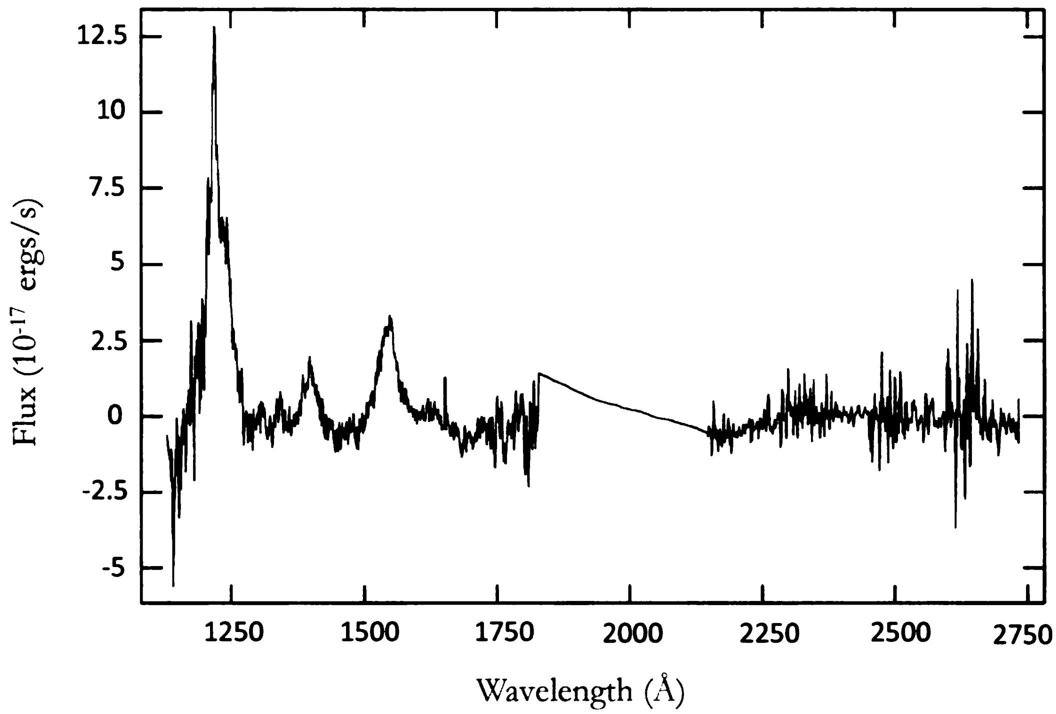

Figure A.2 *cont'd.*: Quasar Spectrum: An Example
(b) SDSS J 102753.89+661219.6, A Quasar with missing lines of interest.

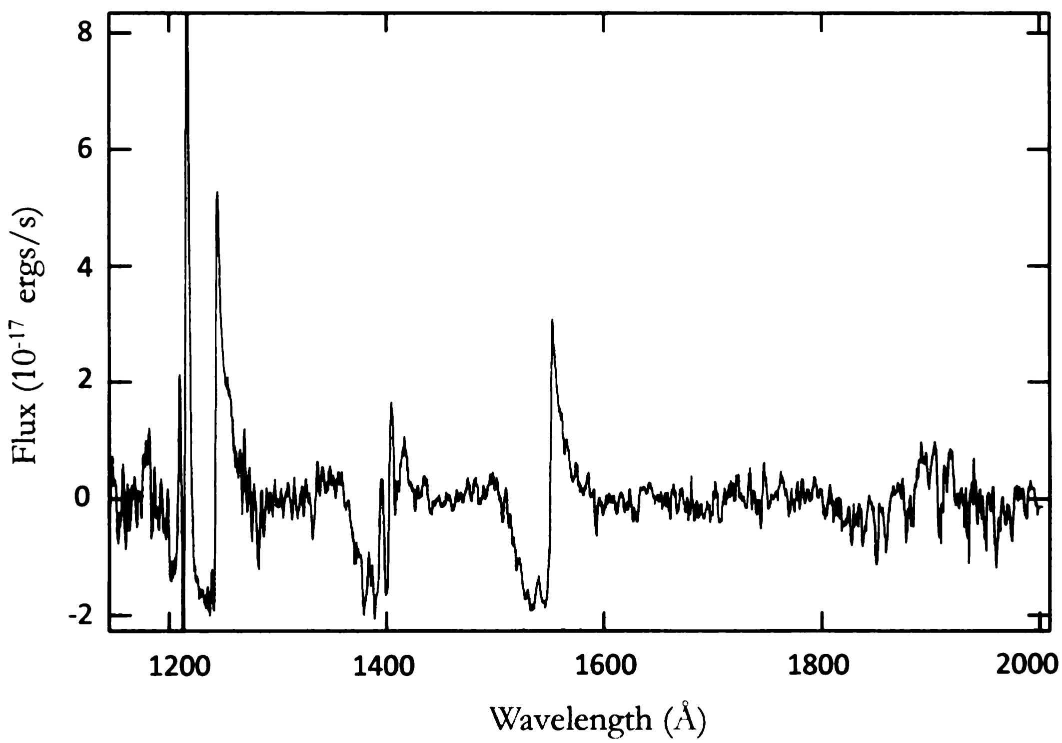

Figure A.2 *cont'd.*: Quasar Spectrum: An Example
(c) SDSS J 114056.81-002329.9, A Quasar with heavy CIV absorption.

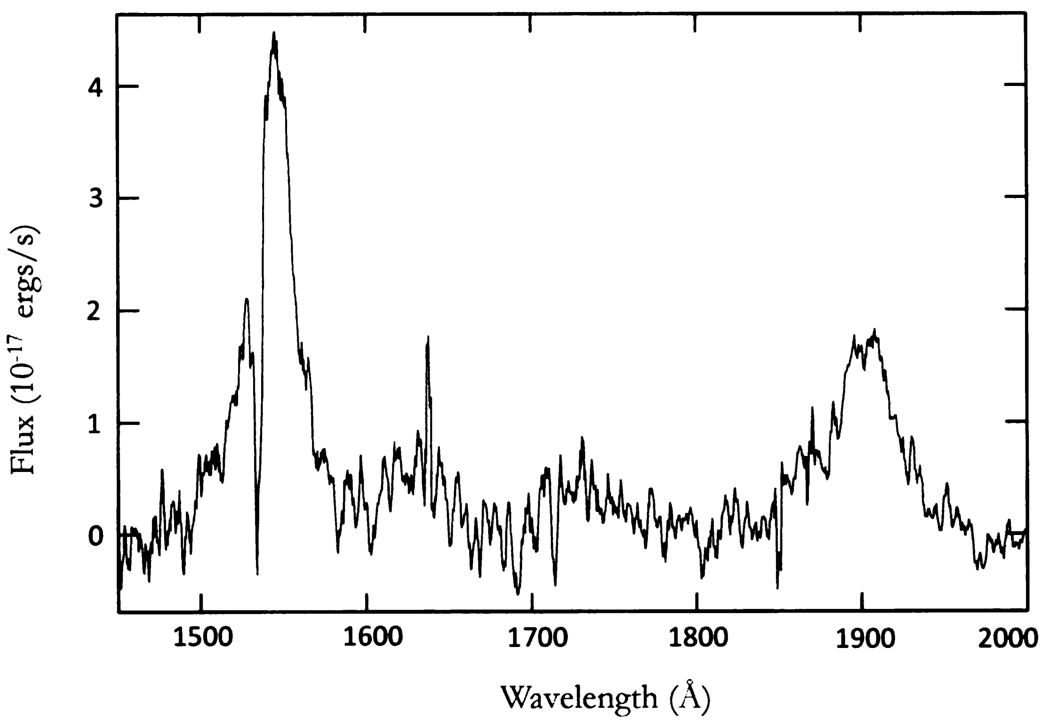

Figure A.2 *cont'd.*: Quasar Spectrum: An Example
(d) SDSS J 002337.54+003127.4, A Quasar with a spurious NIII] line.

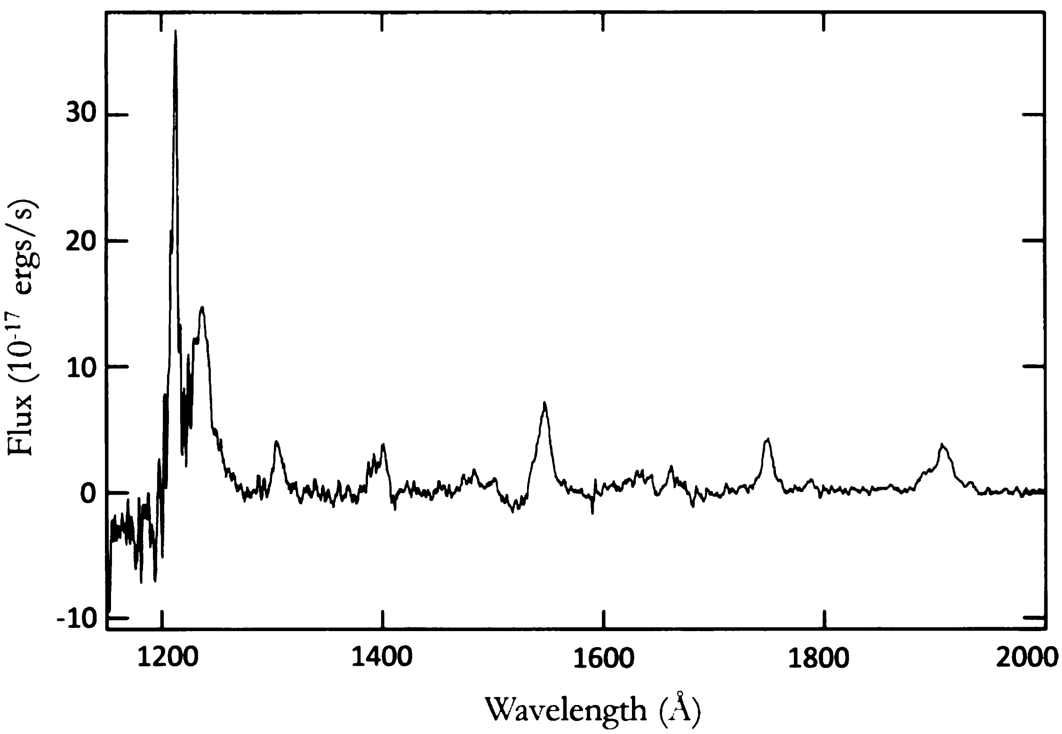

Figure A.2 *cont'd.*: Quasar Spectrum: An Example
(e) SDSS J164148.19+223225.2, A Quasar with strong Nitrogen lines.

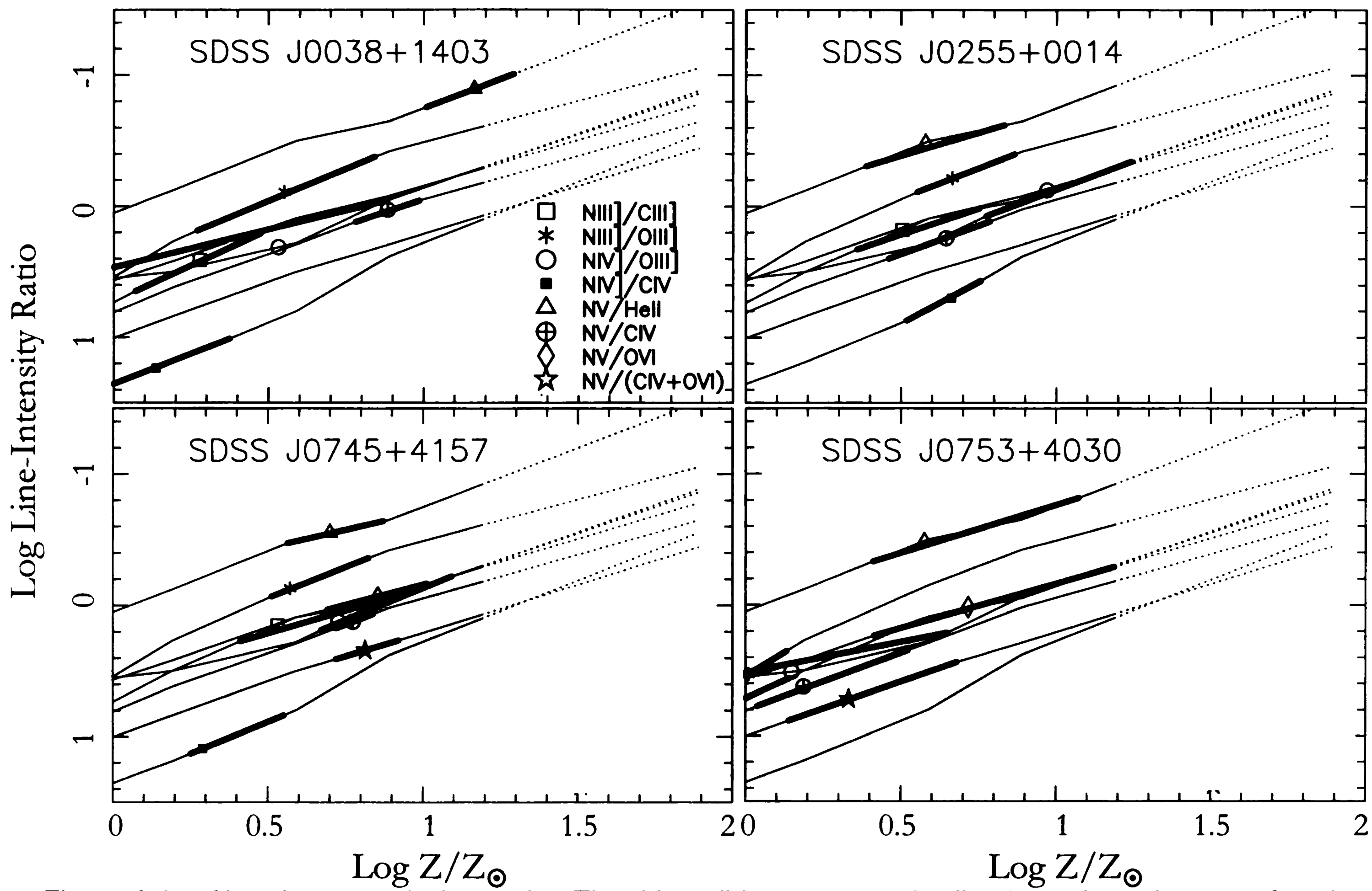

Figure A.3: Abundance analysis results. The thin solid curves are the line-intensity ratios as a function of metallicity (Z) predicted by the LOC models. The dotted portions of these curves are extrapolations beyond the highest Z for which a model was run. The symbols show the best measurements of each line ratio, and the heavy lines show the range uncertainty corresponding to the minimum and maximum line-intensity ratios.

Figure A.3 cont'd.

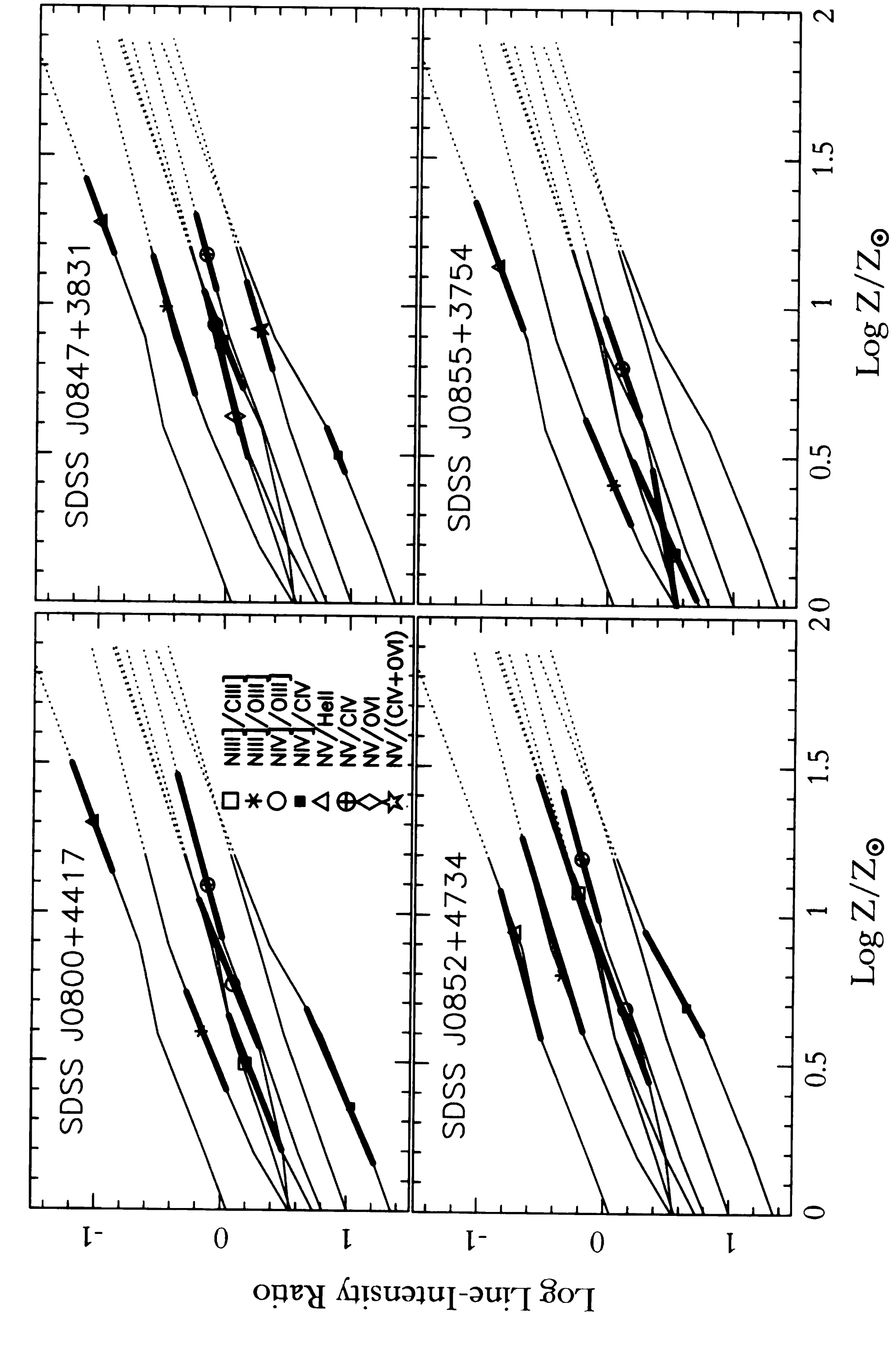

Figure A.3 cont'd.

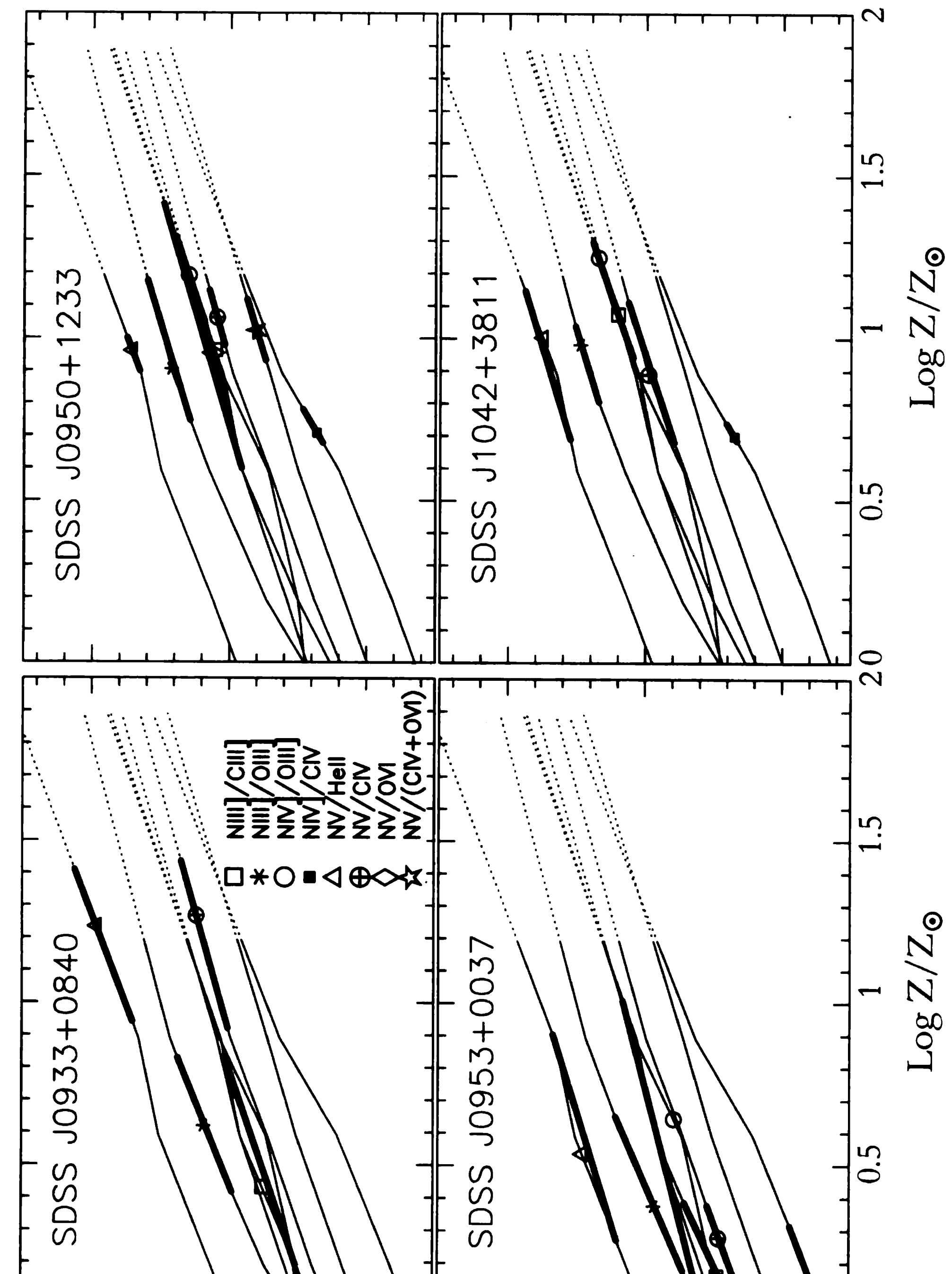

Figure A.3 cont'd.

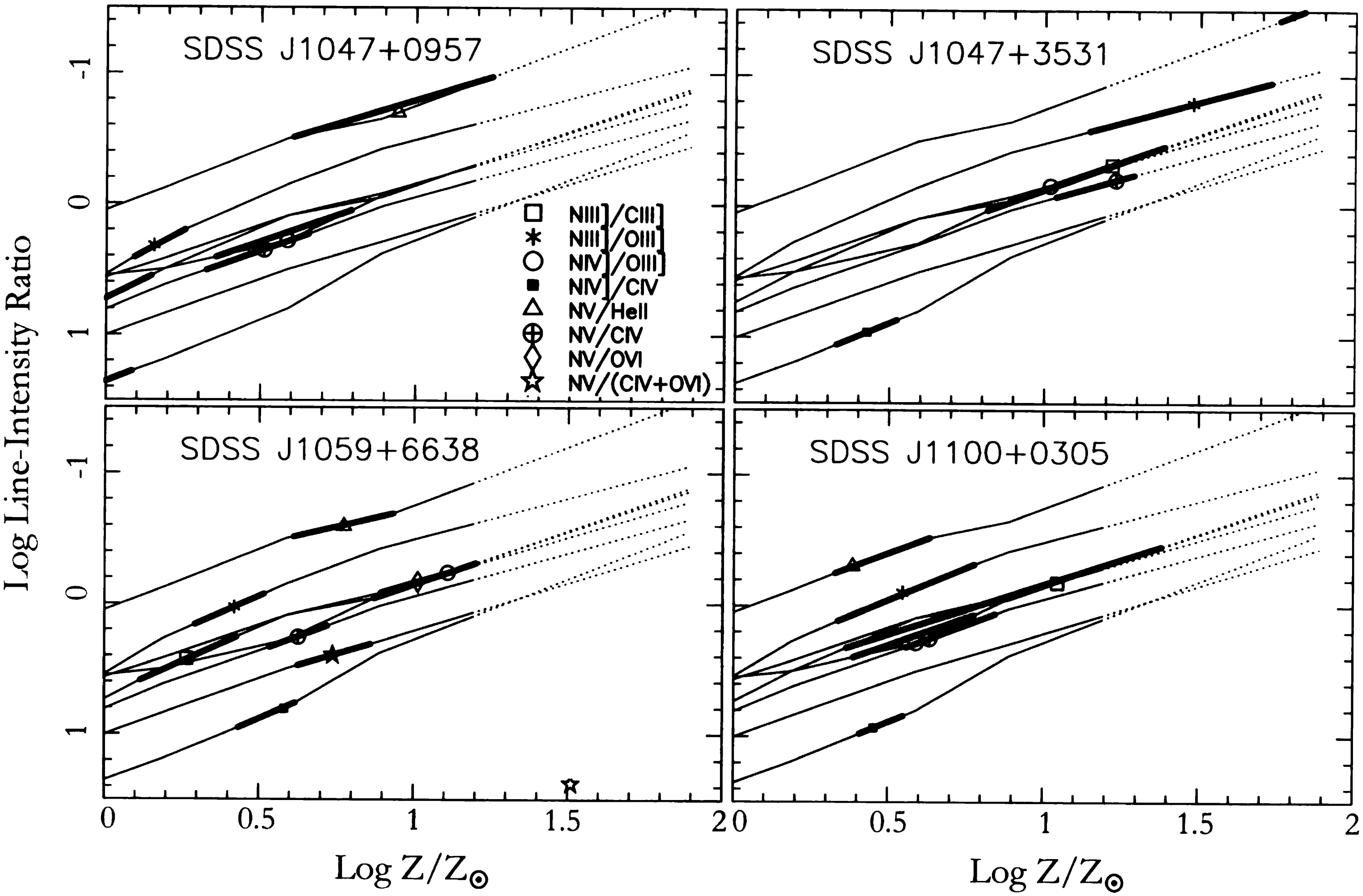

Figure A.3 cont'd.

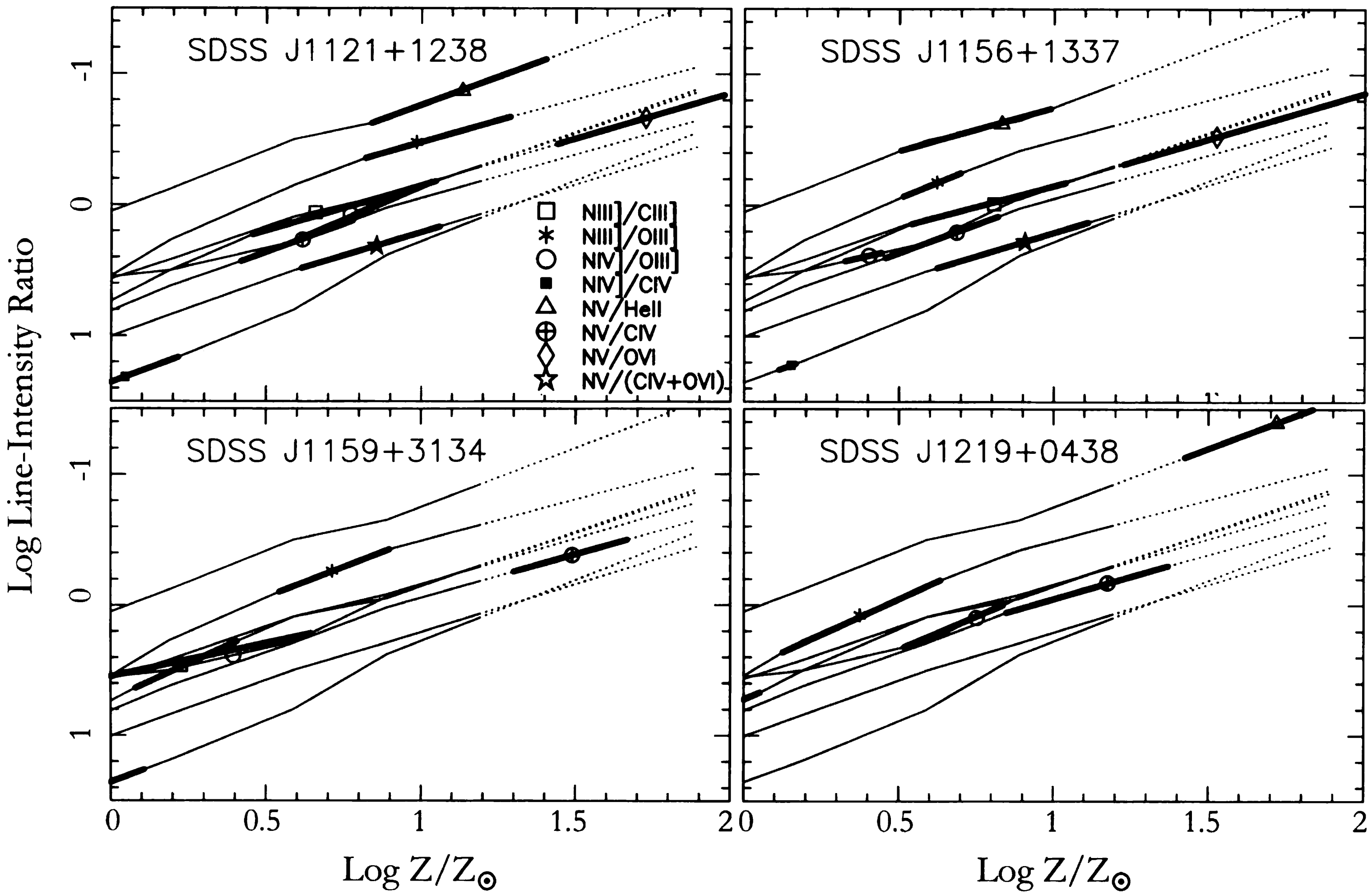

Figure A.3 cont'd.

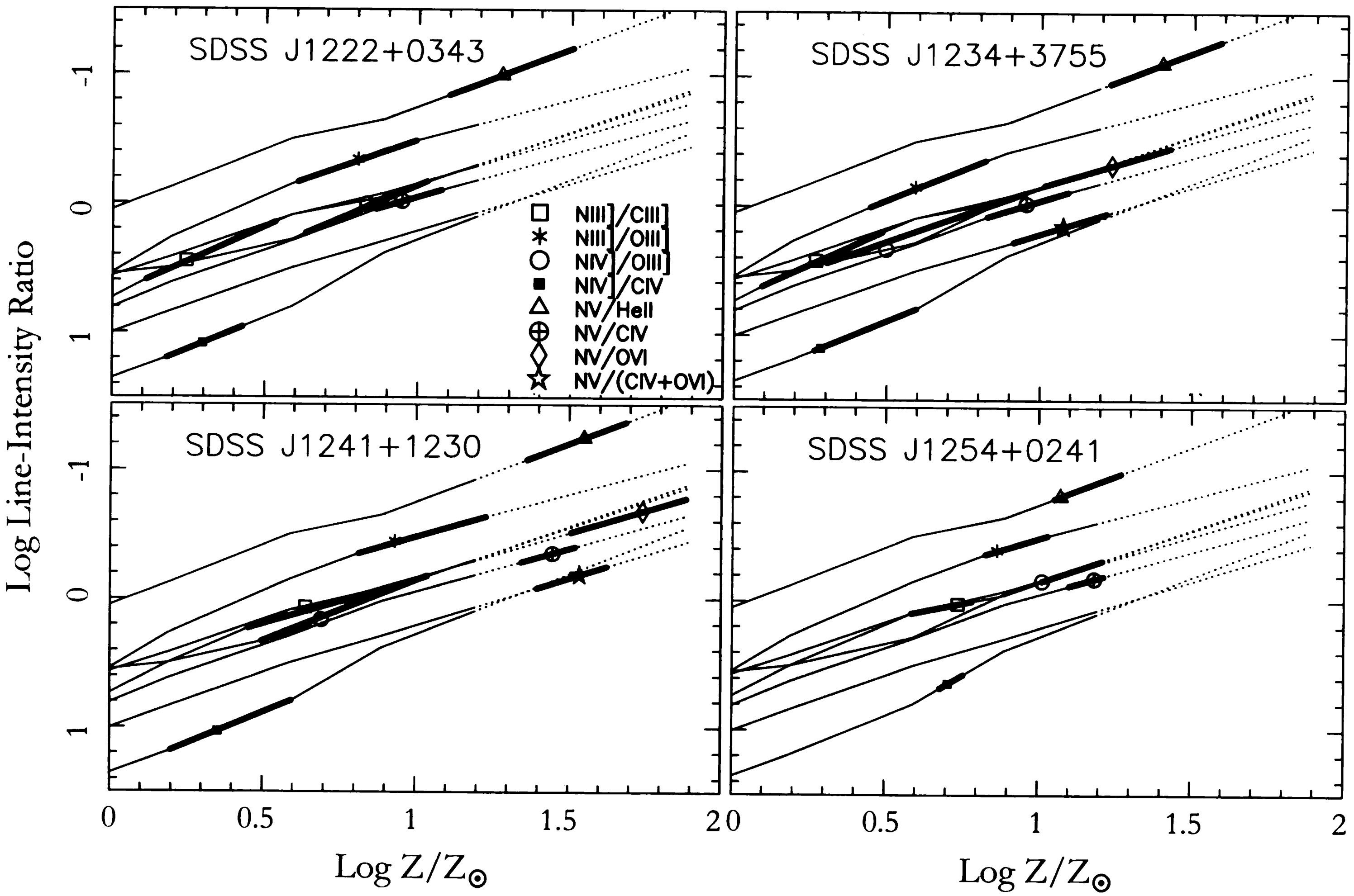

Figure A.3 cont'd.

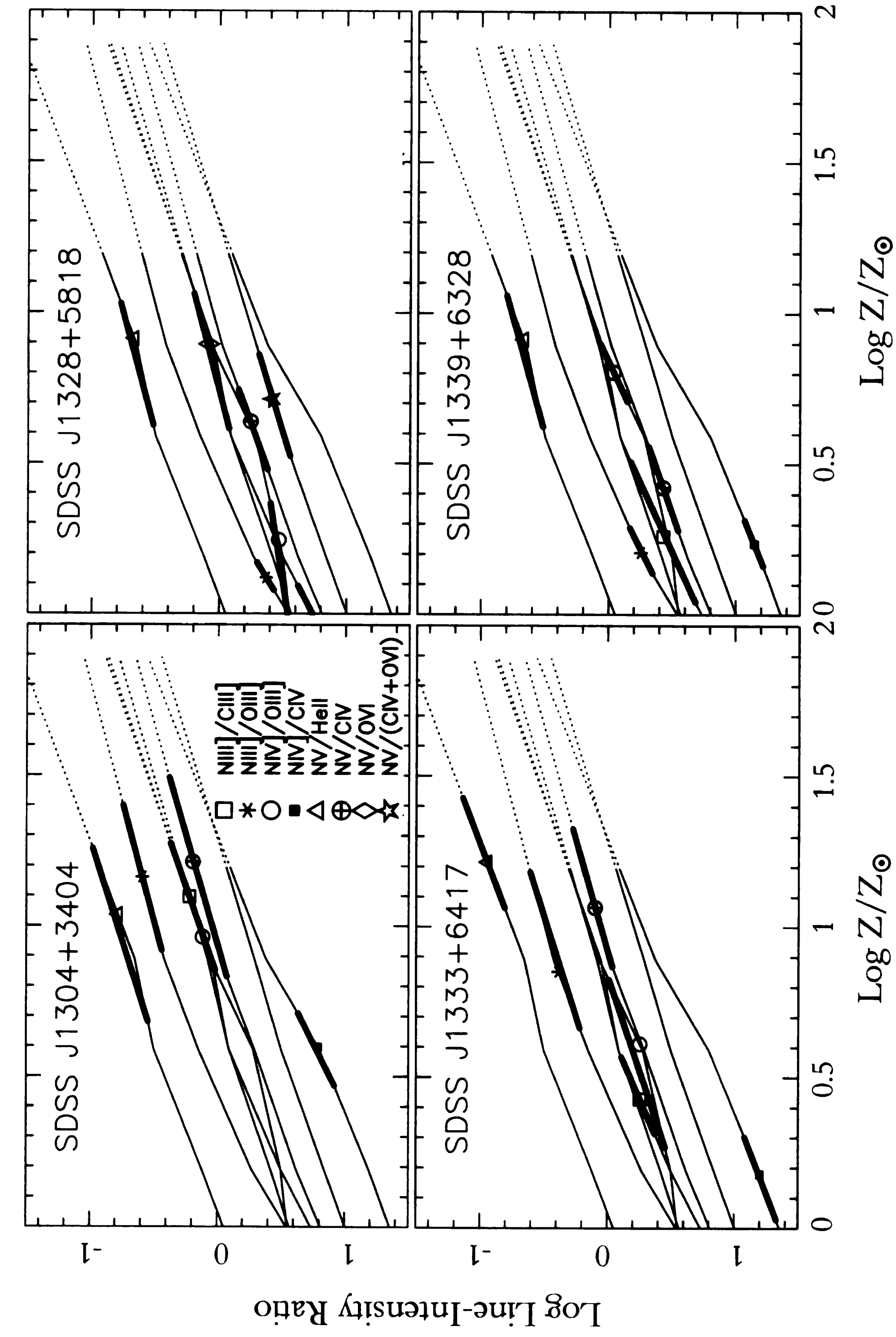

Figure A.3 cont'd.

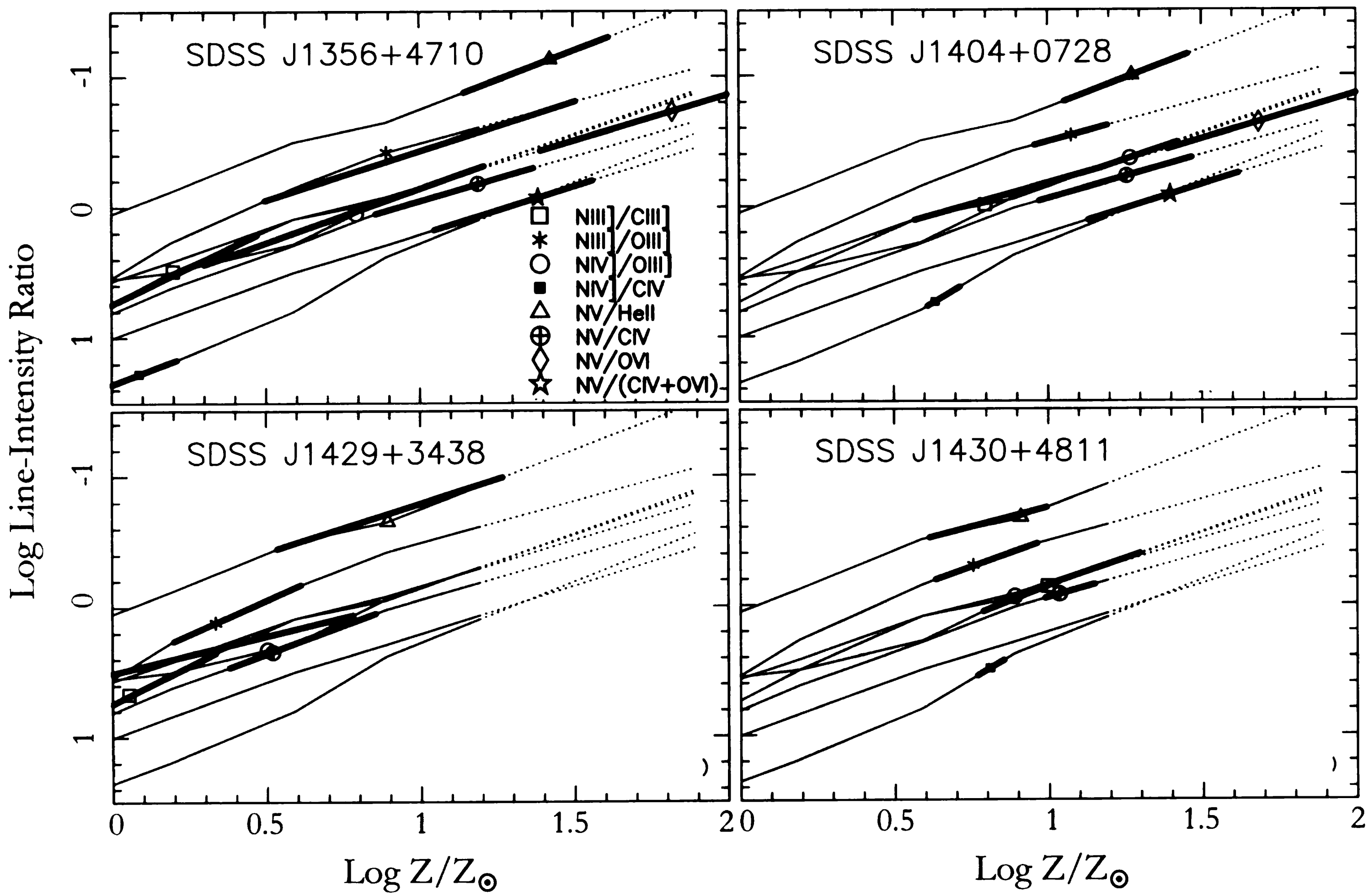

Figure A.3 cont'd.

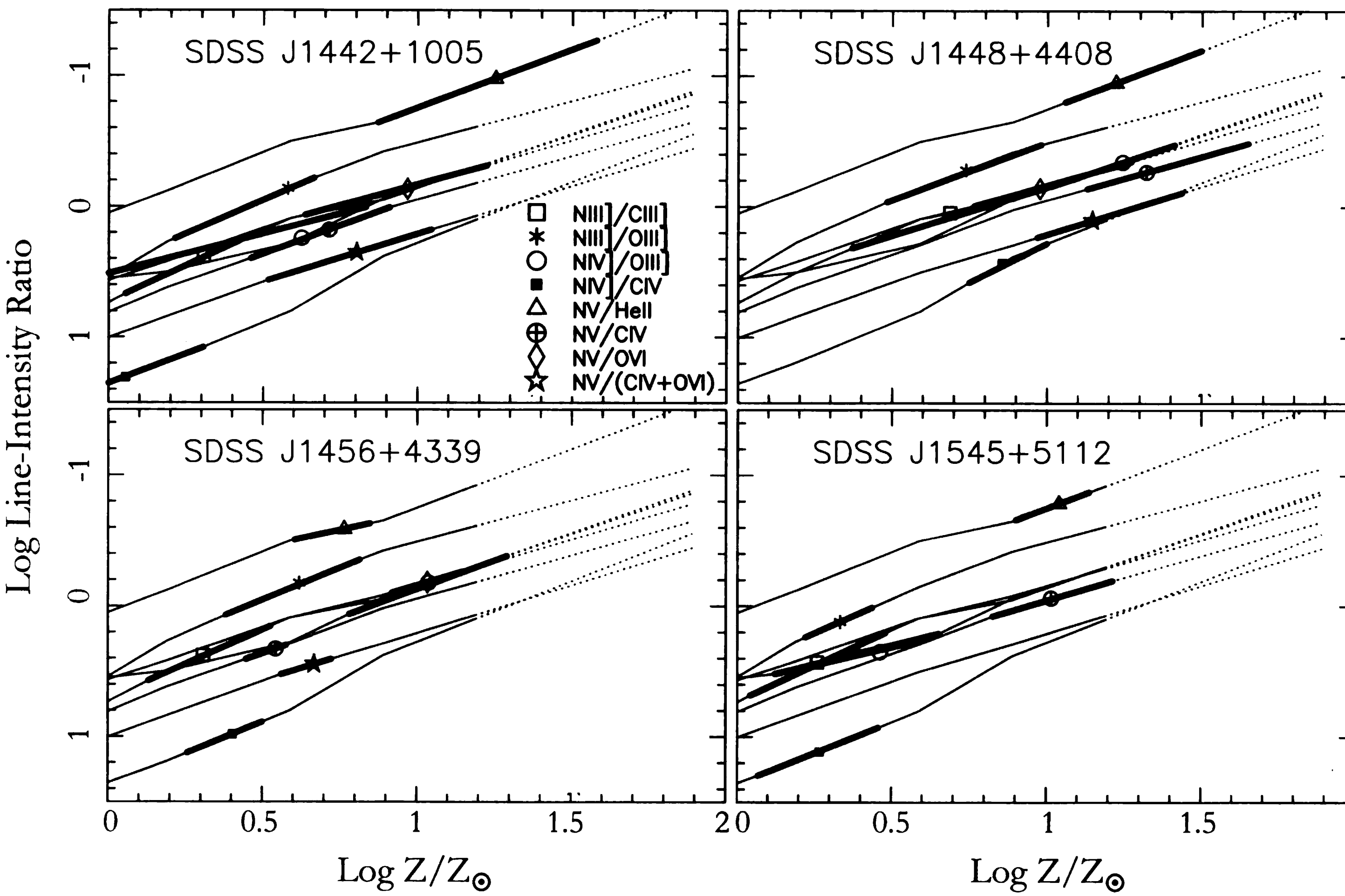

Figure A.3 cont'd.

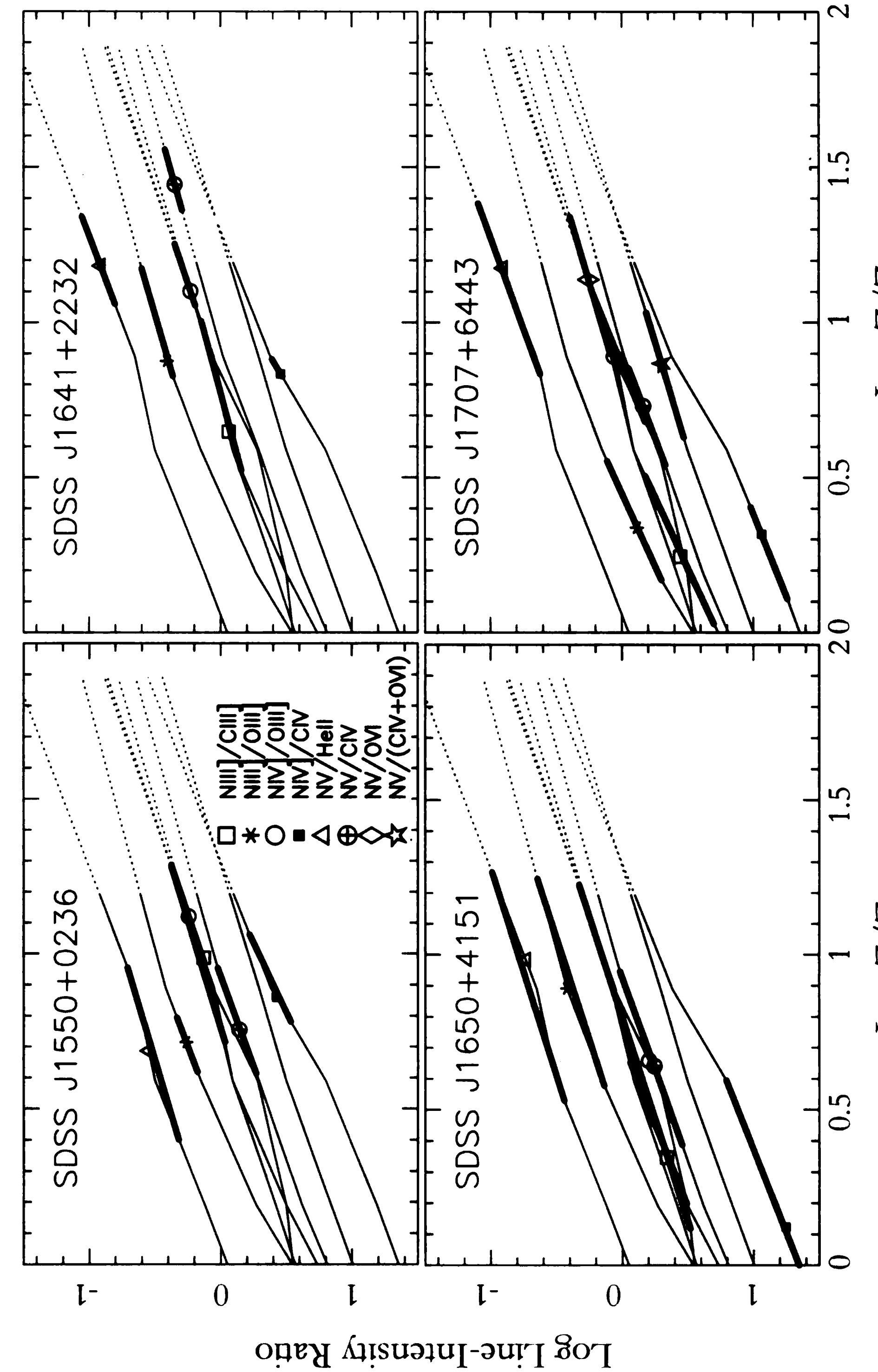

Figure A.3 cont'd.

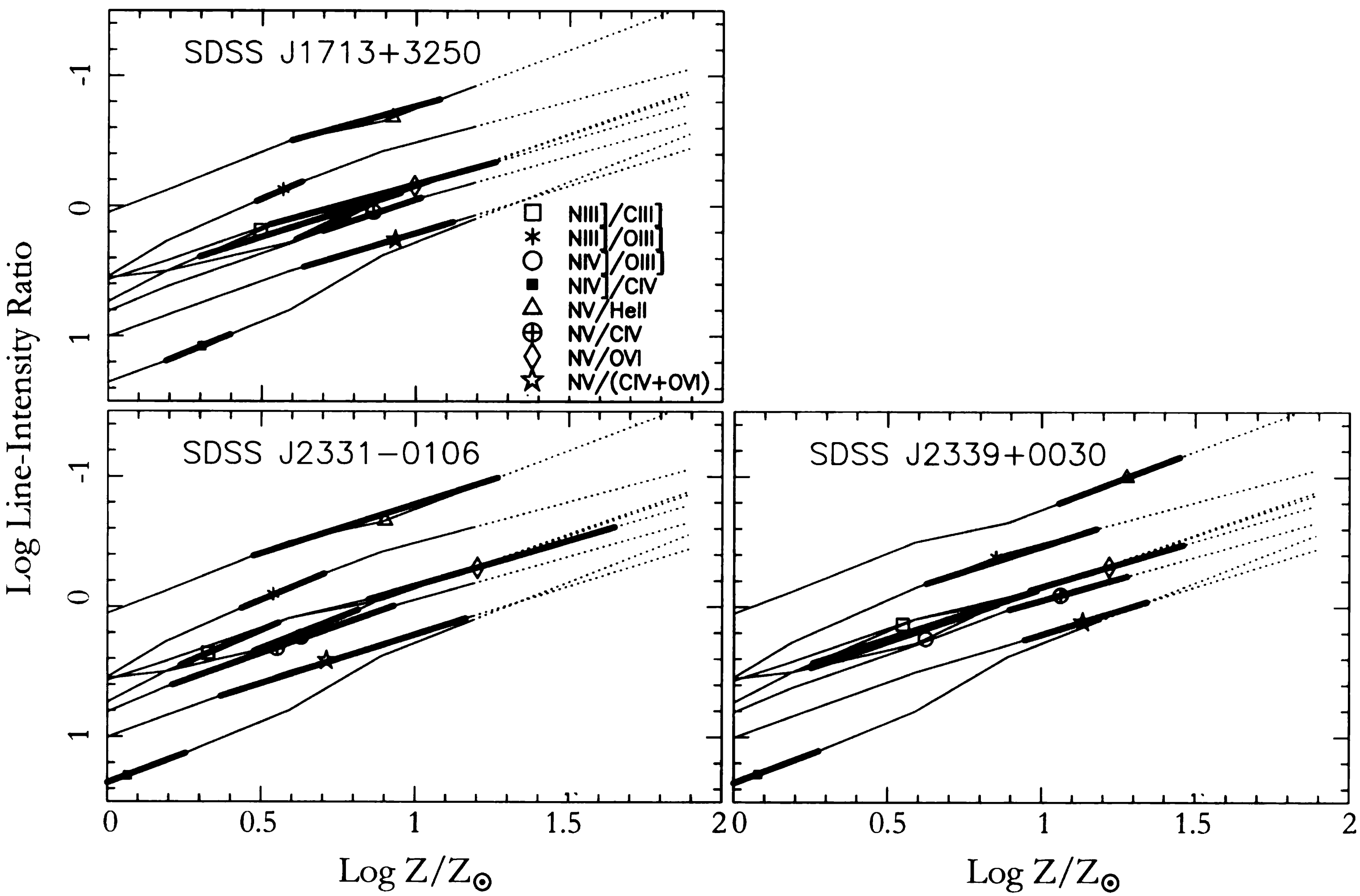

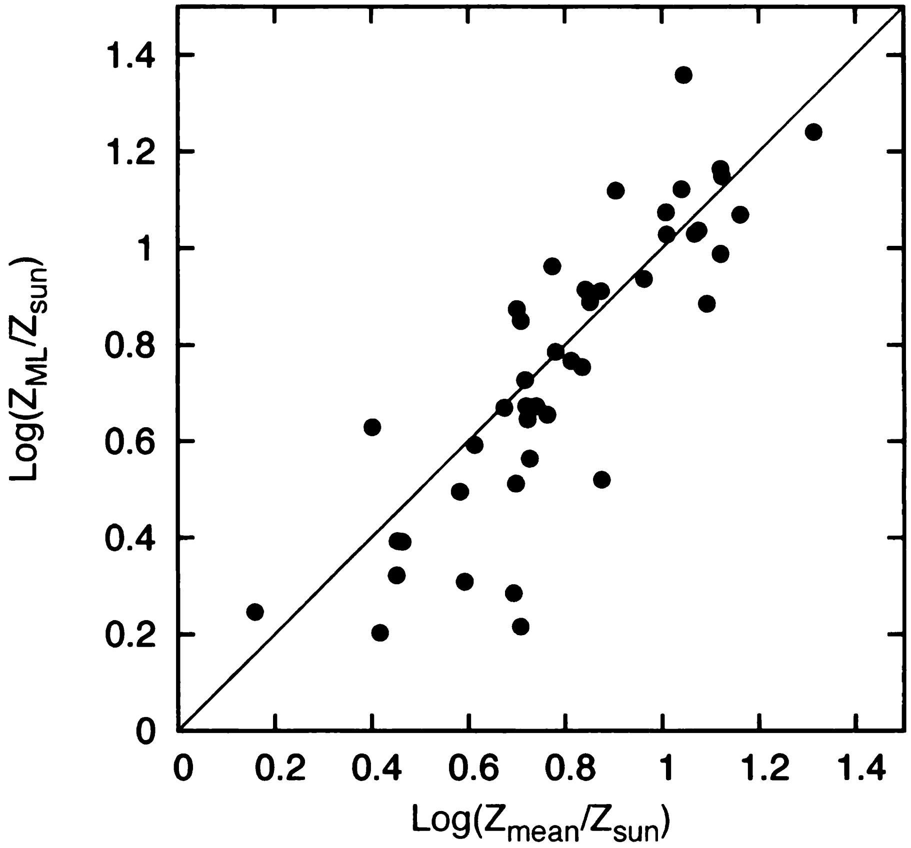

Figure A.4: Comparison of Maximum Likelihood Metallicity (Z_{ML}) and Mean Metallicity (Z_{mean}).

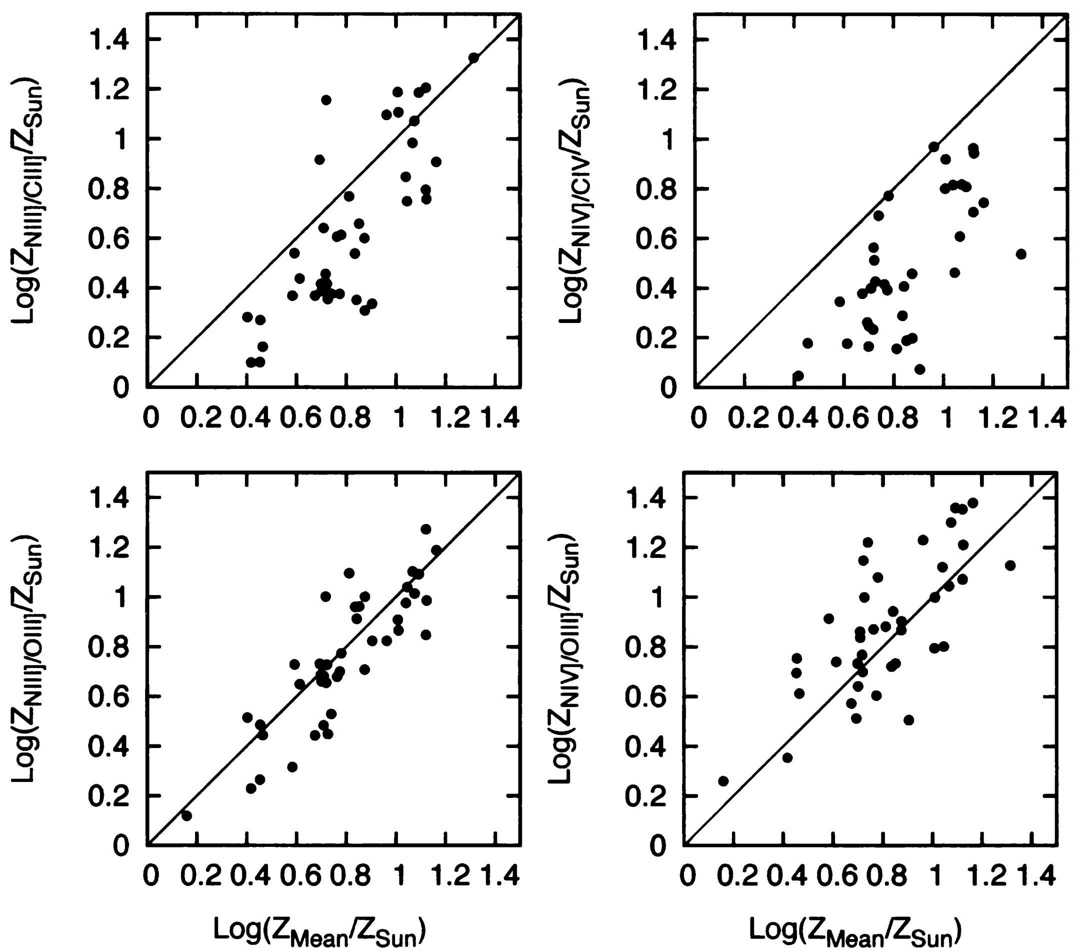

Figure A.5: Metallicity from individual line-intensity ratios as a function of mean metallicity.

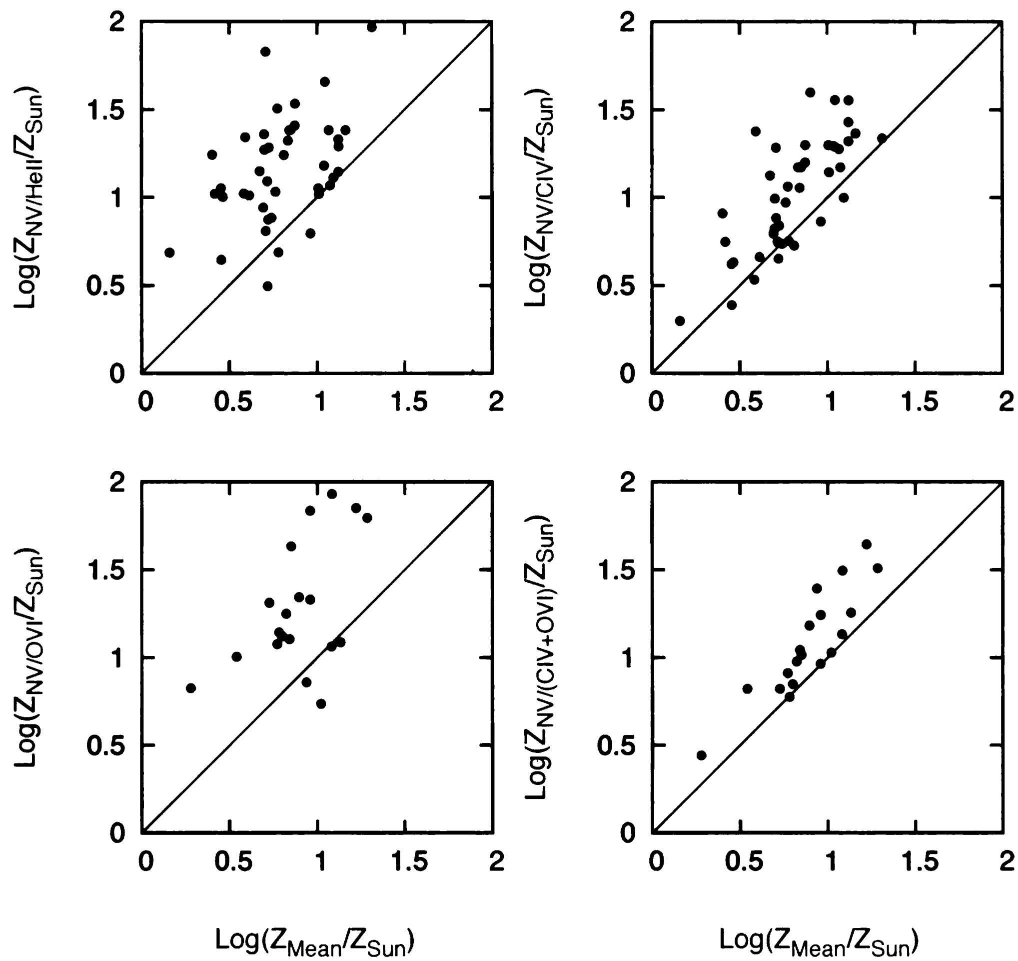

Figure A.5 *cont'd.*: Metallicity from individual line-intensity ratios as a function of mean metallicity. Note that in the last two graphs, which use the OVI line in the denominator; we have used the mean metallicity based on all eight line-intensity ratios.

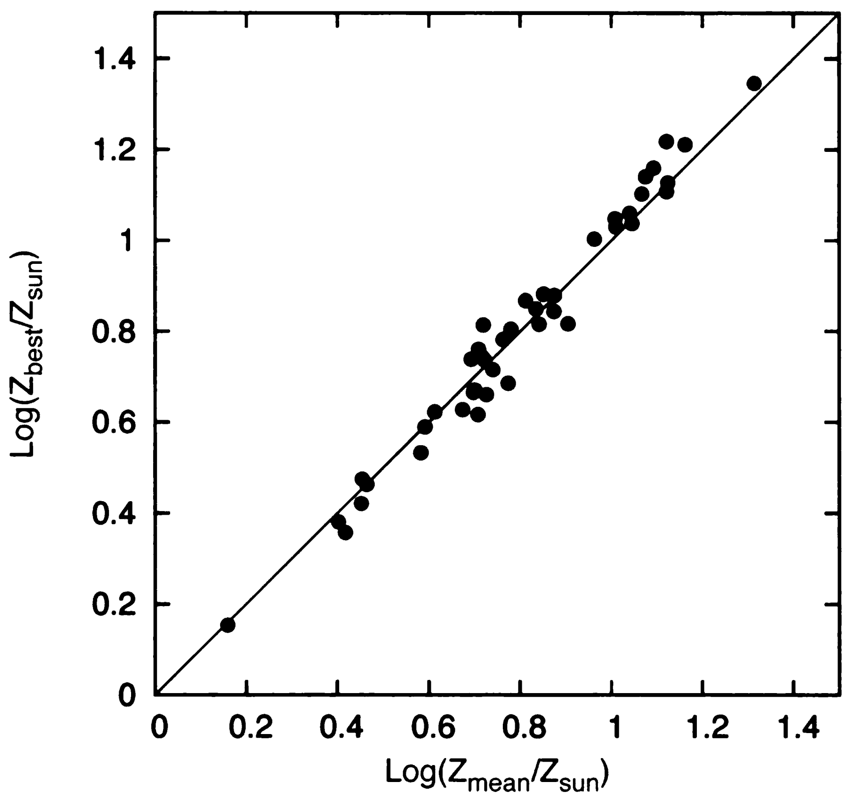

Figure A.6: Comparing Best Metallicity Estimate before (Z_{mean}) and after (Z_{best}) removing the two deviant line-intensity ratios (NIV]/CIV and NV/CIV).

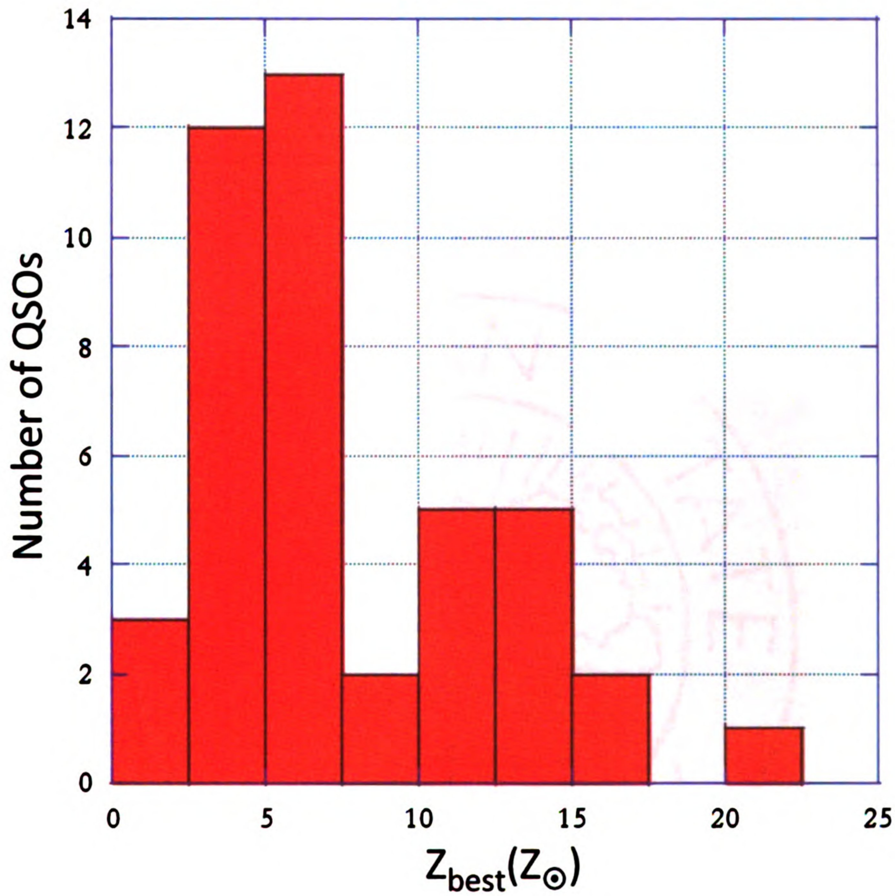

Figure A.7: Distribution of Best Metallicity Estimate (Z_{best}) in the N-Loud Quasar sample.

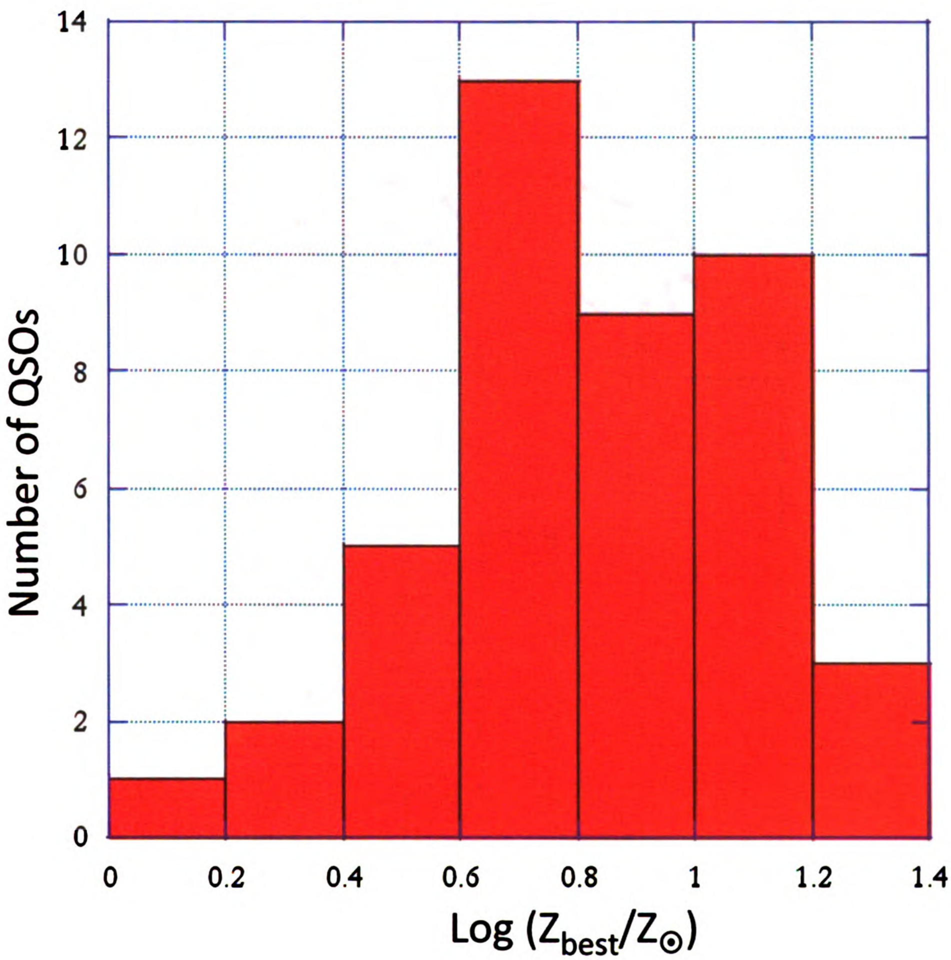

Figure A.7 *cont'd.*: Distribution of Best Metallicity Estimate (Z_{best}) in the N-Loud Quasar sample in Log space (Log Z_{best}).

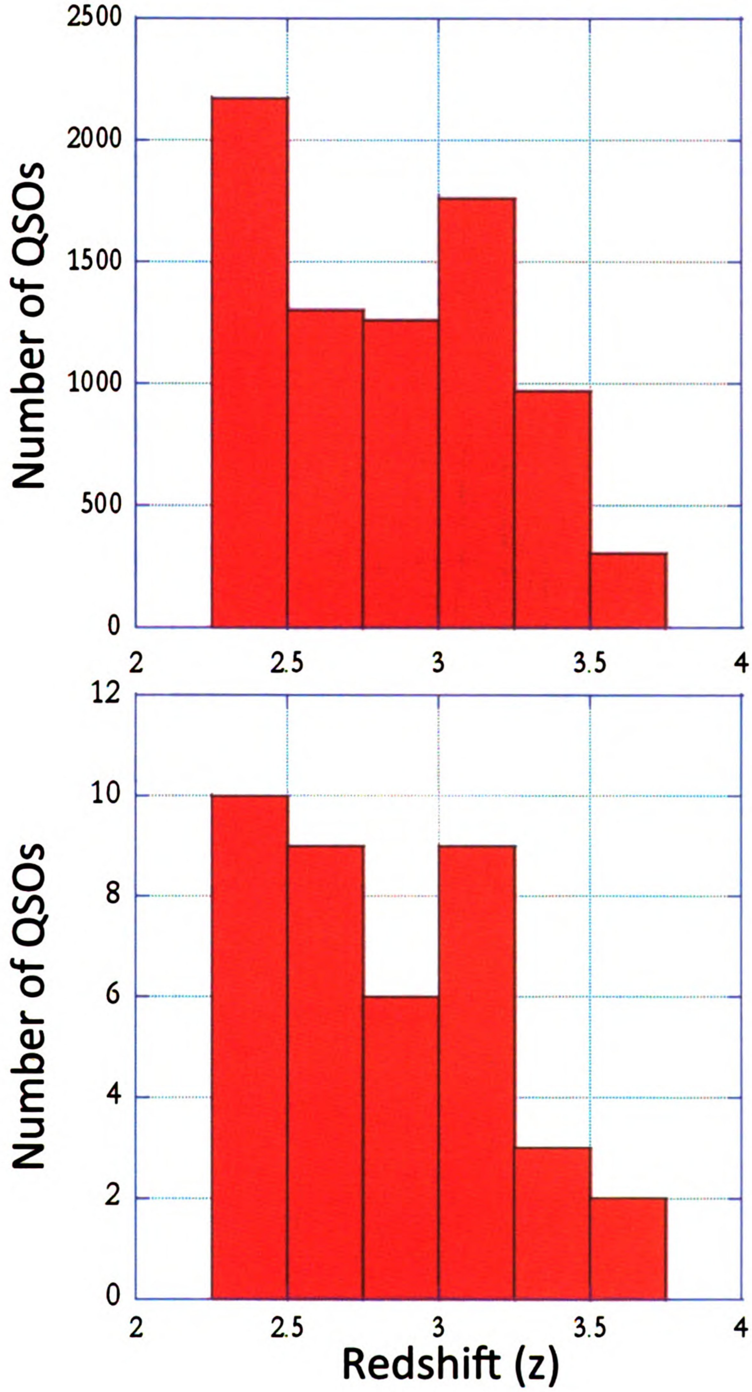

Figure A.8: Redshift (z) Distribution of the Intermediate Quasar Sample (top) and in the N-Loud Quasar Sample (bottom).

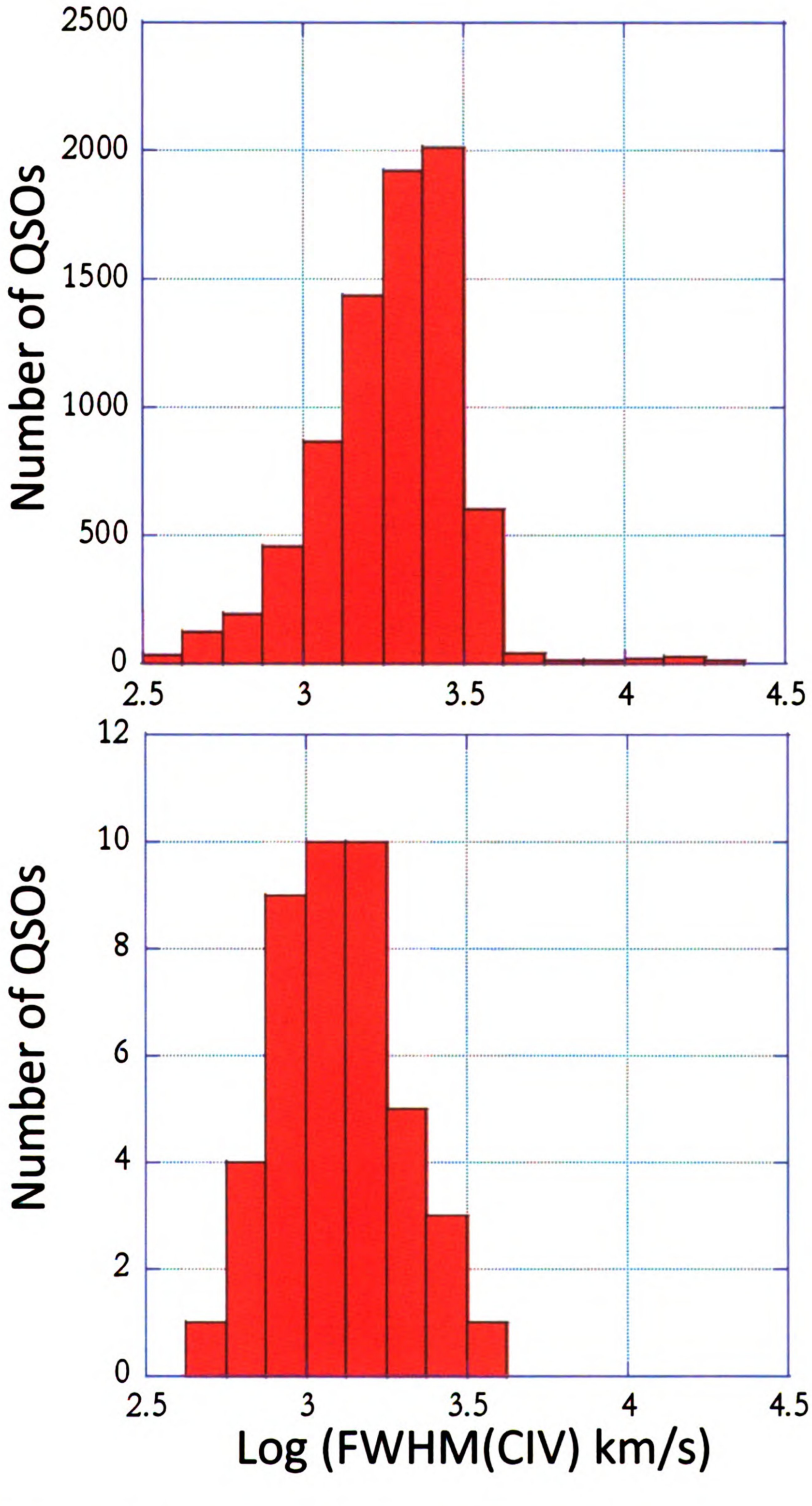

Figure A.9: Distribution of FWHM (CIV) in the Intermediate Quasar Sample (top) and N-Loud Quasar Sample (bottom).

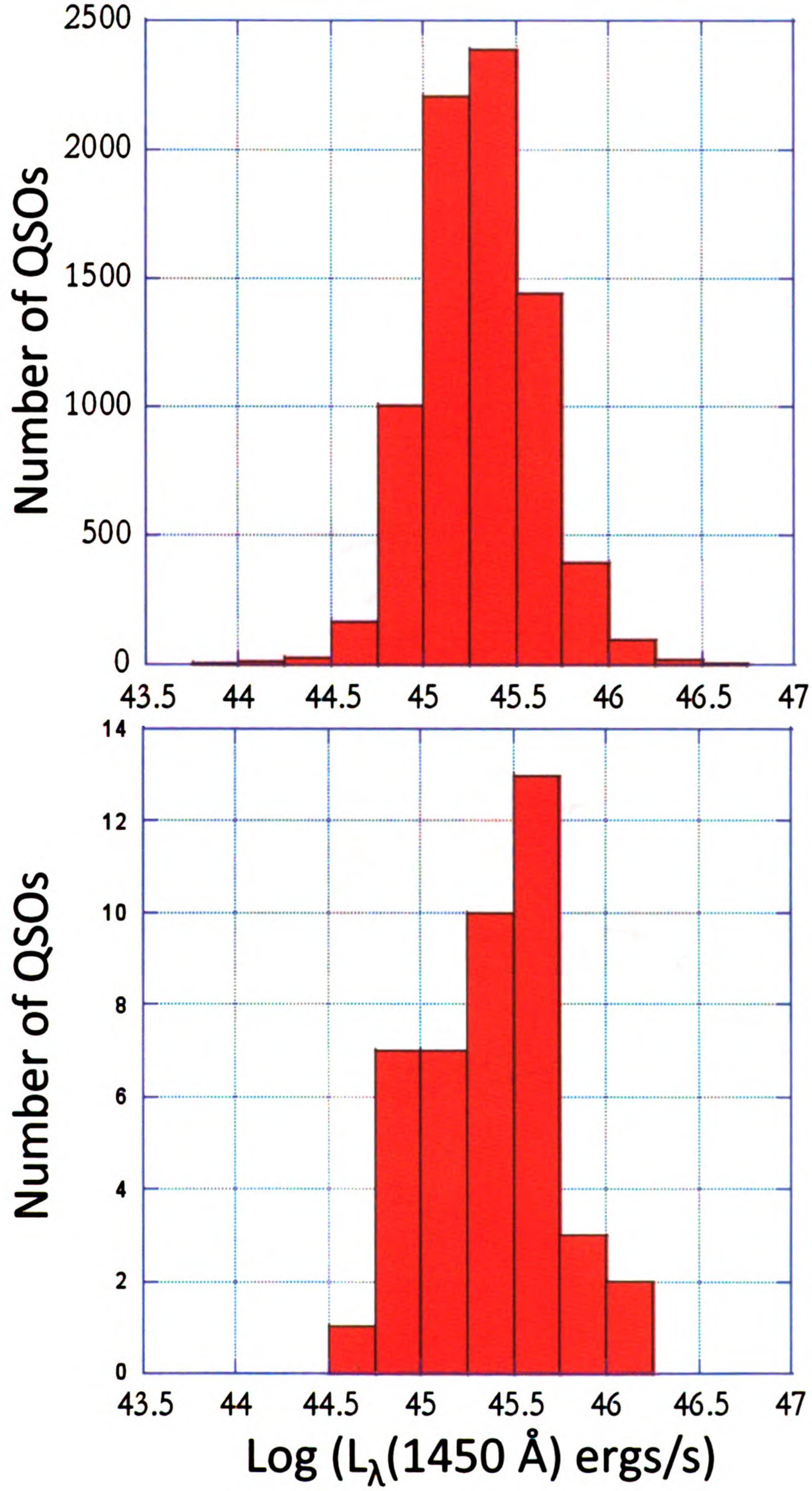

Figure A.10: Distribution of Continuum Luminosity in the Intermediate Quasar Sample (top) and in the N-Loud Quasar Sample (bottom).

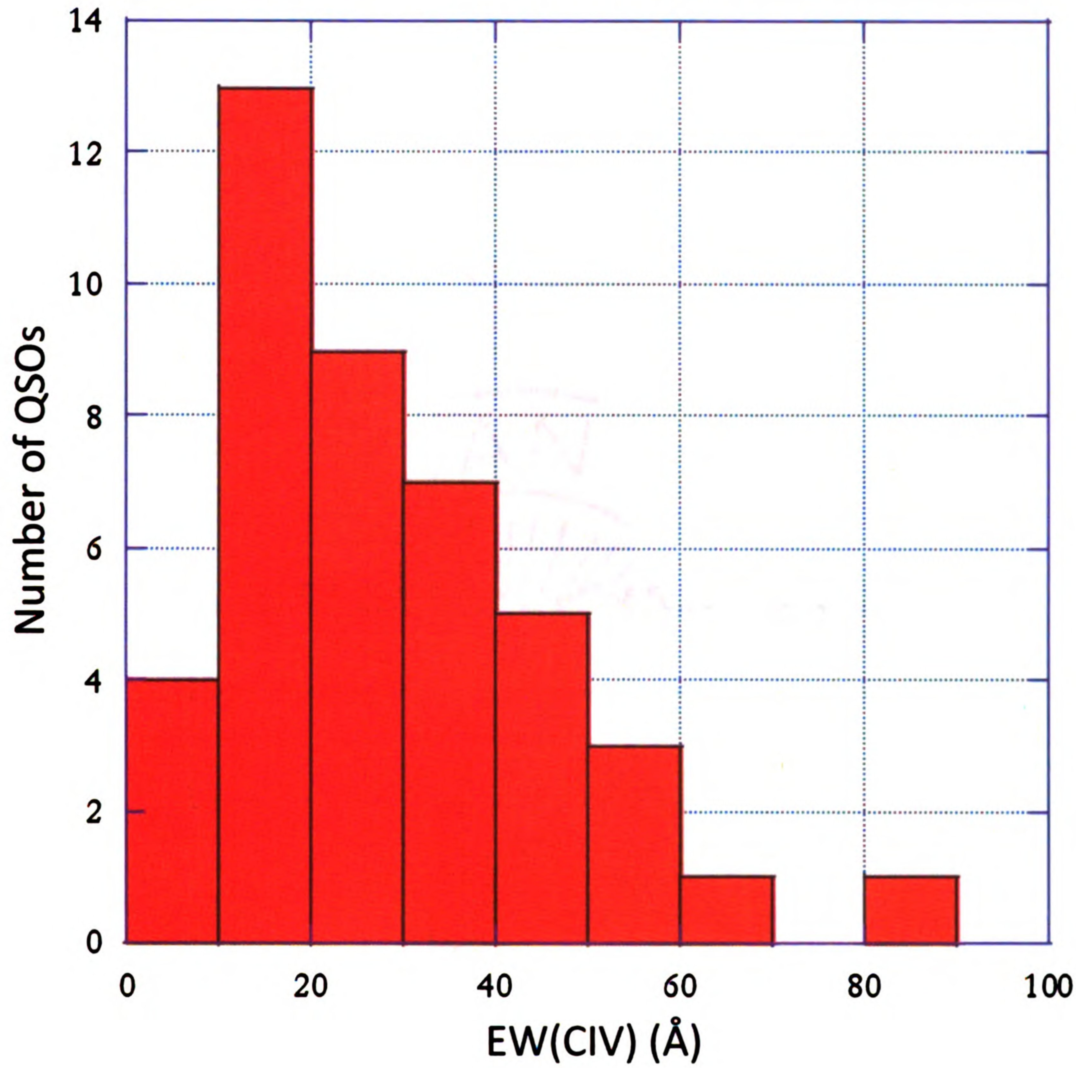

Figure A.11: Distribution of the Equivalent Width (EW) of the CIV Emission Line in the N-Loud Quasar Sample.

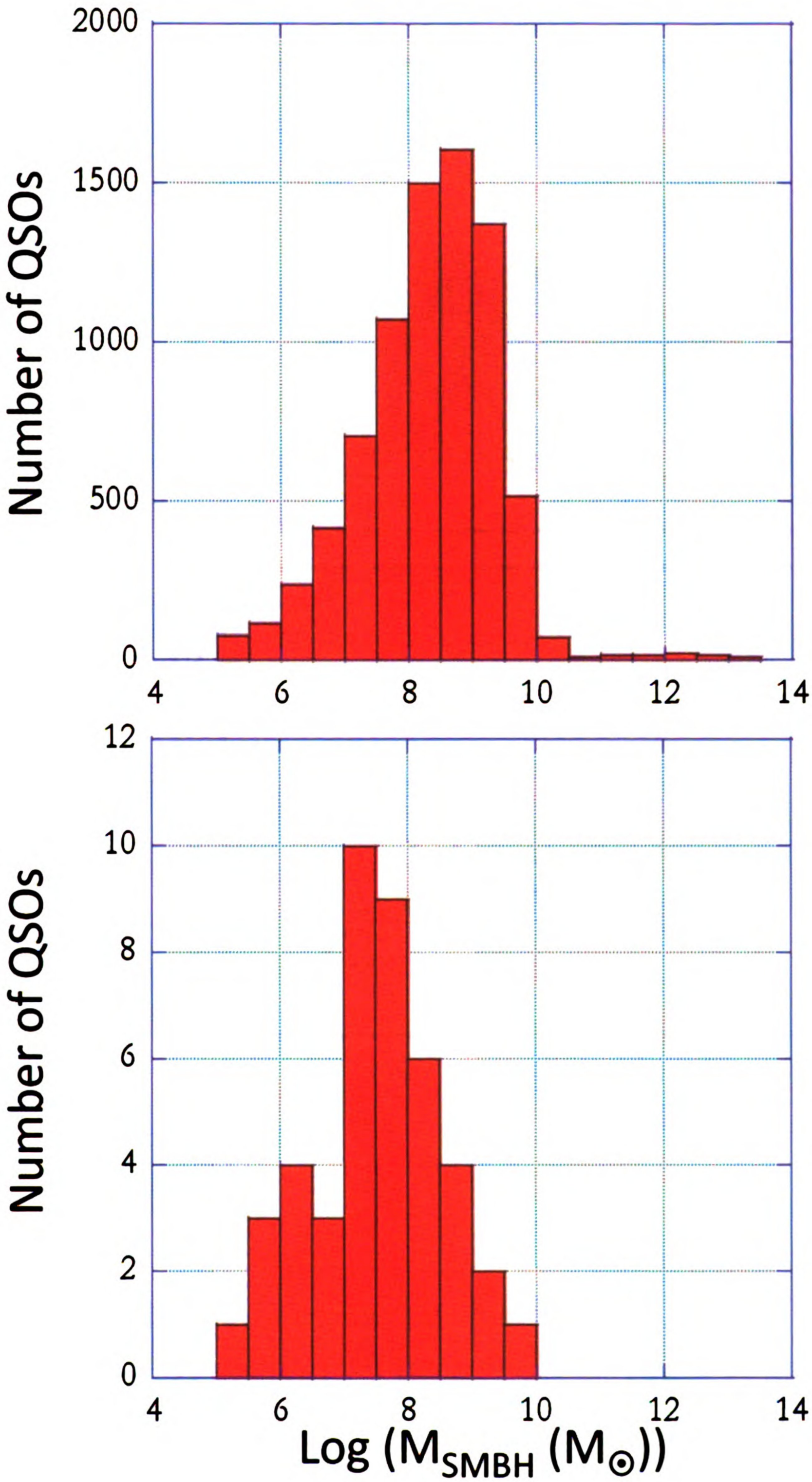

Figure A.12: Distribution of Supermassive Black Hole Mass (M_{SMBH}) for Intermediate Quasar Sample (top) and N-Loud Quasar Sample (bottom).

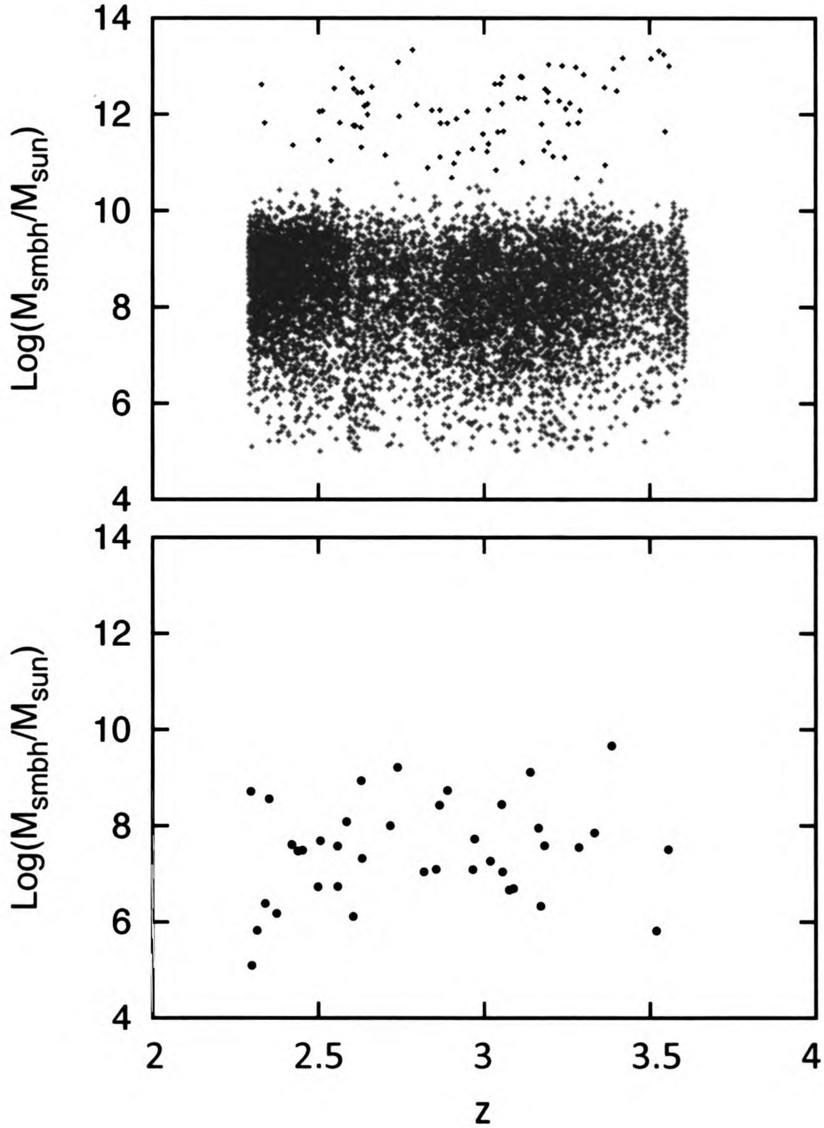

Figure A.13: Supermassive Black Hole Mass (M_{smbh}) as a function of redshift. The top figure shows the redshift distribution of M_{smbh} for the intermediate sample and the bottom figure shows the redshift distribution of M_{smbh} for N-Loud Quasars.

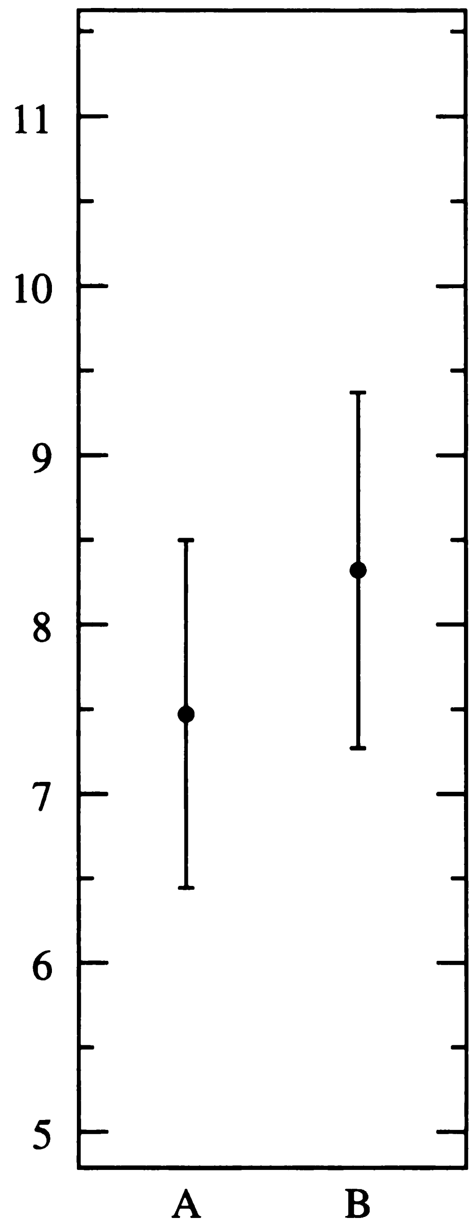

Figure A.14: Box Plot for the comparison of the M_{SMBH} for the two data sets. In the plot A refers to the N-Loud Sample set and B refers to the Intermediate Sample set. The dot indicates the mean M_{SMBH} and the error bars represent the standard deviation

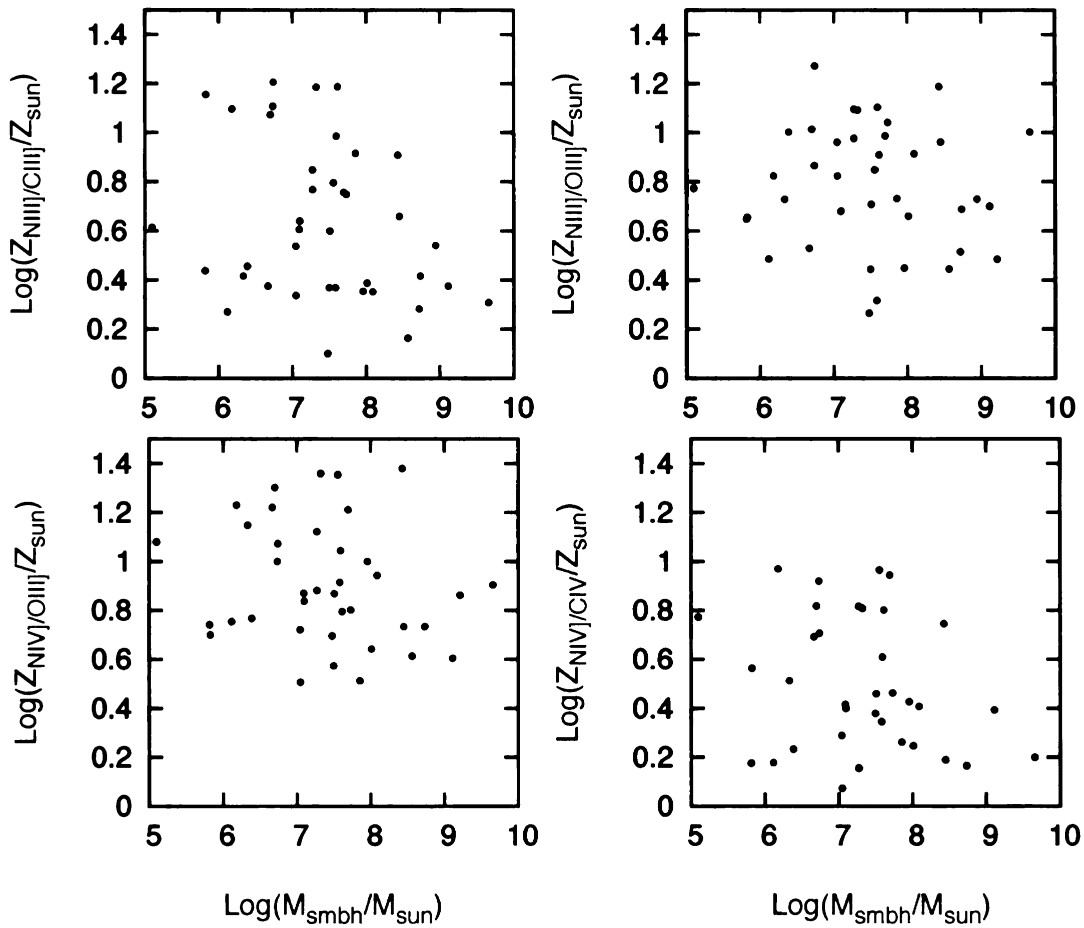

Figure A.15: Metallicity from individual line-intensity ratios as a function of Supermassive Black Hole Mass (M_{smbh}).

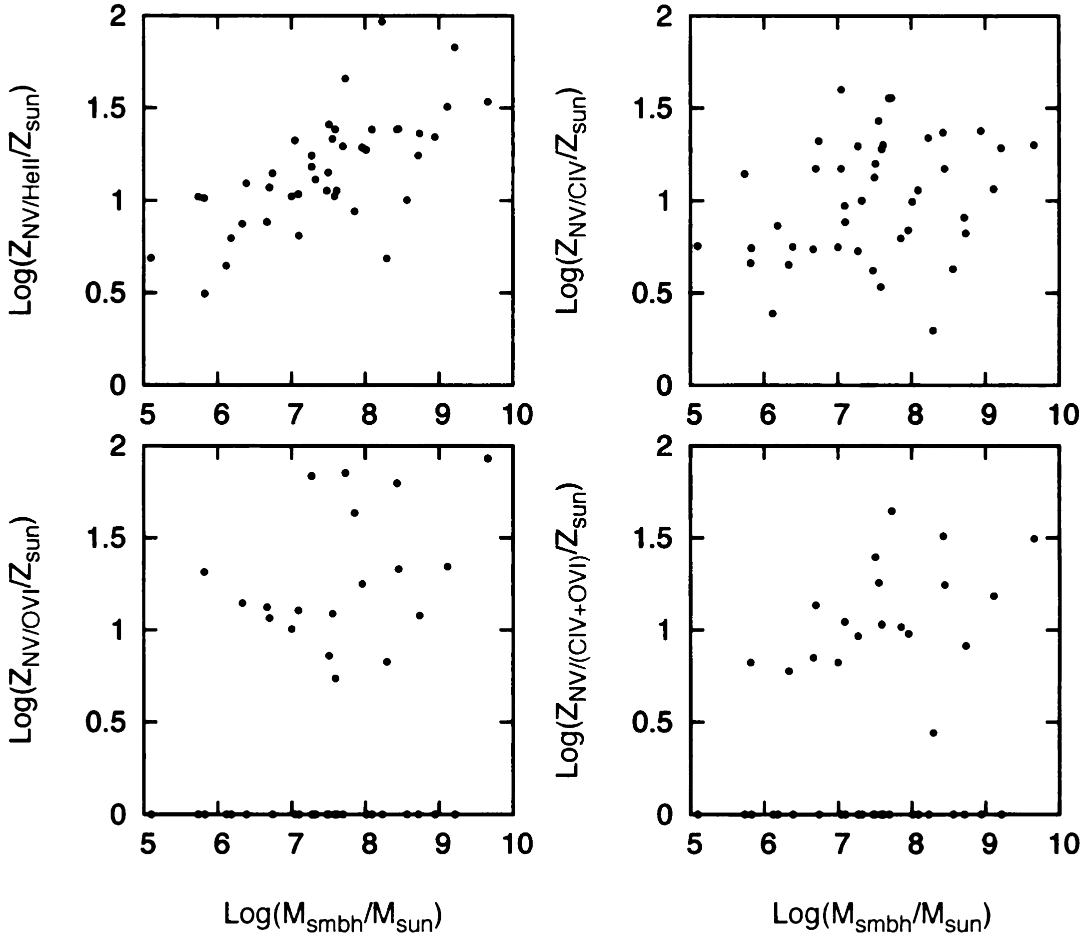

Figure A.15 *cont'd.*: Metallicity from individual line-intensity ratios as a function of Supermassive Black Hole Mass (M_{smbh}).

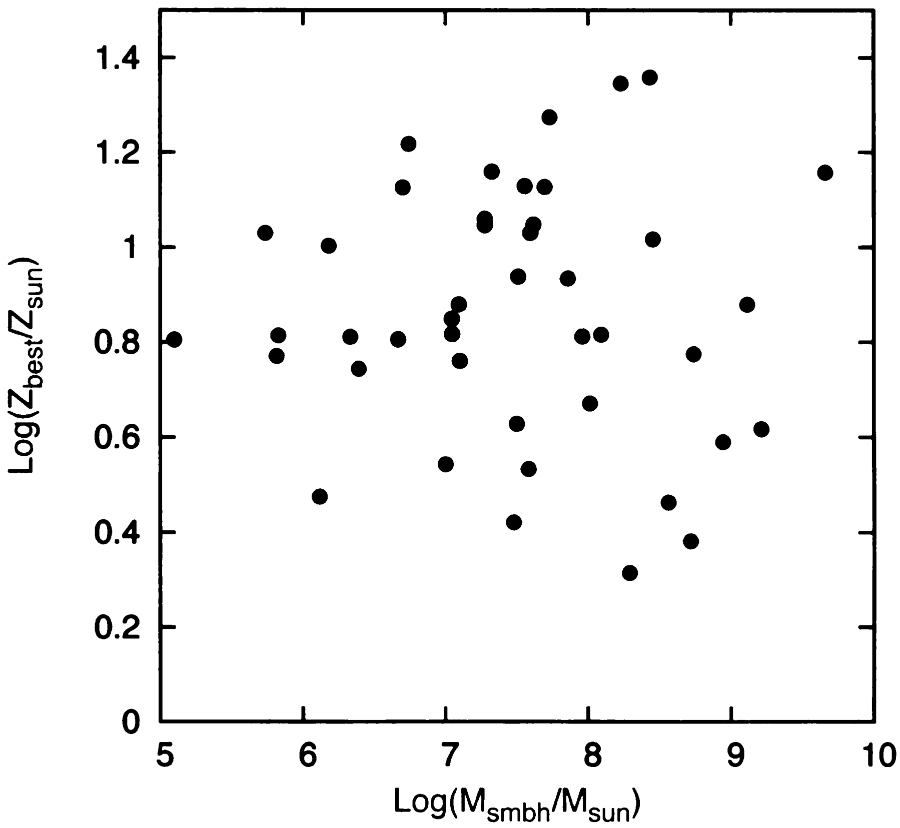

Figure A.16: Best Metallicity Estimate (Z_{best}) as a function of Supermassive Black Hole Mass (M_{smbh}).

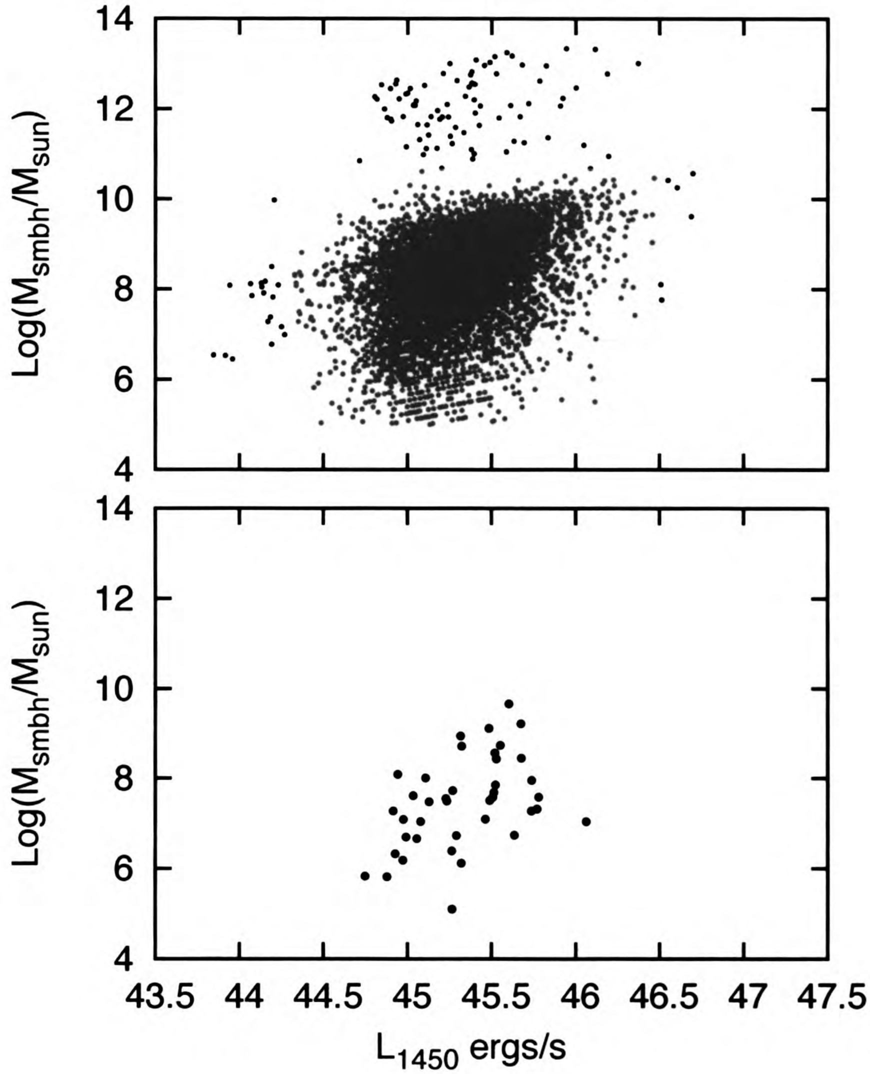

Figure A.17: Supermassive Black Hole Mass (M_{smbh}) as a function of Continuum Luminosity (L_{λ}(1450 Å)). The top figure shows the relation for the intermediate sample whereas the bottom figure shows for the N-Loud sample.

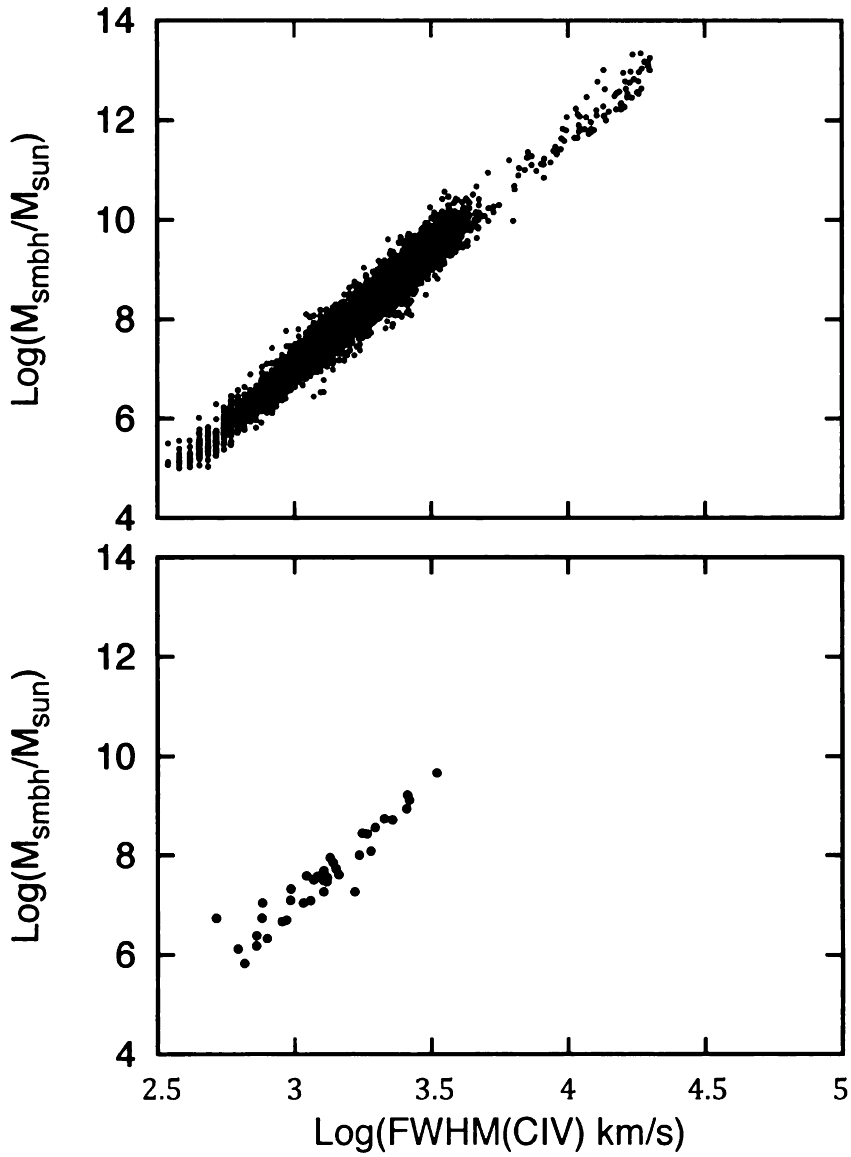

Figure A.18: Supermassive Black Hole Mass (M_{smbh}) as a function of FWHM (CIV). The top figure shows the relation for the intermediate sample whereas the bottom figure shows for the N loud sample.

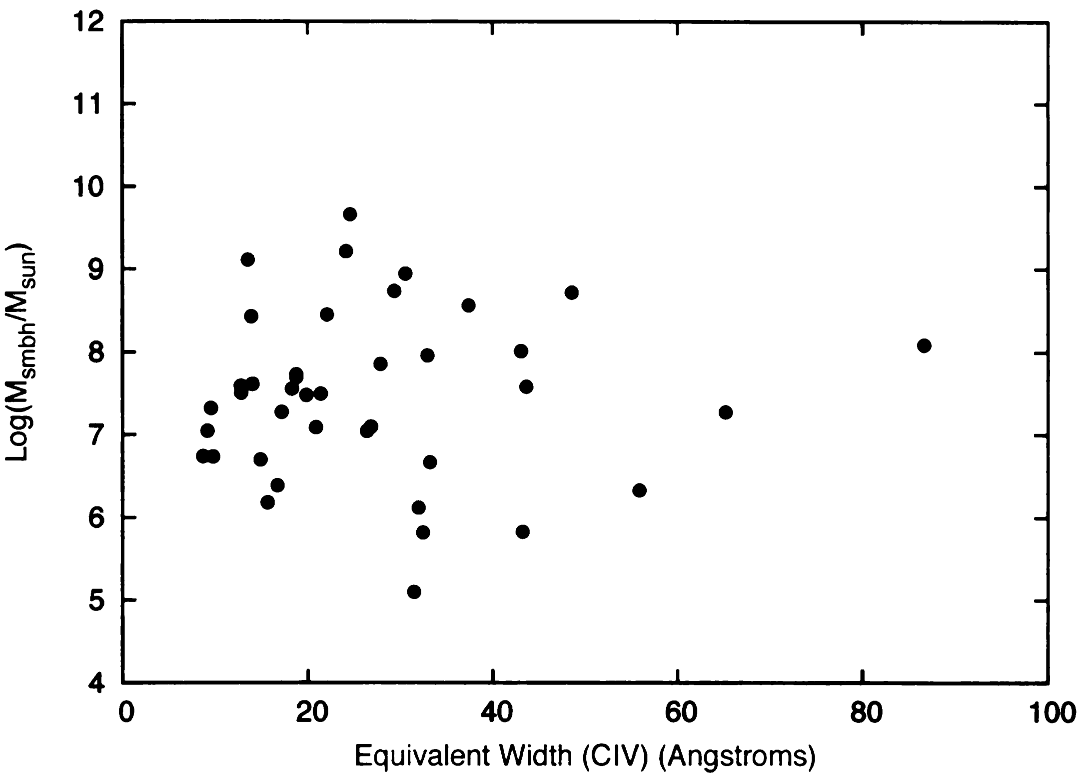

Figure A.19: Supermassive Black Hole Mass (M_{smbh}) as a function of CIV Equivalent width.

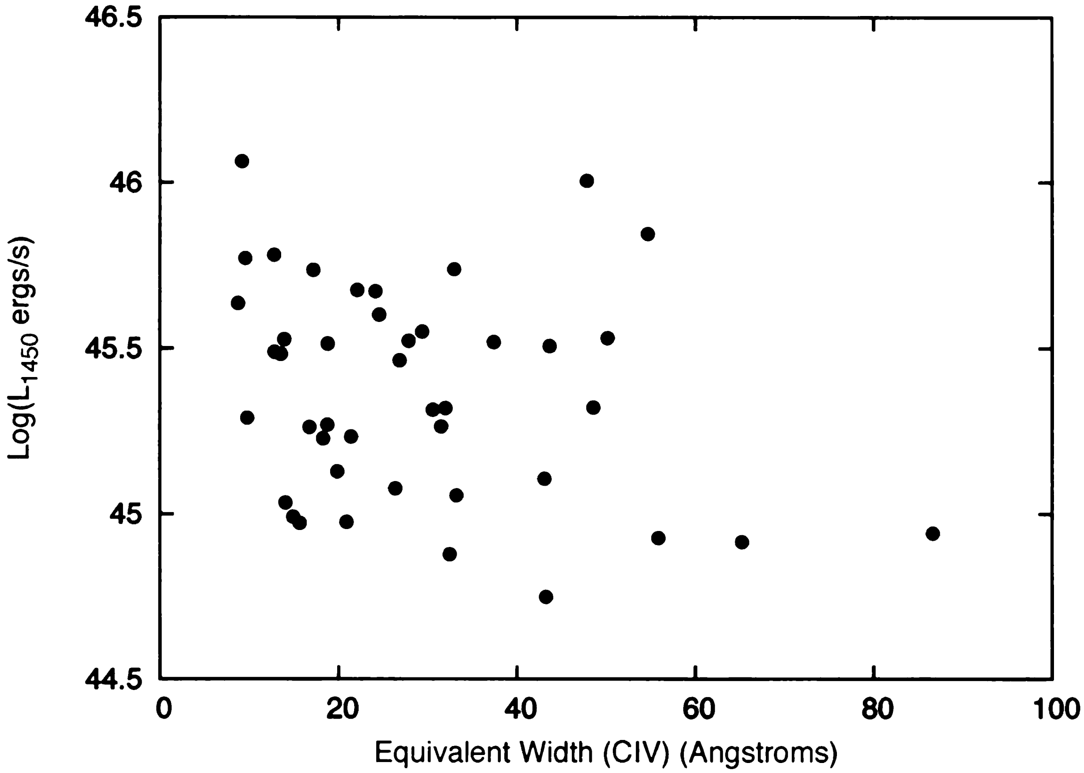

Figure A.20: Continuum Luminosity (L_λ(1450 Å) plotted as a function of CIV Equivalent width.

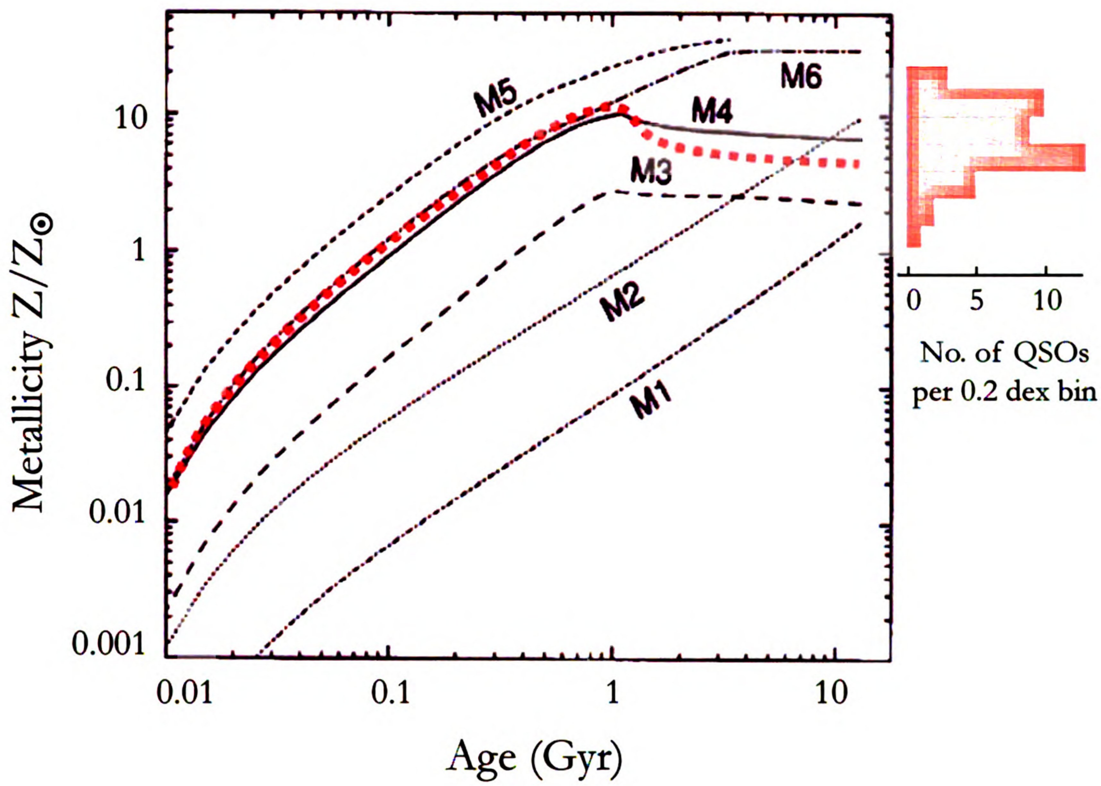

Figure A.21: Models of Chemical Evolution in Quasars (HF93) and the metallicity distribution in the N-Loud Quasar sample. The thick dotted line just above Model M4 refers to the Giant Elliptical model of Hamann and Ferland, (1999).

APPENDIX B: TABLES FOR THE QUASAR PROJECT

The following pages of the Appendix B contain the tables for the Quasar Project of this thesis. They appear in the order in which they have been mentioned in the text in the earlier Chapters.

Table B.1

Fe strengths for the N-Loud Quasars. Note that in all our tables we also include measurement results from N-Loud Quasar SDSS J125414.27+024117.5.

QSO Name	Fe strength
SDSS J003815.92+140304.5	0.57
SDSS J025505.93+001446.7	-
SDSS J074520.21+415725.4	0.40
SDSS J075326.12+403038.6	0.20
SDSS J080025.10+441723.1	0.20
SDSS J084715.16+383110.0	0.20
SDSS J085220.46+473458.4	0.00
SDSS J085522.87+375425.9	0.30
SDSS J093355.72+084043.0	0.40
SDSS J095027.35+123335.9	0.66
SDSS J095334.95+003724.3	0.14
SDSS J104229.19+381111.2	0.40
SDSS J104713.16+353115.6	0.00
SDSS J104713.39+095711.3	0.14
SDSS J105922.31+663806.2	-
SDSS J110013.68+030529.8	0.53
SDSS J112127.96+123816.1	0.76
SDSS J115631.40+133714.9	0.20
SDSS J115911.52+313427.3	1.80
SDSS J121913.19+043809.1	0.20

QSO Name	Fe strength
SDSS J122205.12+034310.3	0.33
SDSS J123450.00+375530.3	0.40
SDSS J124158.18+123059.3	-
SDSS J125414.27+024117.5	0.07
SDSS J130423.24+340438.1	0.04
SDSS J132827.07+581836.9	0.13
SDSS J133317.41+641718.0	0.54
SDSS J133923.77+632858.4	0.20
SDSS J135604.28+471058.7	0.10
SDSS J140432.99+072846.9	0.48
SDSS J142915.19+343820.3	0.30
SDSS J143048.84+481102.7	0.33
SDSS J144241.74+100533.9	0.60
SDSS J144805.84+440806.4	-
SDSS J145615.82+433954.3	0.20
SDSS J154534.59+511228.9	-
SDSS J155007.07+023607.6	0.29
SDSS J164148.19+223225.2	0.39
SDSS J165023.36+415142.0	0.20
SDSS J170704.87+644303.2	-
SDSS J171341.05+325045.3	0.30
SDSS J233101.64-010604.1	-
SDSS J233930.00+003017.3	0.69
SDSS J003815.92+140304.5	0.57

Table B.1 *cont'd.*

Table B.2

Template profiles used in deblending various emission lines. The templates were first extracted from the spectrum and then used for deblending. The different templates used were: CIV, He II, N IV] and OIII].

Name	Template			
	Lyα λ1215.67	N V λ1240	Si II λ1263	N IV] λ1486.50
SDSS J0038+1403	C IV	C IV	C IV	N IV
SDSS J0255+0014	C IV	C IV	C IV	N IV
SDSS J0745+4157	C IV	He II	C IV	N IV
SDSS J0753+4030	C IV	C IV	C IV	N IV
SDSS J0800+4417	C IV	C IV	C IV	N IV
SDSS J0847+3831	C IV	He II	N IV	N IV
SDSS J0852+4734	C IV	C IV	C IV	N IV
SDSS J0855+3754	C IV	C IV	C IV	N IV
SDSS J0933+0840	C IV	C IV	C IV	N IV
SDSS J0950+1233	C IV	C IV	C IV	N IV
SDSS J0953+0037	C III	C III	C III	N IV
SDSS J1042+3811	C IV	C IV	C IV	N IV
SDSS J1047+0957	C IV	C IV	C IV	N IV
SDSS J1047+3531	C IV	C IV	C IV	N IV
SDSS J1059+6638	C IV	He II	C IV	N IV
SDSS J1100+0305	C IV	C IV	C IV	N IV
SDSS J1121+1238	C IV	C IV	C IV	N IV
SDSS J1156+1337	C IV	C IV	C IV	N IV
SDSS J1159+3134	C IV	C IV	C IV	N IV
SDSS J1219+0438	C IV	C IV	C IV	N IV
SDSS J1222+0343	C IV	C IV	C IV	N IV

Name	Template			
	Lyα λ1215.67	**N V λ1240**	**Si II λ1263**	**N IV] λ1486.50**
SDSS J1234+3755	C IV	C IV	C IV	N IV
SDSS J1241+1230	C IV	C IV	C IV	N IV
SDSS J1254+0241	C IV	C IV	C IV	N IV
SDSS J1304+3404	C IV	He II	C IV	N IV
SDSS J1328+5818	C IV	C IV	C IV	N IV
SDSS J1333+6417	C IV	C IV	C IV	N IV
SDSS J1339+6328	C IV	C IV	C IV	N IV
SDSS J1356+4710	C IV	C IV	C IV	N IV
SDSS J1404+0728	C IV	N IV	C IV	N IV
SDSS J1429+3438	C IV	He II	C IV	N IV
SDSS J1430+4811	C IV	C IV	C IV	N IV
SDSS J1442+1005	He II	C IV	C IV	N IV
SDSS J1448+4408	C IV	He II	C IV	N IV
SDSS J1456+4339	C IV	C IV	C IV	N IV
SDSS J1545+5112	C IV	C IV	C IV	N IV
SDSS J1550+0236	C IV	C IV	C IV	N IV
SDSS J1641+2232	C IV	He II	C IV	N IV
SDSS J1650+4151	C III	He II	C III	N IV
SDSS J1707+6443	C IV	C IV	C IV	N IV
SDSS J1713+3250	C IV	C IV	C IV	N IV
SDSS J2331-0106	C IV	C IV	C IV	N IV
SDSS J2339+0030	C IV	C IV	C IV	N IV

Table B.2 *cont'd.*

<u>**Table B.2 *cont'd.***</u>

Template profiles used in deblending various emission lines.

Name	Template			
	C IV λ1549	**He II λ1640.72**	**O III] λ1665**	**N III] λ1750**
SDSS J0038+1403	C IV	He II	He II	N III
SDSS J0255+0014	C IV	He II	N IV	N III
SDSS J0745+4157	C IV	He II	N IV	C IV
SDSS J0753+4030	C IV	He II	O III	C IV + He II
SDSS J0800+4417	C IV	He II	N IV	N III
SDSS J0847+3831	C IV	He II	N IV	N IV + He II
SDSS J0852+4734	C IV	He II	N IV	N III
SDSS J0855+3754	C IV	He II	O I	C IV
SDSS J0933+0840	C IV	He II	O I	N III
SDSS J0950+1233	C IV	He II	N IV	N IV
SDSS J0953+0037	C III	He II	N IV	C III
SDSS J1042+3811	C IV	He II	N IV	C IV
SDSS J1047+0957	C IV	He II	N IV	N III
SDSS J1047+3531	C IV	He II	N IV	N IV
SDSS J1059+6638	C IV	He II	C IV	N III
SDSS J1100+0305	C IV	He II	N IV	He II
SDSS J1121+1238	C IV	He II	N IV	N III
SDSS J1156+1337	C IV	He II	N IV	C IV + He II
SDSS J1159+3134	C IV	He II	He II	He II
SDSS J1219+0438	C IV	He II	N IV	N IV
SDSS J1222+0343	C IV	He II	O I	O I
SDSS J1234+3755	C IV	He II	C IV	O I
SDSS J1241+1230	C IV	He II	He II	O I

Name	Template			
	C IV λ1549	**He II λ1640.72**	**O III] λ1665**	**N III] λ1750**
SDSS J1254+0241	C IV	He II	N IV	He II
SDSS J1304+3404	C IV	He II	N IV	N III
SDSS J1328+5818	C IV	He II	C IV	C IV
SDSS J1333+6417	C IV	He II	N IV	N IV
SDSS J1339+6328	C IV	He II	N IV	N IV
SDSS J1356+4710	C IV	He II	He II	C IV
SDSS J1404+0728	C IV	He II	N IV	C IV, N IV, He II
SDSS J1429+3438	C IV	He II	C IV	C IV
SDSS J1430+4811	C IV	He II	C IV	N IV
SDSS J1442+1005	C IV	He II	C IV	N IV
SDSS J1448+4408	C IV	He II	C IV	He II
SDSS J1456+4339	C IV	He II	N IV	C IV
SDSS J1545+5112	C IV	He II	N IV	C IV
SDSS J1550+0236	C IV	He II	N IV	N IV
SDSS J1641+2232	C IV	He II	C IV	C IV
SDSS J1650+4151	C III	He II	C III	C III
SDSS J1707+6443	C IV	He II	He II	He II
SDSS J1713+3250	C IV	He II	C IV	N IV
SDSS J2331-0106	C IV	He II	C IV	N IV
SDSS J2339+0030	C IV	He II	C IV	C IV

Table B.2 *cont'd.*

Table B.2 *cont'd.*

Template profiles used in deblending various emission lines.

Name	Template			
	Al III λ1857	Si III] λ1892.03	C III] λ1908.73	Fe blend λ1895,1915,1926
SDSS J0038+1403	-	C IV	C IV	C IV
SDSS J0255+0014	N IV	He II	C IV	C IV
SDSS J0745+4157	N IV	He II	C IV	C IV
SDSS J0753+4030	C IV	C IV	C IV	C IV
SDSS J0800+4417	C IV	C IV	C IV	C IV
SDSS J0847+3831	N IV	N IV	C IV	N IV
SDSS J0852+4734	C IV	C IV	C IV	C IV
SDSS J0855+3754	C IV	C IV	C IV	C IV
SDSS J0933+0840	C IV	C IV	C IV	C IV
SDSS J0950+1233	C IV	C IV	C IV	C IV
SDSS J0953+0037	N IV	C III	C III	C III
SDSS J1042+3811	N IV	He II	C IV	C IV
SDSS J1047+0957	N IV	N IV	N IV	C IV
SDSS J1047+3531	N IV	N IV	C IV	-
SDSS J1059+6638	N IV	He II	C IV	C IV
SDSS J1100+0305	He II	N IV	C IV	C IV
SDSS J1121+1238	He II	N IV	N IV	N IV
SDSS J1156+1337	C IV	N IV	C IV	-
SDSS J1159+3134	N IV	C III	C III	N IV
SDSS J1219+0438	C IV	C IV	C IV	C IV
SDSS J1222+0343	C IV	C IV	C IV	C IV
SDSS J1234+3755	C IV	C IV	C IV	C IV

Name	Template			
	Al III λ1857	Si III] λ1892.03	C III] λ1908.73	Fe blend λ1895,1915,1926
SDSS J1241+1230	C IV	O I	C IV	C IV
SDSS J1254+0241	C IV	N IV	C IV	C IV
SDSS J1304+3404	N IV	N IV	C IV	C IV
SDSS J1328+5818	C IV	N IV	C IV	C IV
SDSS J1333+6417	He II	He II	C IV	C IV
SDSS J1339+6328	N IV	N IV	C IV	C IV + He II
SDSS J1356+4710	N IV	C IV	C IV	C IV
SDSS J1404+0728	N IV	N IV	C IV	C IV
SDSS J1429+3438	O I	C IV	C IV	C IV
SDSS J1430+4811	C IV	He II	He II	-
SDSS J1442+1005	N IV	C IV	C IV	C IV
SDSS J1448+4408	N IV	C IV	C IV	C IV
SDSS J1456+4339	C IV	N IV	C IV	C IV
SDSS J1545+5112	C IV	He II	C IV	C IV
SDSS J1550+0236	C IV	N IV	C IV	C IV
SDSS J1641+2232	C IV	C IV	C IV	C IV
SDSS J1650+4151	C III	C III	C III	C III
SDSS J1707+6443	C IV	He II	C IV	C IV
SDSS J1713+3250	C IV	He II	O III	He II
SDSS J2331-0106	C IV	N IV	C IV	C IV
SDSS J2339+0030	He II	C IV	C IV	C IV

Table B.2 *cont'd.*

Table B.3

Emission line-flux strengths for NV, NIV] and NIII] in the units of CIV line-flux.

Name	NV			NIV]			NIII]		
SDSS	Best	min	max	Best	min	max	Best	min	max
J0038+1403	0.95	0.81	1.04	0.06	0.03	0.09	0.15	0.10	0.20
J0255+0014	0.57	0.47	0.66	0.20	0.16	0.23	0.25	0.24	0.27
J0745+4157	0.75	0.67	0.86	0.08	0.07	0.15	0.15	0.13	0.20
J0753+4030	0.24	0.17	0.45	0.02	0.01	0.03	0.02	0.01	0.02
J0800+4417	1.30	1.51	1.51	0.09	0.09	0.14	0.16	0.17	0.17
J0847+3831	1.46	1.23	1.79	0.13	0.11	0.16	0.32	0.27	0.40
J0852+4734	1.52	1.55	1.54	0.22	0.23	0.34	0.71	0.78	0.84
J0855+3754	0.79	0.61	1.00	0.02	0.01	0.03	0.06	0.05	0.09
J0933+0840	1.71	1.12	1.97	0.03	0.02	0.03	0.18	0.15	0.22
J0950+1233	1.25	1.20	1.29	0.23	0.23	0.27	0.31	0.29	0.43
J0953+0037	0.28	0.24	0.27	0.05	0.03	0.07	0.07	0.07	0.08
J1042+3811	0.95	0.67	1.24	0.23	0.23	0.24	0.30	0.31	0.32
J1047+0957	0.44	0.35	0.53	0.03	0.03	0.05	0.03	0.03	0.03
J1047+3531	1.61	1.34	1.56	0.11	0.10	0.12	0.47	0.40	0.46
J1059+6638	0.55	0.52	0.60	0.16	0.13	0.16	0.09	0.08	0.09
J1100+0305	0.56	0.51	0.82	0.12	0.11	0.14	0.28	0.21	0.33
J1121+1238	0.54	0.40	0.71	0.05	0.04	0.06	0.17	0.17	0.20
J1156+1337	0.63	0.43	0.76	0.06	0.06	0.06	0.22	0.19	0.23
J1159+3134	2.40	2.23	2.54	0.04	0.04	0.04	0.18	0.17	0.19
J1219+0438	1.48	0.98	1.79	0.03	0.03	0.03	0.03	0.02	0.05
J1222+0343	1.04	0.98	1.18	0.08	0.07	0.10	0.18	0.17	0.21
J1234+3755	1.05	0.89	1.22	0.08	0.08	0.15	0.24	0.22	0.27
J1241+1230	1.75	1.70	1.93	0.10	0.09	0.16	0.38	0.32	0.45
J1254+0241	1.50	1.44	1.44	0.23	0.23	0.25	0.40	0.37	0.39
J1304+3404	1.57	1.19	1.71	0.16	0.17	0.17	0.48	0.45	0.47
J1328+5818	0.57	0.43	0.68	0.04	0.03	0.04	0.05	0.05	0.05
J1333+6417	1.25	1.04	1.63	0.06	0.05	0.07	0.28	0.25	0.30
J1339+6328	0.37	0.30	0.45	0.07	0.07	0.08	0.04	0.04	0.05
J1356+4710	1.52	0.94	1.90	0.05	0.03	0.06	0.16	0.10	0.20

Name	NV			NIV]			NIII]		
SDSS	Best	min	max	Best	min	max	Best	min	max
J1404+0728	1.68	1.23	2.05	0.18	0.19	0.21	0.28	0.29	0.28
J1429+3438	0.45	0.35	0.86	0.03	0.02	0.04	0.05	0.04	0.07
J1430+4811	1.19	1.11	1.42	0.32	0.28	0.37	0.56	0.50	0.72
J1442+1005	0.66	0.48	0.83	0.05	0.04	0.07	0.12	0.09	0.12
J1448+4408	1.85	1.76	2.40	0.37	0.34	0.41	0.32	0.26	0.41
J1456+4339	0.47	0.45	0.43	0.10	0.09	0.11	0.10	0.09	0.11
J1545+5112	1.16	1.15	1.15	0.08	0.07	0.09	0.13	0.13	0.14
J1550+0236	0.72	0.73	0.78	0.38	0.40	0.45	0.39	0.44	0.40
J1641+2232	1.95	1.63	2.28	0.35	0.34	0.38	0.53	0.51	0.68
J1650+4151	0.57	0.46	0.80	0.06	0.05	0.12	0.24	0.21	0.26
J1707+6443	0.69	0.52	0.79	0.09	0.06	0.09	0.06	0.05	0.07
J1713+3250	0.90	0.64	1.16	0.08	0.06	0.10	0.14	0.13	0.14
J2331-0106	0.48	0.37	0.68	0.05	0.05	0.05	0.10	0.09	0.12
J2339+0030	1.25	1.25	1.34	0.05	0.05	0.06	0.22	0.21	0.23

Table B.3 *cont'd.*

Table B.3 *cont'd.*

Emission line-flux strengths for CIII], He II and OIII] in the units of CIV line-flux.

Name	CIII]			HeII			OIII]		
SDSS	Best	min	max	Best	min	max	Best	min	max
J0038+1403	0.39	0.34	0.42	0.12	0.11	0.13	0.12	0.09	0.15
J0255+0014	0.37	0.32	0.43	0.19	0.18	0.20	0.15	0.12	0.16
J0745+4157	0.21	0.16	0.25	0.21	0.20	0.23	0.11	0.09	0.11
J0753+4030	0.13	0.08	0.19	0.08	0.07	0.08	0.05	0.05	0.06
J0800+4417	0.25	0.30	0.34	0.12	0.15	0.13	0.11	0.14	0.12
J0847+3831	0.29	0.27	0.35	0.15	0.14	0.15	0.10	0.10	0.15
J0852+4734	0.44	0.35	0.53	0.30	0.32	0.35	0.33	0.26	0.38
J0855+3754	0.21	0.15	0.25	0.11	0.09	0.12	0.07	0.06	0.08
J0933+0840	0.33	0.23	0.42	0.19	0.17	0.20	0.12	0.10	0.14
J0950+1233	0.24	0.15	0.32	0.24	0.25	0.24	0.12	0.12	0.14
J0953+0037	0.24	0.19	0.27	0.10	0.08	0.12	0.08	0.06	0.10
J1042+3811	0.19	0.14	0.23	0.17	0.18	0.18	0.10	0.11	0.13
J1047+0957	0.17	0.13	0.22	0.09	0.06	0.10	0.07	0.06	0.07
J1047+3531	0.22	0.18	0.24	0.05	0.05	0.05	0.08	0.06	0.09
J1059+6638	0.22	0.18	0.27	0.14	0.14	0.14	0.09	0.09	0.10
J1100+0305	0.19	0.12	0.42	0.28	0.26	0.27	0.22	0.17	0.26
J1121+1238	0.20	0.14	0.27	0.07	0.06	0.09	0.06	0.05	0.07
J1156+1337	0.21	0.17	0.24	0.15	0.15	0.15	0.15	0.14	0.15
J1159+3134	0.53	0.46	0.59	0.06	0.06	0.05	0.10	0.09	0.11
J1219+0438	0.35	0.27	0.43	0.06	0.05	0.07	0.04	0.04	0.05
J1222+0343	0.51	0.32	0.63	0.11	0.08	0.13	0.08	0.07	0.11
J1234+3755	0.64	0.45	0.87	0.08	0.07	0.09	0.17	0.13	0.21
J1241+1230	0.41	0.35	0.48	0.14	0.14	0.17	0.15	0.15	0.18
J1254+0241	0.42	0.42	0.42	0.23	0.16	0.21	0.16	0.13	0.15
J1304+3404	0.29	0.28	0.27	0.26	0.25	0.24	0.12	0.12	0.12
J1328+5818	0.27	0.23	0.32	0.12	0.12	0.13	0.12	0.11	0.12
J1333+6417	0.50	0.45	0.52	0.14	0.14	0.14	0.11	0.09	0.13
J1339+6328	0.12	0.07	0.19	0.08	0.08	0.09	0.08	0.07	0.09

Name SDSS	CIII] Best	CIII] min	CIII] max	HeII Best	HeII min	HeII max	OIII] Best	OIII] min	OIII] max
J1356+4710	0.48	0.35	0.73	0.11	0.10	0.12	0.06	0.03	0.09
J1404+0728	0.27	0.16	0.33	0.17	0.16	0.17	0.08	0.08	0.09
J1429+3438	0.23	0.17	0.30	0.10	0.09	0.12	0.07	0.05	0.08
J1430+4811	0.41	0.30	0.46	0.26	0.26	0.34	0.28	0.25	0.32
J1442+1005	0.28	0.25	0.34	0.07	0.05	0.09	0.09	0.09	0.13
J1448+4408	0.36	0.31	0.41	0.21	0.20	0.22	0.17	0.18	0.18
J1456+4339	0.25	0.17	0.28	0.12	0.12	0.12	0.07	0.05	0.09
J1545+5112	0.35	0.30	0.46	0.19	0.21	0.18	0.17	0.19	0.17
J1550+0236	0.29	0.23	0.35	0.21	0.21	0.26	0.22	0.25	0.22
J1641+2232	0.53	0.38	0.61	0.31	0.28	0.32	0.26	0.25	0.26
J1650+4151	0.52	0.38	0.50	0.11	0.11	0.13	0.09	0.08	0.12
J1707+6443	0.16	0.12	0.21	0.09	0.07	0.11	0.08	0.06	0.08
J1713+3250	0.21	0.11	0.31	0.19	0.18	0.20	0.10	0.09	0.12
J2331-0106	0.25	0.19	0.23	0.10	0.10	0.10	0.09	0.08	0.08
J2339+0030	0.30	0.22	0.44	0.13	0.12	0.15	0.09	0.08	0.11

Table B.3 *cont'd.*

Table B.3 *cont'd.*

Emission line-flux strengths for OVI in the units of CIV line-flux.

Name	OVI Best	OVI min	OVI max
J0038+1403	-	-	-
J0255+0014	-	-	-
J0745+4157	0.654	0.587	0.722
J0753+4030	0.248	0.231	0.290
J0800+4417	-	-	-
J0847+3831	1.715	1.554	1.825
J0852+4734	-	-	-
J0855+3754	-	-	-
J0933+0840	-	-	-
J0950+1233	0.937	0.879	0.992
J0953+0037	-	-	-
J1042+3811	-	-	-
J1047+0957	-	-	-
J1047+3531	-	-	-
J1059+6638	0.378	0.378	0.382
J1100+0305	-	-	-
J1121+1238	0.117	0.109	0.127
J1156+1337	0.187	0.109	0.193
J1159+3134	-	-	-
J1219+0438	-	-	-
J1222+0343	-	-	-
J1234+3755	0.504	0.457	0.570
J1241+1230	0.470	0.446	0.605
J1254+0241	-	-	-
J1304+3404	-	-	-
J1328+5818	0.468	0.445	0.493
J1333+6417	-	-	-
J1339+6328	-	-	-

Name	OVI		
	Best	min	max
J1356+4710	0.281	0.250	0.330
J1404+0728	0.386	0.320	0.402
J1429+3438	-	-	-
J1430+4811	-	-	-
J1442+1005	0.486	0.478	0.464
J1448+4408	1.336	1.380	1.353
J1456+4339	0.309	0.274	0.310
J1545+5112	-	-	-
J1550+0236	-	-	-
J1641+2232	-	-	-
J1650+4151	-	-	-
J1707+6443	0.381	0.356	0.382
J1713+3250	0.632	0.531	0.892
J2331-0106	0.230	0.219	0.240
J2339+0030	0.608	0.574	0.711

Table B.3 *cont'd.*

Table B.4

Best measurements of line-intensity ratios for NIII]/CIII] and NIII]/OIII] along with their corresponding minimum and maximum values.

Name	NIII/CIII]			NIII]/OIII]		
SDSS	Best	min	max	Best	min	max
J0038+1403	-0.410	-0.647	-0.209	0.109	-0.186	0.377
J0255+0014	-0.178	-0.327	-0.015	0.217	0.110	0.398
J0745+4157	-0.150	-0.272	0.096	0.131	0.068	0.361
J0753+4030	-0.927	-1.116	-0.561	-0.530	-0.625	-0.354
J0800+4417	-0.192	-0.489	-0.061	0.157	-0.047	0.277
J0847+3831	0.043	-0.110	0.175	0.485	0.250	0.591
J0852+4734	0.206	0.027	0.531	0.338	0.168	0.654
J0855+3754	-0.522	-0.708	-0.198	-0.044	-0.182	0.180
J0933+0840	-0.253	-0.499	0.021	0.177	-0.033	0.365
J0950+1233	0.110	-0.086	0.485	0.429	0.290	0.601
J0953+0037	-0.537	-0.708	-0.298	-0.075	-0.287	0.206
J1042+3811	0.204	0.094	0.386	0.478	0.344	0.514
J1047+0957	-0.747	-0.933	-0.554	-0.320	-0.411	-0.201
J1047+3531	0.322	0.170	0.463	0.792	0.581	0.951
J1059+6638	-0.422	-0.590	-0.256	-0.028	-0.161	0.073
J1100+0305	0.180	-0.320	0.460	0.104	-0.114	0.320
J1121+1238	-0.058	-0.227	0.181	0.480	0.358	0.672
J1156+1337	0.011	-0.140	0.172	0.179	0.070	0.247
J1159+3134	-0.462	-0.635	-0.278	0.262	0.102	0.425
J1219+0438	-1.025	-1.339	-0.670	-0.076	-0.362	0.190
J1222+0343	-0.447	-0.598	-0.148	0.342	0.165	0.485
J1234+3755	-0.422	-0.622	-0.200	0.151	-0.003	0.356
J1241+1230	-0.067	-0.230	0.171	0.446	0.351	0.634
J1254+0241	-0.021	-0.094	0.000	0.398	0.364	0.509
J1304+3404	0.222	0.068	0.370	0.592	0.438	0.743
J1328+5818	-0.748	-0.858	-0.619	-0.371	-0.431	-0.298

Name	NIII/CIII]			NIII]/OIII]		
SDSS	Best	min	max	Best	min	max
J1333+6417	-0.256	-0.374	-0.112	0.385	0.217	0.605
J1339+6328	-0.429	-0.683	-0.174	-0.253	-0.345	-0.167
J1356+4710	-0.491	-0.879	-0.212	0.421	0.053	0.811
J1404+0728	0.007	-0.110	0.290	0.539	0.464	0.613
J1429+3438	-0.669	-0.859	-0.353	-0.118	-0.261	0.169
J1430+4811	0.139	0.033	0.389	0.299	0.190	0.466
J1442+1005	-0.380	-0.667	-0.260	0.139	-0.245	0.217
J1448+4408	-0.045	-0.315	0.228	0.283	0.037	0.477
J1456+4339	-0.380	-0.572	-0.156	0.176	-0.069	0.352
J1545+5112	-0.429	-0.682	-0.204	-0.119	-0.237	-0.010
J1550+0236	0.130	-0.032	0.377	0.262	0.175	0.333
J1641+2232	-0.063	-0.158	0.145	0.407	0.363	0.600
J1650+4151	-0.339	-0.492	-0.061	0.421	0.137	0.645
J1707+6443	-0.444	-0.700	-0.177	-0.114	-0.299	0.111
J1713+3250	-0.186	-0.389	0.100	0.128	0.037	0.186
J2331-0106	-0.358	-0.450	-0.124	0.097	-0.011	0.254
J2339+0030	-0.132	-0.431	0.129	0.386	0.182	0.603

Table B.4 *cont'd.*

Table B.4 *cont'd.*

Best measurements of line-intensity ratios for NIV]/OIII] and NIV]/CIV along with their corresponding minimum and maximum values.

Name	NIV]/OIII]			NIV]/CIV		
SDSS	Best	min	max	Best	min	max
J0038+1403	-0.312	-0.760	0.040	-1.236	-1.600	-1.010
J0255+0014	0.124	-0.071	0.341	-0.699	-0.870	-0.568
J0745+4157	-0.124	-0.187	0.222	-1.092	-1.130	-0.837
J0753+4030	-0.511	-0.624	-0.213	-1.788	-1.843	-1.500
J0800+4417	-0.090	-0.302	0.181	-1.035	-1.217	-0.681
J0847+3831	0.095	-0.130	0.184	-0.889	-0.944	-0.800
J0852+4734	-0.172	-0.362	0.258	-0.658	-0.783	-0.327
J0855+3754	-0.647	-0.772	-0.353	-1.797	-1.897	-1.565
J0933+0840	-0.686	-0.900	-0.503	-1.599	-1.745	-1.485
J0950+1233	0.301	0.188	0.397	-0.635	-0.679	-0.533
J0953+0037	-0.219	-0.648	0.154	-1.296	-1.639	-1.068
J1042+3811	0.347	0.222	0.387	-0.648	-0.666	-0.591
J1047+0957	-0.282	-0.409	-0.050	-1.469	-1.585	-1.282
J1047+3531	0.162	-0.024	0.370	-0.959	-1.055	-0.865
J1059+6638	0.236	0.040	0.309	-0.808	-0.952	-0.762
J1100+0305	-0.280	-0.391	-0.069	-0.933	-0.977	-0.840
J1121+1238	-0.074	-0.253	0.175	-1.315	-1.407	-1.164
J1156+1337	-0.383	-0.425	-0.361	-1.223	-1.256	-1.210
J1159+3134	-0.387	-0.557	-0.217	-1.387	-1.524	-1.261
J1219+0438	-0.097	-0.319	0.000	-1.496	-1.658	-1.422
J1222+0343	-0.005	-0.233	0.171	-1.086	-1.199	-0.959
J1234+3755	-0.332	-0.438	0.106	-1.099	-1.119	-0.793
J1241+1230	-0.180	-0.363	0.090	-1.015	-1.115	-0.746
J1254+0241	0.158	0.158	0.317	-0.638	-0.675	-0.568
J1304+3404	0.118	0.019	0.293	-0.790	-0.919	-0.632
J1328+5818	-0.470	-0.589	-0.403	-1.409	-1.510	-1.355
J1333+6417	-0.256	-0.457	-0.014	-1.200	-1.330	-1.080

Name	NIV]/OIII]			NIV]/CIV		
SDSS	Best	min	max	Best	min	max
J1339+6328	-0.037	-0.147	0.068	-1.146	-1.214	-1.069
J1356+4710	-0.049	-0.439	0.315	-1.278	-1.506	-1.170
J1404+0728	0.363	0.284	0.485	-0.737	-0.771	-0.624
J1429+3438	-0.328	-0.600	-0.065	-1.518	-1.726	-1.369
J1430+4811	0.060	-0.055	0.176	-0.493	-0.549	-0.430
J1442+1005	-0.241	-0.581	-0.006	-1.307	-1.468	-1.077
J1448+4408	0.343	0.157	0.477	-0.430	-0.577	-0.279
J1456+4339	0.178	-0.063	0.381	-0.982	-1.125	-0.889
J1545+5112	-0.350	-0.518	-0.209	-1.114	-1.296	-0.929
J1550+0236	0.244	0.128	0.377	-0.423	-0.534	-0.220
J1641+2232	0.131	0.118	0.194	-0.459	-0.463	-0.415
J1650+4151	-0.203	-0.519	0.329	-1.248	-1.447	-0.793
J1707+6443	0.060	-0.177	0.236	-1.066	-1.260	-0.981
J1713+3250	-0.086	-0.255	0.051	-1.077	-1.191	-0.987
J2331-0106	-0.234	-0.342	-0.025	-1.297	-1.421	-1.127
J2339+0030	-0.242	-0.466	0.021	-1.286	-1.438	-1.106

Table B.4 *cont'd.*

Table B.4 *cont'd.*

Best measurements of line-intensity ratios for NV/He II and NV/CIV along with their corresponding minimum and maximum values.

Name	NV/He II			NV/CIV		
SDSS	Best	min	max	Best	min	max
J0038+1403	0.896	0.757	1.010	-0.025	-0.118	0.044
J0255+0014	0.489	0.308	0.621	-0.241	-0.397	-0.114
J0745+4157	0.555	0.475	0.641	-0.124	-0.173	-0.066
J0753+4030	0.487	0.330	0.815	-0.623	-0.773	-0.346
J0800+4417	1.019	0.871	1.198	0.114	-0.003	0.361
J0847+3831	0.996	0.902	1.126	0.165	0.088	0.254
J0852+4734	0.698	0.497	0.823	0.180	0.044	0.332
J0855+3754	0.870	0.684	1.064	-0.102	-0.247	0.031
J0933+0840	0.960	0.696	1.118	0.232	0.000	0.344
J0950+1233	0.713	0.657	0.749	0.095	0.039	0.151
J0953+0037	0.449	0.197	0.663	-0.547	-0.719	-0.465
J1042+3811	0.752	0.550	0.881	-0.020	-0.208	0.128
J1047+0957	0.698	0.508	0.972	-0.355	-0.509	-0.232
J1047+3531	1.521	1.429	1.545	0.206	0.078	0.245
J1059+6638	0.592	0.511	0.689	-0.257	-0.335	-0.172
J1100+0305	0.305	0.252	0.522	-0.250	-0.315	-0.060
J1121+1238	0.869	0.625	1.112	-0.266	-0.431	-0.121
J1156+1337	0.621	0.420	0.739	-0.204	-0.400	-0.084
J1159+3134	1.631	1.531	1.719	0.380	0.254	0.498
J1219+0438	1.396	1.131	1.587	0.170	-0.057	0.300
J1222+0343	0.995	0.840	1.203	0.018	-0.044	0.104
J1234+3755	1.106	0.953	1.278	0.022	-0.078	0.113
J1241+1230	1.112	0.957	1.203	0.242	0.176	0.339
J1254+0241	0.814	0.796	0.992	0.176	0.121	0.196
J1304+3404	0.782	0.546	0.980	0.195	-0.073	0.381
J1328+5818	0.670	0.518	0.775	-0.247	-0.382	-0.151
J1333+6417	0.942	0.806	1.134	0.096	-0.040	0.270

Name	NV/He II			NV/CIV		
SDSS	Best	min	max	Best	min	max
J1339+6328	0.671	0.517	0.802	-0.428	-0.546	-0.316
J1356+4710	1.131	0.880	1.302	0.180	-0.050	0.300
J1404+0728	0.996	0.799	1.159	0.225	0.036	0.366
J1429+3438	0.653	0.448	0.989	-0.348	-0.464	-0.053
J1430+4811	0.668	0.512	0.744	0.077	0.046	0.153
J1442+1005	0.976	0.641	1.270	-0.179	-0.397	-0.007
J1448+4408	0.949	0.802	1.196	0.267	0.140	0.487
J1456+4339	0.587	0.507	0.629	-0.329	-0.408	-0.302
J1545+5112	0.786	0.661	0.873	0.064	-0.076	0.196
J1550+0236	0.548	0.320	0.708	-0.142	-0.269	0.022
J1641+2232	0.797	0.713	0.908	0.291	0.212	0.358
J1650+4151	0.734	0.443	0.989	-0.244	-0.457	0.017
J1707+6443	0.907	0.622	1.094	-0.164	-0.331	-0.054
J1713+3250	0.681	0.504	0.819	-0.045	-0.191	0.064
J2331-0106	0.661	0.391	0.991	-0.321	-0.602	0.007
J2339+0030	0.998	0.800	1.154	0.095	-0.016	0.239

Table B.4 *cont'd.*

Table B.4 *cont'd.*

Best measurements of line-intensity ratios for NV/OVI and NV/(CIV+OVI) along with their corresponding minimum and maximum values.

Name	NV/OVI			NV/(CIV+OVI)		
	Best	min	max	Best	min	max
J0038+1403	-	-	-	-	-	-
J0255+0014	-	-	-	-	-	-
J0745+4157	0.060	-0.032	0.165	-0.343	-0.409	-0.267
J0753+4030	-0.018	-0.235	0.289	-0.719	-0.884	-0.437
J0800+4417	-	-	-	-	-	-
J0847+3831	-0.069	-0.173	0.063	-0.268	-0.363	-0.153
J0852+4734	-	-	-	-	-	-
J0855+3754	-	-	-	-	-	-
J0933+0840	-	-	-	-	-	-
J0950+1233	0.124	0.042	0.207	-0.192	-0.260	-0.123
J0953+0037	-	-	-	-	-	-
J1042+3811	-	-	-	-	-	-
J1047+0957	-	-	-	-	-	-
J1047+3531	-	-	-	-	-	-
J1059+6638	0.166	0.083	0.251	-0.396	-0.475	-0.311
J1100+0305	-	-	-	-	-	-
J1121+1238	0.665	0.466	0.842	-0.314	-0.483	-0.166
J1156+1337	0.524	0.315	0.878	-0.278	-0.477	-0.129
J1159+3134	-	-	-	-	-	-
J1219+0438	-	-	-	-	-	-
J1222+0343	-	-	-	-	-	-
J1234+3755	0.320	0.166	0.453	-0.155	-0.274	-0.051
J1241+1230	0.570	0.395	0.690	0.075	-0.029	0.179
J1254+0241	-	-	-	-	-	-
J1304+3404	-	-	-	-	-	-
J1328+5818	0.083	-0.076	0.200	-0.414	-0.557	-0.311

Name	NV/OVI			NV/(CIV+OVI)		
	Best	min	max	Best	min	max
J1333+6417	-	-	-	-	-	-
J1339+6328	-	-	-	-	-	-
J1356+4710	0.732	0.432	0.901	0.073	-0.174	0.203
J1404+0728	0.637	0.431	0.860	0.083	-0.111	0.245
J1429+3438	-	-	-	-	-	-
J1430+4811	-	-	-	-	-	-
J1442+1005	0.134	-0.064	0.313	-0.351	-0.562	-0.177
J1448+4408	0.141	0.009	0.347	-0.102	-0.232	0.110
J1456+4339	0.181	0.101	0.260	-0.446	-0.525	-0.407
J1545+5112	-	-	-	-	-	-
J1550+0236	-	-	-	-	-	-
J1641+2232	-	-	-	-	-	-
J1650+4151	-	-	-	-	-	-
J1707+6443	0.254	0.087	0.395	-0.305	-0.472	-0.186
J1713+3250	0.154	-0.142	0.339	-0.258	-0.468	-0.121
J2331-0106	0.299	0.057	0.612	-0.414	-0.688	-0.089
J2339+0030	0.311	0.132	0.480	-0.111	-0.249	0.042

Table B.4 *cont'd.*

Table B.5

Metallicity Estimates from individual line-intensity ratios. This table lists the Z estimates from NIII]/CIII] and NIII]/OIII] line-intensity ratios, the best estimates along with the corresponding minimum and maximum values.

QSO Name	Metallicity $Log(Z/Z_{sun})$ N III]/C III]			Metallicity $Log(Z/Z_{sun})$ N III]/O III]		
SDSS	Best Estimate	Minimum	Maximum	Best Estimate	Minimum	Maximum
J0038+1403	0.388	0.181	0.584	0.661	0.380	0.952
J0255+0014	0.614	0.469	0.861	0.774	0.662	0.976
J0745+4157	0.641	0.522	1.055	0.682	0.622	0.934
J0753+4030	-0.061	-0.264	0.250	0.119	0.052	0.241
J0800+4417	0.600	0.311	0.762	0.708	0.512	0.841
J0847+3831	0.985	0.680	1.150	1.103	0.811	1.270
J0852+4734	1.187	0.951	1.577	0.909	0.720	1.370
J0855+3754	0.282	0.131	0.595	0.515	0.384	0.733
J0933+0840	0.541	0.301	0.938	0.730	0.526	0.939
J0950+1233	1.072	0.709	1.522	1.014	0.856	1.286
J0953+0037	0.270	0.131	0.497	0.486	0.288	0.762
J1042+3811	1.185	1.053	1.403	1.092	0.916	1.148
J1047+0957	0.100	-0.068	0.256	0.265	0.202	0.366
J1047+3531	1.326	1.144	1.496	1.587	1.254	1.838
J1059+6638	0.376	0.227	0.538	0.530	0.404	0.627
J1100+0305	1.156	0.476	1.492	0.656	0.449	0.889
J1121+1238	0.769	0.566	1.157	1.095	0.931	1.398
J1156+1337	0.916	0.651	1.146	0.732	0.624	0.808
J1159+3134	0.337	0.191	0.517	0.824	0.654	1.008
J1219+0438	-0.166	-0.504	0.162	0.485	0.236	0.744
J1222+0343	0.352	0.221	0.643	0.913	0.717	1.103
J1234+3755	0.376	0.201	0.593	0.701	0.554	0.929
J1241+1230	0.749	0.563	1.145	1.041	0.923	1.338

QSO Name	Metallicity $Log(Z/Z_{sun})$ N III]/C III]			Metallicity $Log(Z/Z_{sun})$ N III]/O III]		
SDSS	Best Estimate	Minimum	Maximum	Best Estimate	Minimum	Maximum
J1254+0241	0.848	0.696	0.893	0.976	0.938	1.140
J1304+3404	1.206	1.022	1.384	1.272	1.028	1.510
J1328+5818	0.099	0.010	0.204	0.229	0.188	0.280
J1333+6417	0.538	0.423	0.678	0.961	0.774	1.292
J1339+6328	0.369	0.152	0.618	0.316	0.248	0.398
J1356+4710	0.309	-0.010	0.581	1.002	0.608	1.617
J1404+0728	0.908	0.680	1.288	1.188	1.069	1.305
J1429+3438	0.163	0.009	0.443	0.445	0.309	0.721
J1430+4811	1.107	0.964	1.407	0.866	0.744	1.073
J1442+1005	0.417	0.165	0.534	0.689	0.324	0.774
J1448+4408	0.796	0.481	1.214	0.848	0.592	1.090
J1456+4339	0.417	0.242	0.636	0.729	0.491	0.924
J1545+5112	0.369	0.152	0.589	0.444	0.331	0.548
J1550+0236	1.096	0.824	1.392	0.824	0.728	0.903
J1641+2232	0.758	0.634	1.114	0.986	0.937	1.284
J1650+4151	0.457	0.308	0.762	1.002	0.688	1.355
J1707+6443	0.355	0.138	0.615	0.449	0.280	0.663
J1713+3250	0.606	0.408	1.060	0.679	0.592	0.740
J2331-0106	0.438	0.349	0.667	0.650	0.547	0.816
J2339+0030	0.659	0.367	1.095	0.962	0.736	1.289

Table B.5 *cont'd.*

Table B.5 *cont'd.*

Metallicity Estimates from individual line-intensity ratios. This table lists the *Z* estimates from NIV]/OIII] and NIV]/CIV line-intensity ratios, the best estimates along with the corresponding minimum and maximum values.

QSO Name	Metallicity Log(Z/Z_{sun}) N IV]/O III]			Metallicity Log(Z/Z_{sun}) N IV]/C IV		
SDSS	Best Estimate	Minimum	Maximum	Best Estimate	Minimum	Maximum
J0038+1403	0.642	-0.397	0.982	0.247	-0.155	0.485
J0255+0014	1.080	0.884	1.351	0.772	0.628	0.866
J0745+4157	0.838	0.782	1.202	0.400	0.361	0.662
J0753+4030	0.259	-0.120	0.759	-0.345	-0.396	-0.052
J0800+4417	0.868	0.660	1.151	0.459	0.269	0.785
J0847+3831	1.044	0.832	1.155	0.609	0.552	0.700
J0852+4734	0.795	0.551	1.247	0.801	0.712	1.057
J0855+3754	-0.183	-0.413	0.567	-0.353	-0.446	-0.119
J0933+0840	-0.289	-0.590	0.289	-0.154	-0.305	-0.036
J0950+1233	1.301	1.160	1.421	0.818	0.786	0.891
J0953+0037	0.754	-0.185	1.117	0.178	-0.196	0.425
J1042+3811	1.359	1.202	1.409	0.809	0.796	0.849
J1047+0957	0.696	0.465	0.903	-0.020	-0.140	0.194
J1047+3531	1.128	0.926	1.388	0.537	0.438	0.633
J1059+6638	1.220	0.982	1.311	0.692	0.544	0.727
J1100+0305	0.700	0.498	0.886	0.564	0.518	0.659
J1121+1238	0.882	0.724	1.144	0.156	0.050	0.327
J1156+1337	0.513	0.436	0.553	0.262	0.224	0.277
J1159+3134	0.506	0.086	0.756	0.073	-0.077	0.218
J1219+0438	0.862	0.629	0.947	-0.048	-0.215	0.032
J1222+0343	0.943	0.742	1.139	0.407	0.290	0.537
J1234+3755	0.605	0.413	1.058	0.393	0.373	0.705
J1241+1230	0.802	0.607	1.146	0.463	0.309	0.704

QSO Name	Metallicity Log(Z/Z_{sun}) N IV]/O III]			Metallicity Log(Z/Z_{sun}) N IV]/C IV		
SDSS	Best Estimate	Minimum	Maximum	Best Estimate	Minimum	Maximum
J1254+0241	1.122	1.122	1.321	0.816	0.789	0.866
J1304+3404	1.072	0.964	1.291	0.707	0.578	0.820
J1328+5818	0.354	-0.024	0.476	0.047	-0.062	0.110
J1333+6417	0.721	0.378	0.935	0.289	0.139	0.413
J1339+6328	0.914	0.817	1.010	0.345	0.272	0.424
J1356+4710	0.904	0.411	1.319	0.199	-0.058	0.320
J1404+0728	1.379	1.280	1.531	0.745	0.721	0.826
J1429+3438	0.613	-0.054	0.890	-0.07	-0.285	0.094
J1430+4811	1.000	0.899	1.145	0.919	0.879	0.964
J1442+1005	0.734	-0.003	0.942	0.165	-0.019	0.416
J1448+4408	1.354	1.121	1.521	0.964	0.859	1.108
J1456+4339	1.148	0.891	1.401	0.513	0.367	0.609
J1545+5112	0.573	0.233	0.763	0.378	0.178	0.568
J1550+0236	1.230	1.085	1.396	0.969	0.890	1.171
J1641+2232	1.211	1.165	1.362	0.944	0.936	0.991
J1650+4151	0.768	0.229	1.336	0.233	0.004	0.705
J1707+6443	1.000	0.791	1.220	0.427	0.219	0.514
J1713+3250	0.871	0.722	0.992	0.416	0.299	0.508
J2331-0106	0.741	0.587	0.925	0.176	0.034	0.365
J2339+0030	0.734	0.362	0.966	0.189	0.014	0.386

Table B.5 *cont'd.*

Table B.5 *cont'd.*

Metallicity Estimates from individual line-intensity ratios. This table lists the *Z* estimates from NV/He II and NV/CIV line-intensity ratios, the best estimates along with the corresponding minimum and maximum values.

QSO Name	Metallicity Log(Z/Z_{sun}) N V/He II			Metallicity Log(Z/Z_{sun}) N V/C IV		
SDSS	Best Estimate	Minimum	Maximum	Best Estimate	Minimum	Maximum
J0038+1403	1.273	1.119	1.400	0.994	0.891	1.096
J0255+0014	0.688	0.498	0.942	0.754	0.570	0.896
J0745+4157	0.810	0.674	0.982	0.884	0.830	0.949
J0753+4030	0.686	0.521	1.183	0.297	0.147	0.632
J0800+4417	1.410	1.246	1.609	1.201	1.026	1.571
J0847+3831	1.384	1.280	1.529	1.278	1.162	1.411
J0852+4734	1.053	0.697	1.192	1.300	1.096	1.528
J0855+3754	1.244	1.038	1.460	0.909	0.748	1.077
J0933+0840	1.344	1.051	1.520	1.378	1.030	1.546
J0950+1233	1.070	1.008	1.110	1.173	1.089	1.257
J0953+0037	0.646	0.381	1.014	0.389	0.201	0.488
J1042+3811	1.113	0.800	1.257	1.000	0.791	1.222
J1047+0957	1.053	0.716	1.358	0.621	0.435	0.764
J1047+3531	1.968	1.866	1.994	1.339	1.147	1.398
J1059+6638	0.884	0.722	1.043	0.737	0.646	0.831
J1100+0305	0.495	0.439	0.744	0.744	0.670	0.956
J1121+1238	1.243	0.950	1.513	0.727	0.529	0.888
J1156+1337	0.942	0.616	1.099	0.796	0.567	0.929
J1159+3134	2.090	1.979	2.188	1.600	1.411	1.777
J1219+0438	1.829	1.534	2.041	1.285	0.959	1.480
J1222+0343	1.383	1.211	1.614	1.057	0.973	1.186
J1234+3755	1.507	1.337	1.698	1.063	0.936	1.199
J1241+1230	1.659	1.472	1.796	1.556	1.454	1.630
J1254+0241	1.182	1.162	1.380	1.294	1.212	1.324

QSO Name	Metallicity $Log(Z/Z_{sun})$ N V/He II			Metallicity $Log(Z/Z_{sun})$ N V/C IV		
SDSS	Best Estimate	Minimum	Maximum	Best Estimate	Minimum	Maximum
J1304+3404	1.147	0.792	1.367	1.322	0.941	1.602
J1328+5818	1.022	0.736	1.139	0.748	0.589	0.854
J1333+6417	1.324	1.173	1.538	1.174	0.978	1.435
J1339+6328	1.023	0.734	1.169	0.533	0.390	0.669
J1356+4710	1.534	1.256	1.724	1.300	0.967	1.480
J1404+0728	1.384	1.166	1.566	1.367	1.084	1.579
J1429+3438	1.003	0.645	1.377	0.630	0.489	0.963
J1430+4811	1.020	0.724	1.104	1.145	1.099	1.260
J1442+1005	1.362	0.982	1.689	0.823	0.570	1.020
J1448+4408	1.332	1.169	1.607	1.431	1.240	1.760
J1456+4339	0.874	0.714	0.958	0.653	0.557	0.686
J1545+5112	1.151	1.012	1.248	1.126	0.938	1.324
J1550+0236	0.796	0.511	1.064	0.864	0.723	1.063
J1641+2232	1.292	1.170	1.450	1.554	1.471	1.666
J1650+4151	1.093	0.640	1.377	0.751	0.498	1.056
J1707+6443	1.286	0.944	1.493	0.840	0.650	0.962
J1713+3250	1.034	0.708	1.188	0.972	0.810	1.126
J2331-0106	1.012	0.585	1.379	0.662	0.322	1.041
J2339+0030	1.387	1.167	1.560	1.173	1.006	1.388

Table B.5 *cont'd.*

Table B.5 *cont'd.*

Metallicity Estimates from individual line-intensity ratios. This table lists the *Z* estimates from NV/OVI and NV/(CIV+OVI) line-intensity ratios, the best estimates along with the corresponding minimum and maximum values.

QSO Name	Metallicity Log(Z/Z_{sun}) N V/O VI			Metallicity Log(Z/Z_{sun}) N V/(C IV+ O VI)		
SDSS	Best Estimate	Minimum	Maximum	Best Estimate	Minimum	Maximum
J0038+1403	-	-	-	-	-	-
J0255+0014	-	-	-	-	-	-
J0745+4157	-	-	-	-	-	-
J0753+4030	0.827	0.524	1.299	0.442	0.249	0.790
J0800+4417	0.859	0.859	0.859	1.395	1.395	1.395
J0847+3831	0.737	0.599	0.970	1.030	0.896	1.187
J0852+4734	-	-	-	-	-	-
J0855+3754	-	-	-	-	-	-
J0933+0840	-	-	-	-	-	-
J0950+1233	1.063	0.933	1.181	1.134	1.041	1.228
J0953+0037	-	-	-	-	-	-
J1042+3811	-	-	-	-	-	-
J1047+0957	-	-	-	-	-	-
J1047+3531	-	-	-	-	-	-
J1059+6638	1.123	1.004	1.244	0.849	0.736	0.970
J1100+0305	-	-	-	-	-	-
J1121+1238	1.836	1.551	2.089	0.966	0.724	1.169
J1156+1337	1.634	1.336	2.140	1.016	0.733	1.219
J1159+3134	-	-	-	-	-	-
J1219+0438	-	-	-	-	-	-
J1222+0343	-	-	-	-	-	-
J1234+3755	1.343	1.123	1.533	1.184	1.022	1.326
J1241+1230	1.851	1.617	1.994	1.645	1.506	1.734

QSO Name	Metallicity $Log(Z/Z_{sun})$ N V/O VI			Metallicity $Log(Z/Z_{sun})$ N V/(C IV+ O VI)		
SDSS	Best Estimate	Minimum	Maximum	Best Estimate	Minimum	Maximum
J1254+0241	-	-	-	-	-	-
J1304+3404	-	-	-	-	-	-
J1328+5818	1.004	0.725	1.171	0.823	0.633	0.970
J1333+6417	-	-	-	-	-	-
J1339+6328	-	-	-	-	-	-
J1356+4710	1.931	1.503	2.173	1.495	1.158	1.672
J1404+0728	1.796	1.501	2.114	1.509	1.244	1.730
J1429+3438	-	-	-	-	-	-
J1430+4811	-	-	-	-	-	-
J1442+1005	1.077	0.746	1.333	0.913	0.627	1.154
J1448+4408	1.087	0.875	1.381	1.256	1.079	1.546
J1456+4339	1.144	1.030	1.257	0.777	0.671	0.833
J1545+5112	-	-	-	-	-	-
J1550+0236	-	-	-	-	-	-
J1641+2232	-	-	-	-	-	-
J1650+4151	-	-	-	-	-	-
J1707+6443	1.249	1.010	1.450	0.979	0.740	1.142
J1713+3250	1.106	0.637	1.370	1.044	0.746	1.230
J2331-0106	1.313	0.959	1.760	0.823	0.479	1.274
J2339+0030	1.330	1.074	1.571	1.244	1.056	1.453

Table B.5 *cont'd.*

Table B.6

Best Metallicity Estimates (Log Z_{best}/Z_{sun}) for the N-Loud Quasar Sample and their corresponding error estimates.

QSO Name	Z_{best}	$\pm\Delta Z_{best}$
SDSS J0038+1403	0.671	0.108
SDSS J0255+0014	0.805	0.085
SDSS J0745+4157	0.761	0.051
SDSS J0753+4030	0.154	0.07
SDSS J0800+4417	0.844	0.113
SDSS J0847+3831	1.102	0.055
SDSS J0852+4734	1.048	0.102
SDSS J0855+3754	0.381	0.198
SDSS J0933+0840	0.59	0.297
SDSS J0950+1233	1.14	0.054
SDSS J0953+0037	0.475	0.089
SDSS J1042+3811	1.159	0.066
SDSS J1047+0957	0.421	0.123
SDSS J1047+3531	1.345	0.081
SDSS J1059+6638	0.716	0.159
SDSS J1100+0305	0.814	0.1
SDSS J1121+1238	0.868	0.071
SDSS J1156+1337	0.739	0.073
SDSS J1159+3134	0.817	0.242
SDSS J1219+0438	0.617	0.266
SDSS J1222+0343	0.816	0.137

QSO Name	Z_{best}	$\pm\Delta Z_{best}$
SDSS J1234+3755	0.686	0.124
SDSS J1241+1230	1.037	0.16
SDSS J1254+0241	1.06	0.083
SDSS J1304+3404	1.218	0.047
SDSS J1328+5818	0.357	0.121
SDSS J1333+6417	0.849	0.12
SDSS J1339+6328	0.533	0.117
SDSS J1356+4710	0.879	0.18
SDSS J1404+0728	1.211	0.095
SDSS J1429+3438	0.463	0.094
SDSS J1430+4811	1.03	0.054
SDSS J1442+1005	0.666	0.076
SDSS J1448+4408	1.107	0.144
SDSS J1456+4339	0.737	0.132
SDSS J1545+5112	0.628	0.148
SDSS J1550+0236	1.003	0.083
SDSS J1641+2232	1.127	0.147
SDSS J1650+4151	0.744	0.097
SDSS J1707+6443	0.661	0.134
SDSS J1713+3250	0.782	0.073
SDSS J2331-0106	0.623	0.056
SDSS J2339+0030	0.882	0.101

Table B.6 *cont'd.*

Table B.7

Quantitative comparison of how well the metallicity from different line-intensity ratios relates to mean metallicity Z_{mean}. The values in brackets are the corresponding error estimates.

Z(line-intensity ratio) (= m * Z_{mean} + c)	Slope (m)	Intercept (c)
Z (N III]/C III])	1.179 (0.149)	-0.341 (0.124)
Z (N III/OIII])	1.073 (0.092)	-0.087 (0.077)
Z (N IV]/OIII])	1.030 (0.164)	0.008 (0.137)
Z (N IV]/C IV)	1.127 (0.137)	-0.504 (0.114)
Z (N V/He II)	0.590 (0.193)	0.715 (0.161)
Z (N V/CIV)	1.000 (0.136)	0.211 (0.114)
Z (N V/OVI)	0.805 (0.324)	0.559 (0.299)
Z (N V/(C IV+O VI))	1.117 (0.144)	0.081 (0.133)

Table B.8

Statistics and Student 't' test results for M_{SMBH} for the two Quasar sample sets.

Mass ~ $Log(M_{SMBH}/M_{SUN})$	All QSOs	N-loud QSOs
Mean Mass	8.32	7.47
Standard deviation	1.05	1.03
Standard error	0.012	0.16
Mass Range (High – Low)	5.10 – 9.66	5.48 – 13.34
Median Mass	8.43	7.51
$(\Delta M_{SMBH})_{mean}$	0.8500	
Standard error of difference	0.161	
P value	< 0.0001	
t value	5.2943	

The P value for this test is, P value < 0.0001. This indicates that this difference between the two data sets is extremely statistically significant.

BIBLIOGRAPHY

REFERENCES

Allende Prieto, C., Lambert, D. L., Asplund, M. 2001, ApJ, 556, L63

Allende Prieto, C., Lambert, D. L., Asplund, M. 2002, ApJ, 573, L137

Baldwin, Jack, Ferland, G. J., Korista, K. T., Verner, D. A. 1995, ApJL, 455, 119

Baldwin, J. A., et. al., 1996, ApJ, 461, 664

Baldwin, J. A., Ferland, G. J., Korista, K. T., Hamann, F., Dietrich, M. 2003a, ApJ, 582, 590

Baldwin, J. A., Hamann, F., Korista, K. T., Ferland, G. J., Dietrich, M., Warner, C. 2003b, ApJ, 583, 649

Bardeen, J. M., J. R. Bond, N. Kaiser, and A. S. Szalay 1986, ApJ, 304, 15

Bentz, M. C., Hall, P. B., Osmer, P. S. 2004, AJ, 128, 561

Brandenberger, R. H. 2002, arXiv:hep-th/0210165

Caldwell, R. R., Linder, E. V. Phys. Rev. Letts., 2005, 95, 141301

Cooper, M.C. et. al., 2007 MNRAS, 376, 1445

Collin S, Zahn, J-P. 1999 ApSS, 265, 501

Dhanda, N., Baldwin, J. A., Osmer P. S., Bentz, M. C., 2007, ApJ, 658, 804

Dietrich, M., Appenzeller, I., Hamann, F., Heidt, J., Jager, K., Vestergaard, M., Wagner, S. J. 2003, AA, 398, 891

Dvali, G., Gabadadze, G., Porrati, M. 2000, Physics Letters, 485, 208

Eisenstein, D. J., Hu, W. 1999, ApJ, 511, 5

eROSITA Mission Document, 2005: www.mpe.mpg.de/erosita/MDD-6.pdf

Evrard, A. E. 2004, Clusters of Galaxies: Probes of Cosmological Structure and Galaxy Evolution, Carnegie Astrophysics Series No. 3 (Cambridge University, Cambridge)

Feldman, H. A., Kaiser, N., Peacock, J. A. 1994, ApJ, 426, 23

Ferrarese, L., Merritt, D. 2000, ApJ, 539, L9

Friaca, A. C. S., Terlevich, R. J. 1998, MNRAS, 298, 399

Futamase, T. 1996, Phys. Rev. D 53, 681

Gladders, M. D. 2009, ApJ, 655, 128

Hamann, F., Ferland, G. J. 1993, ApJ, 418, 11

Hamann, F., Ferland, G. J. 1999, ARAA, 37, 487

Hamann, F., Korista, K. T., Ferland, G. J., Warner, C., Baldwin, J. A. 2002, ApJ, 564, 592

Holweger H. 2001, AIPC, 598, 23

Hopkins, Philip F.; Bundy, Kevin; Hernquist, Lars; Ellis, Richard S. 2007 ApJ, 659, 976

Hu, W., Kravtsov, A. V. 2003, ApJ, 584, 702

Hubble, Edwin P. 1929, Proceedings of the National Academy of Sciences of the United States of America, 15, 168

Holder, G. P., Mohr, J. J., Carlstrom, J. E., Evrard, A. E., Leitch, E. M. 2000, ApJ, 544, 629

Hulse, R. A., Taylor, J. H. 1975, ApJ, 195, 51

Jiang, L., et. al., 2009, AJ, 138, 305

Kaspi, S., Smith, P. S., Netzer, H., Maoz, D., Jannuzi, B. T., Giveon U. 2000 ApJ, 533, 631

Larson, D; et al. 2010, arXiv:astro-ph1001.4635

Levine, E. S., Schulz, A. E., White, M. 2002, ApJ, 577, 569

Linder, E. V. 2005, Phys. Rev. D, D72, 043529

Linder E. V., Cahn R. N. 2007, Astropart. Phys., 28, 481

Majumdar, S., Mohr, J. J. 2004, ApJ, 613, 41

Mantz, A., Allen, S. W., Ebeling, H., Rapetti, D. (2008), MNRAS, 387, 1179

Mo, H. J., White, S. D. M. 1996, MNRAS, 282, 347

Murray, S. S., WFXT team, 2010, 42, 520, Bulletin of the American Astronomical Society

Nagao, T., Marconi, A., Maiolino, R. 2006, AA, 447, 157

Osmer, P. S. 1980, ApJ, 237, 666

Ostriker, J. P.; Steinhardt, P. 2003, Science, 300, 1909

Peacock J. A., Cosmological Physics, 1999 (Cambridge University Press)

Peacock, J. A., and S. J. Dodds 1994, MNRAS, 267, 1020

Peebles, P. J. E. 1980, The Large Scale Structure of the Universe 1980 (Princeton University Press)

Peterson, 1988 PASP, 100, 18

Perlmutter, S, et al. 1999, ApJ, 517, 565

Pettini, M., Ellison, S. L., Bergeron, J., Petitjean, P. 2002, AA, 391, 21

Reiss A. G., et al. 1998, ApJ, 116, 1009

Reiprich, T. H., Bhringer, H. 2002, ApJ, 567, 716

Richards G T et. al., 2002AJ, 123, 2945

Romano, D., Silva, L., Matteucci, F., Danese, L. 2002, MNRAS, 334, 444

Rozo, E. 2009, ApJ, 699, 768

Schimdt, M. 1963, Nature, 197, 1040

Schlegel, D. J., Finkbeiner, D. P., Davis, M. 1998, ApJ, 500, 525

Schneider et al., 2007, AJ, 134, 102S

Shapiro, I. I., 1964, Phys. Rev. Letts., 13, 789

Shemmer, O., Netzer, H. 2002, ApJ, 567, L19

Sheth, R. K., Tormen, G. 1999, MNRAS, 308, 119

Silk, J., Rees, M. J. 1998, AA, 331,1

Soltan, A. 1982, MNRAS, 200, 115

Staniszewski, Z., et. al. 2009, ApJ, 701, 32

Sunyaev, R. A., and Y. B. Zeldovich 1970, Astrophys. Space Sci. 7, 3

Tauber, J. A. 2004, AdSpR, 34, 491

Tegmark, M. 1997, Phys. Rev. Lett., 79, 3806

Toomre, A. 1977, in Proceedings of a Conference at Yale University, May 19-21, 1977

Tremaine, S., et. al., 2002 ApJ, 574, 740

Vanden Berk, D. E., et. al., 2001, AJ, 122, 549

Vestergaard, M., Wilkes, B. J. 2001, ApJS, 134, 1

Voit, G. M. 2005, Rev. Mod. Phys. 77, 207

Wang, L. M., Steinhardt, P. J. 1998, ApJ, 508, 483

Warner, C., Hamann, F., Dietrich, M. 2003, ApJ, 596, 72

Warner, C., Hamann, F., Dietrich, M. 2004, ApJ, 608, 136

Warner, C., Hamann, F., Dietrich, M. 2007, ASPC, 373, 653H

Will, C. M. 2001, Living Rev. Rel. 4, 4